



HAL
open science

Statistical analysis of the coupling effects between tags in the RFID links

Aiman Mughal

► **To cite this version:**

Aiman Mughal. Statistical analysis of the coupling effects between tags in the RFID links. Electronics. Université Gustave Eiffel, 2024. English. NNT : 2024UEFL2002 . tel-04550099

HAL Id: tel-04550099

<https://theses.hal.science/tel-04550099>

Submitted on 17 Apr 2024

HAL is a multi-disciplinary open access archive for the deposit and dissemination of scientific research documents, whether they are published or not. The documents may come from teaching and research institutions in France or abroad, or from public or private research centers.

L'archive ouverte pluridisciplinaire **HAL**, est destinée au dépôt et à la diffusion de documents scientifiques de niveau recherche, publiés ou non, émanant des établissements d'enseignement et de recherche français ou étrangers, des laboratoires publics ou privés.



UNIVERSITÉ GUSTAVE EIFFEL

Ecole Doctorale Mathématiques, Sciences et Technologies de
l'Information et de la Communication

Thesis Report

to obtain the rank of

DOCTOR of Université Gustave Eiffel

Specializations: Electronics, Optronics and Systems (CNU 63)

presented by

Aiman MUGHAL

Statistical analysis of the coupling effects between tags in the RFID links

Directed by

Mr. Jean-Marc LAHEURTE

Supervised by

Mrs. Shermila MOSTARSHEDI and Mr. Benoit POUSSOT

For a thesis defence on Jan 15, 2024, in front of the jury composed of :

Mr. Nicolas BARBOT	Université Grenoble Alpes	Rapporteur
Mr. Bernard UGUEN	Université de Rennes 1	Rapporteur
Mrs. Alessandra COSTANZO	Université de Bologne	Examiner
Mrs. Shermila MOSTARSHEDI	Université Gustave Eiffel	Thesis co-supervisor
Mr. Benoit POUSSOT	Université Gustave Eiffel	Thesis co-supervisor
Mr. Jean-Marc LAHEURTE	Université Gustave Eiffel	Thesis Director

Acknowledgement

I want to take a moment to express my sincere appreciation to the esteemed jury members, Nicolas BARBOT, Bernard UGUEN and Alessandra COSTANZO who bestowed upon me the honour of evaluating my work. Your thoughtful comments and constructive feedback have offered me a valuable and unique perspective on the project I have diligently undertaken.

I extend my heartfelt gratitude to my Thesis Director, Professor Jean-Marc LAHEURTE, former Director of ESYCOM, University Gustave Eiffel. From my early days as a student, through my master's internship, and to the culmination of this thesis, you have been an unwavering source of support, trust, and invaluable guidance. Your genuine humanity and your remarkable ability to provide perspective in the realm of academia, where your reputation is truly exceptional, have left an indelible mark on me. Thank you again, Professor LAHEURTE, for being an outstanding mentor and a true inspiration throughout this academic journey.

I am equally indebted to my thesis supervisors, Shermila MOSTARSHEDI and Benoit POUSSOT, Associate Professor at University Gustave Eiffel. I cannot adequately convey my appreciation for your invaluable guidance and unwavering support, without which the completion of this thesis would not have been possible. Throughout this journey, I have not only gained immense knowledge and wisdom from a professional perspective but also profound life lessons from both of you. Your consistent presence and unwavering support from the very beginning to the end of this journey have been a tremendous blessing, and I consider myself exceptionally fortunate to have had both of you as my mentors. Additionally, I would like to express my gratitude to Stéphane PROTAT and Jimmy LESZCZYŃSKI, who have consistently been a reliable source of assistance.

I am overwhelmed with profound gratitude for the invaluable friendships that have flourished throughout my doctoral journey. Among these cherished companions, I wish to express my deepest appreciation to Mahdi, Said, Jithin, Meriem, Hocine, Moen, Nikky, Josephine, Nadeen, and Moussa. Each of them has been an integral part of this transformative experience, and I am sincerely thankful for their presence and support.

Saving the best for last, I am also eternally grateful to my parents to whom I wholeheartedly dedicate this thesis. They have bestowed upon me everything in this life, and I owe them an immeasurable debt of gratitude. I know I can never fully repay them for all they've done, but I will tirelessly endeavor to do so. Without their unwavering support and love, my name would never grace the pages of this manuscript. I pray that the Lord continues to bless me with their presence for many more years to come.

Reserving the finest acknowledgment for the conclusion, I would like to thank my

beloved husband Sohaib, whose presence in my life has truly been a divine blessing. Your dedication to alleviating my stress amid your hectic schedule deserves nothing but admiration. You have been my oasis, enveloping me in serenity at the close of each demanding day. You are my anchor, my confidant, and my unwavering source of support.

Abstract

Different empirical studies show that the effect of mutual coupling and the random position and orientation of tag antennas in a reduced volume result in a degradation of key performance indicators of an RFID system such as the read-range and the read-rate. This thesis takes part in the performance analysis of such an RFID system by exploring the physical phenomena behind the degradation and by introducing statistical techniques into investigations. Prior to the group behaviour investigations, the sensitivity and the impedance of two RFID chips (Higgs-3 and Higgs-9) have been measured. Two RFID tags have been used, a commercial one (ALN-9662) associated with the Higgs-3 chip and a home-made tag, which has been fabricated in laboratory to match the Higgs-9 chip. The read range of both tags have measured along with their antenna impedances. The measurement results have been confronted to electromagnetic simulations. In order to study various cases involving randomly positioned tags, an electromagnetic model and simulation tools (HFSS and NEC) have been used and the conclusions are based on their results while cross-validated in a few cases by measurements. To simplify any further, the RFID tags are modelled by a set of half-wave dipoles, with and without T-match, and the reader is replaced by a plane wave. The objective is to confront the behaviour of a single isolated tag to that of the same tag while surrounded by other tags and to conclude on the impact of the antenna type, the density of tags, the terminating load and the wave polarisation on the output under observation. The RFID link is studied through its forward and reverse links and by using a conventional grid model for tags including coupling. A thorough power budget analysis is conducted and the absorbed power at the level of the loads (chips) and the reradiated power at the level of the antennas are assessed. Regarding the forward link, the ratio of the absorbed power by the chip of a surrounded tag to that of an isolated tag is called normalised absorbed power and constitutes a useful tool to estimate the percentage of inactivated tags in the set. Regarding the reverse link, the Radar Cross Section (RCS) of loaded antennas with short-circuit and matched loads have been studied. The differential RCS of the isolated tag and that of the surrounded one has also been evaluated and the impact of coupling on the backscattered power have been studied. As in a high-density random context, predicting the system performances in a realistic way with a deterministic approach is impossible, several configurations of randomly positioned and oriented tags and dipoles have been simulated and the conclusions are drawn using statistical analysis. In other words, at the end of this study, the performance degradation of a particular tag in a given configuration of surrounding tags needs to be evaluated individually but the statistical moments as well as cumulative distribution functions allow to predict the behaviour of the population tags under given conditions. This thesis helps the RFID designer to assess the performance of an RFID scenario and eventually adjust some input parameters such as the density of

tags in order to attain the desired objectives.

Resumé

Différentes études empiriques montrent que l'effet du couplage mutuel et la position et l'orientation aléatoires des antennes tags dans un volume réduit entraînent une dégradation des indicateurs de performance d'un système RFID, tels que la distance et le taux de lecture. Cette thèse participe à l'analyse des performances d'un tel système RFID en explorant les phénomènes physiques à l'origine de la dégradation et en introduisant des techniques statistiques dans les investigations. Avant de procéder à l'étude du comportement de groupe, la sensibilité et l'impédance de deux puces RFID (Higgs-3 et Higgs-9) ont été mesurées. Deux tag RFID ont été utilisées, un tag commercial (ALN-9662) associé à la puce Higgs-3 et tag fabriqué au laboratoire pour s'adapter à la puce Higgs-9. La distance de lecture des deux tags a été mesurée ainsi que l'impédance de leur antenne. Les résultats des mesures ont été confrontés à des simulations électromagnétiques. Afin d'étudier différents cas de figure faisant intervenir des tags positionnés de manière aléatoire, un modèle électromagnétique et des outils de simulation (HFSS et NEC) ont été utilisés. Les résultats ont été validés expérimentalement pour quelques configurations. Pour simplifier davantage, les tags RFID sont modélisés par un ensemble de dipôles demi-onde, avec et sans le circuit d'adaptation sous forme de T-match, et le lecteur est remplacé par une onde plane. L'objectif est de confronter le comportement d'un tag isolé à celui du même tag entouré par d'autres tags et de conclure sur l'impact du type d'antenne, de la densité des tags, de l'impédance de charge et de la polarisation de l'onde sur l'observable de sortie. La liaison RFID est étudiée à travers son lien forward et reverse, en utilisant un modèle multiport conventionnel pour les tags intégrant le couplage. Une analyse approfondie du bilan de puissance est effectuée et la puissance absorbée au niveau des charges (puces) et la puissance re-rayonnée au niveau des antennes sont évaluées. En ce qui concerne la liaison forward, le rapport entre la puissance absorbée par la puce d'un tag environné et celle d'un tag isolé est appelé puissance absorbée normalisée et constitue un outil utile pour estimer le pourcentage de tags inactifs dans un ensemble de tags. En ce qui concerne la liaison reverse, la surface équivalente radar (SER) des antennes chargées par une charge adaptée et par un court-circuit a été étudiée. La SER différentielle du tag isolé et celle du tag environné ont également été évaluées et l'impact du couplage sur la puissance re-rayonnée a été étudié. Étant donné que dans un contexte aléatoire à haute densité, il est impossible de prédire les performances du système de manière réaliste avec une approche purement déterministe, plusieurs configurations de tags et de dipôles positionnés et orientés de manière aléatoire ont été simulées et les conclusions sont tirées à l'aide d'une analyse statistique. En d'autres termes, si la

dégradation des performances d'un tag particulier dans une configuration donnée de tags environnants est évaluée individuellement, les moments statistiques ainsi que les fonctions de répartition permettent de prédire le comportement d'une population de tags sous certaines conditions. Cette thèse aide le concepteur RFID à évaluer la performance d'un scénario RFID et éventuellement à ajuster certains paramètres d'entrée tels que la densité des tags afin d'atteindre les objectifs visés.

Contents

1	Introduction	1
1.1	RFID: from the context to the problem statement	1
1.2	State of art	5
1.3	Objectives of the thesis	10
1.4	Organisation of the Manuscript	11
2	Characterisation of an RFID tag and its simplified model	13
2.1	Tools and techniques used in the study	14
2.1.1	Measurement bench to characterise the UHF RFID chips	15
2.1.2	Measurement bench to characterise the UHF RFID tag antennas without chip	17
2.1.3	Measurement bench to characterise UHF RFID tag antenna and chip together	18
2.1.4	Simulation tools	18
2.2	Characterisation of the RFID tags and the chip	19
2.2.1	Real commercial UHF RFID tag	19
2.2.2	Characterisation of the RFID tag	20
2.3	Dipole-based RFID system	30
2.3.1	Half-wave dipole, with and without T-match network	32
2.3.2	Impedance of a tag compared with dipole, with and without T- match	33
2.4	Conclusion	34
3	RFID grid modelling: A comprehensive study	36
3.1	Network representation of an RFID grid	36
3.2	Power Budget analysis	42
3.2.1	Isolated case	42
3.2.2	A set of two parallel antennas	45
3.2.3	Array of ten randomly distributed antennas	48
3.3	RFID forward link	50
3.4	RFID reverse link and differential RCS	54

CONTENTS

3.4.1	RCS definition	55
3.4.2	RCS of a loaded antenna	56
3.4.3	Estimation of differential RCS	58
3.4.4	Simulation results of RCS and differential RCS	59
3.5	Conclusion	68
4	Statistical evaluation of RFID links in a high-density context	70
4.1	Methodology	70
4.2	Statistical analysis in the forward link	72
4.3	Statistical analysis in the reverse link	80
4.4	Conclusion	84
5	Conclusion and Perspectives	86
A	Derivation of absorbed and re-radiated powers	92
A - 1	Absorbed power in terms of reflection coefficient	92
A - 2	Re-radiated power in terms of reflection coefficient	93
B	Automation of simulation with NEC using MATLAB	94
B - 1	Presentation of 4NEC2 graphic interface	94
B - 1.1	Geometry Editor (Ctrl+F3)	97
B - 1.2	NEC Editor (New Version) (Ctrl+F4)	98
C	Automation of simulation with HFSS using MATLAB:	102
D	Near-field of dipole using NEC	104
	Résumé	112

List of Figures

1.1	Schematic diagram of RFID system	3
1.2	Principle of backscattering	3
1.3	Practical examples of UHF RFID technology in a high-density context	5
1.4	Communication between a reader and a set of multiple RFID tags terminated with their chip impedances	6
1.5	Thevenin network model for an RFID grid	7
1.6	Effects of mutual coupling on the forward and reverse links of an RFID system	7
2.1	Measurement bench to measure the complex impedance of the UHF RFID chip.	15
2.2	Experimental setup to measure the threshold of the chip, connected with SMA.	16
2.3	Experimental setup to measure the complex impedance of UHF RFID tag without a chip.	17
2.4	Experimental setup to measure the read range of UHF RFID tag.	18
2.5	Schematic of real commercial UHF RFID tag (ALN-9662).	20
2.6	Measured impedance of the UHF RFID Higgs-3 chip over a range of input powers in the impedance analyser.	21
2.7	Measured real and imaginary parts of the impedance of three samples of Higgs-3 chip using the impedance analyser.	22
2.8	Higgs-9 chip connected with SMA and experimental setup to measured P_{\min}	23
2.9	Measured real and imaginary parts of the impedance of two samples of Higgs-9 chips using the impedance analyser.	24
2.10	Power absorbed, P_{th} by the chip in dBm (a) and Γ_{50} of the Higgs-9 chip (b).	24
2.11	Schematic of the home-made RFID tag with its dimensions (top view in (a) and side view in (b)).	25
2.12	Measured (dotted line) and simulated (solid line) impedance of ALN-9662 tag (a) and home-made tag (b) over the frequency band.	26

LIST OF FIGURES

2.13	Real and imaginary parts of the commercial ALN-9662 tag (measured: solid line) and chip (simulated: dotted line).	26
2.14	Measured real and imaginary parts of the impedance of the home-made tag (solid line) and the Higgs-9 chip (dotted line).	27
2.15	Measured and simulated reflection coefficient in dB of ALN-9662 tag (a) and home-made tag (b).	29
2.16	Measured and simulated read range (m) of three samples of ALN-9662 (a) and home-made tag (b).	29
2.17	(a) RFID tags and reader modeled by (b) loaded dipoles illuminated by a linearly or circularly polarised plane wave.	31
2.18	Schematic of dipole, with (a) and without Tmatch (b) network indicating its respective dimensions.	32
2.19	Real and imaginary parts of the impedance of the tag and the dipole with and without T-match using HFSS (solid line) and NEC (dashed line).	33
3.1	Equivalent circuit model of (a) N loaded tag antennas exposed to an incident electromagnetic wave (b) the circuit as seen by the n^{th} tag antenna.	37
3.2	Isolated (a) dipole, (b) T-matched dipole and (c) tag, illuminated by a plane wave in normal incidence.	43
3.3	Power levels of the isolated antennas employing the linearly polarised plane wave in (a) and circularly polarised plane wave in (b) under three numerical techniques: i. direct plane wave excitation in NEC, ii. open circuit voltage V^{OC} from NEC, iii. direct plane wave in HFSS. $P_{V^{\text{OC}}}$: Induced power on the antenna, $P_{V_{\text{in}}^{\text{OC}}}$: Induced power by other antennas, P_{in} : Re-radiated power by the antenna, P_{L} : Absorbed power by the load.	44
3.4	A set of two parallel dipoles (a), T-matched dipoles (b), and tags (c), placed at a distance d from each other and illuminated by a plane wave in a normal incidence.	46
3.5	Power levels of two parallel dipoles, T-matched dipoles and tags, spaced at a distance of (a) 0.1λ , (b) 0.2λ and (c) 0.3λ . $P_{V^{\text{OC}}}$: Induced power on the antenna, $P_{V_{\text{in}}^{\text{OC}}}$: Induced power by other antennas, P_{in} : Re-radiated power by the antenna, P_{L} : Absorbed power by the load.	47
3.6	Ten loaded half-wave dipoles randomly distributed over a surface of dimensions $1\lambda \times 1\lambda$	48

3.7	Power budget for a grid of 10 randomly distributed matched dipoles using linear (LP) and circular (CP) polarisation, with (w/) and without (w/o) mutual coupling at a polarisation angle of $\phi = 0^\circ$. P_{Voc} : Induced power on the antenna, $P_{V_{in}^{oc}}$: Induced power by other antennas, P_{in} : Re-radiated power by the antenna, P_L : Absorbed power by the load.	49
3.8	Absorbed powers (P_L) of (a) dipoles and (b) T-matched dipoles obtained by NEC and HFSS and (c) compared to those of the tags, in the random configuration shown in Figure 3.6.	51
3.9	Normalized absorbed powers (P_{Lnorm}) of (a) dipoles and (b) T-matched dipoles obtained by NEC and HFSS and (c) compared to those of the tags, in the random configuration shown in Fig. 3.6 with respect to their isolated P_L	52
3.10	Data exchange between an RFID reader and a tag	54
3.11	Equivalent circuit of an RFID tag	56
3.12	Isolated dipole and an arbitrary observation point P , illuminated by a linearly polarised plane wave.	59
3.13	Mono-static RCS(σ) in dBm ² of an isolated case terminated with matched load for three planes, (a) $\phi = 0^\circ$, (b) $\phi = 90^\circ$ and (c) $\theta = 90^\circ$ for a linear polarised plane wave.	60
3.14	Mono-static RCS(σ) in dBm ² of an isolated case terminated with short circuited load for three planes, (a) $\phi = 0^\circ$, (b) $\phi = 90^\circ$ and (c) $\theta = 90^\circ$ for a linear polarised plane wave.	61
3.15	RCS(σ) in dBm ² of two parallel antennas (c.f Fig. 3.4) terminated with matched load for three planes, (a) $\phi = 0^\circ$, (b) $\phi = 90^\circ$ and (c) $\theta = 90^\circ$ for a linear polarised plane wave using NEC (black solid line) and HFSS (grey solid line).	63
3.16	Mono-static RCS(σ) in dBm ² of ten randomly distributed antennas (c.f Fig. 3.6) terminated with matched load for three planes, (a) $\phi = 0^\circ$, (b) $\phi = 90^\circ$ and (c) $\theta = 90^\circ$ for a linear polarised plane wave using NEC (black solid line) and HFSS (grey solid line).	65
3.17	Δ RCS of a set of ten randomly distributed antennas over a surface of dimensions $1\lambda \times 1\lambda$	67
4.1	Automation steps of simulating files from NEC.	71
4.2	CDF plots for the normalised absorbed power (P_{Lnorm}) in dB of 2000 configurations of 10 randomly distributed matched dipoles without T-match (black line) in (a) and with T-match (blue line) in (b), illuminated by a linearly and circularly polarised wave over four distribution surface areas and compared with the matched tags (red thick line) for one distribution surface of $1\lambda \times 1\lambda$ in (c) with linear polarisation.	75

LIST OF FIGURES

4.3	CDF plot for the normalised absorbed power in 2000 configurations of 10 randomly distributed matched dipoles and T-matched dipoles illuminated by a circularly polarised wave over $3\lambda \times 3\lambda$ (solid line) and $4\lambda \times 4\lambda$ (dotted line) surface area.	76
4.4	CDF plots for the normalised absorbed power ($P_{L_{\text{norm}}}$) in dB of 2000 configurations of 10 randomly distributed matched dipoles without T-match (solid line) and with T-match (dotted line), illuminated by a linearly and circularly polarised wave over two distribution surface areas of $2\lambda \times 2\lambda$ in (a) and $4\lambda \times 4\lambda$ in (b).	78
4.5	CDF plot for the normalised absorbed power in 2000 configurations of 10 randomly distributed matched tags illuminated by a linearly polarised wave over $1\lambda \times 1\lambda$ area.	79
4.6	CDF plots for the differential RCS (ΔRCS) in dBm^2 of 2000 configurations of 10 randomly distributed dipoles without T-match (solid line) and with T-match (dotted line) over two distribution surface areas of $1\lambda \times 1\lambda$ (black line) and $2\lambda \times 2\lambda$ (grey line).	82
4.7	CDF plot for the ΔRCS in dBm^2 of samples (dipoles and T-matched dipoles) illuminated by a linearly polarised wave and having normalised absorbed power higher than 0 dB over a distribution of $1\lambda \times 1\lambda$ and $2\lambda \times 1\lambda$ area.	83
B.1	Graphical interface of the 4NEC2 electromagnetic simulator	94
B.2	Notepad editor of 4NEC2	95
B.3	Specifications of a plane wave	97
B.4	Old version of 4NEC2 editor	98
B.5	Geometry editor of 4NEC2	98
B.6	Geometry editor of 4NEC2	99
B.7	Geometry editor of 4NEC2	99
B.8	Geometry editor of 4NEC2	100
B.9	Geometry editor of 4NEC2	101
B.10	Geometry editor of 4NEC2	101
C.1	Declaration of packages and creation of HFSS projects from the script	102
C.2	Declaration of local variables on the HFSS script	103
C.3	Creation of boundary box	103
C.4	Specifications used to assign RLC port and plane wave excitation	104
C.5	Simulation parameters	104
C.6	Launching the HFSS simulation and exporting the results from the script	104
D.1	Cartesian and spherical coordinates at point P	105
D.2	Input parameters for radiated near electric field using NEC	105

I	Bilan de puissance de dix dipôles demi-onde chargés répartis aléatoirement sur une surface de dimensions $1\lambda \times 1\lambda$	115
II	Graphique CDF pour le Δ SER en dBm ² d'échantillons (dipôles et dipôles adaptés en T) éclairés par une onde polarisée linéairement et ayant une puissance absorbée normalisée supérieure à 0 dB sur une distribution de $1\lambda \times 1\lambda$ et $2\lambda \times 1\lambda$	118

List of Tables

2.1	Input impedance of the isolated dipole with and without T-match network and real tag at 928 MHz.	34
3.1	Δ RCS in dBm ² of the isolated dipole with and without T-match and real tag, illuminated by a linearly polarised plane wave at a normal incidence.	66
3.2	Δ RCS in dBm ² of two parallel dipoles, T-matched dipoles and tags in the direction of normal incidence, placed at a distance of 0.1λ , 0.2λ and 0.3λ	67
4.1	Key parameters of statistical studies for forward link	72
4.2	Statistical moments of the absorbed power	73
4.3	Isolated power for Linear Polarisation (LP)	74
4.4	Isolated power for Circular Polarisation (CP)	74
4.5	Percentage of dipole, T-match and tag with a normalised absorbed power lower than the $P_{L_{norm}} = 0$ dB.	77
4.6	Key parameters of statistical studies for backward link	81
4.7	Statistical moments of the differential RCS	81
4.8	Percentage of the dipole and T-matched dipoles with a differential RCS less than the threshold i.e. Δ RCS < -23dBm ²	82
4.9	Percentage of the dipole and T-matched dipoles having $P_{L_{norm}} > 0$ dB in the forward link, with a differential RCS greater than the standard value in the reverse link, i.e. Δ RCS > -23dBm ²	83
I	Pourcentage de dipôles et dipôles T-match ayant $P_{L_{norm}} \geq 0$ dB dans la liaison aller, avec un SER différentiel supérieur à la valeur standard dans la liaison retour, c'est-à-dire Δ SER ≥ -23 dBm ²	118

Abbreviations

ASIC	A pplication S pecific I ntegrated C hip
ASK	A mplitude S hift K eying
CDF	C umulative D istribution F unction
CP	C ircular P olarisation
CV	C oefficient of V ariance
CW	C ontinuous W ave
DUT	D evice U nder T est
EM	E lectro M agnetic
FEM	F inite E lement M ethod
FEA	F inite E lement A nalysis
HF	H igh F requency
HFSS	H igh F requency S tructure S imulator
IOT	I nternet of T hings
LF	L ow F requency
LP	L inear P olarisation
MoM	M ethod of M oments
NEC	N umerical E lectromagnetics C ode
RCS	R adar C ross S ection
RFID	R adio F requency I Dentification
RF	R adio F requency
RMSE	R oot M ean S quare E rror
UHF	U ltra H igh F requency
VNA	V ector N etwork A nalyzer

Symbols

Scalar

A_{eff}	effective aperture area (m ²)
d	distance between the reader and the tag (m)
d_0	any arbitrary distance chosen between a reader and tag (m)
d_{max}	maximum reading range (m)
E_z	vertically polarised incident field (V/m)
\hat{G}	embedded realized gain
G_t	gain of transmitting antenna
G_{tag}	gain of real commercial tag
P_{bs}	backscattered power from the tag (W)
$P_{EIRP_{max}}$	maximum effective isotropic power radiated by the reader (W)
P_i	incident power density (W/m ²)
P_{in}	re-radiated power at the tag antenna (μ W)
P_L	power absorbed by the load of each tag (μ W)
$P_{L_{norm}}$	normalised absorbed power (dB)
P_L^{dip}	absorbed power at the load of the dipole/tag of interest (W)
P_L^{iso}	absorbed power at a load of an isolated dipole/tag (W)
$P_{L_{norm}}^{RMSE}$	root mean square of the $P_{L_{norm}}$ of dipole/tag
$P_{L_{norm}}^{HFSS}$	normalised absorbed power obtained from HFSS (dB)
$P_{L_{norm}}^{NEC}$	normalised absorbed power obtained from NEC (dB)
$P_L^{non-iso}$	modified turn-on power of the tag of interest in the presence of coupling (W)
P_{min}	minimum power required to turn on the chip obtained from Voyantic Tagformance system and Impedance analyser (dBm)
P_t	transmitted power (W)
P_r	power collected by the tag (w)
P_{th}	chip threshold sensitivity (dBm)
P_{VOC}	power induced when the tag of interest is exposed to an incident electromagnetic field (μ W)
$P_{VOC_{in}}$	power induced by other tags includes all the coupling effect (μ W)

R_a	Resistance of the tag antenna (Ω)
R_{in}	Resistance of the input impedance of a dipole/tag (Ω)
R_c	Resistance of the RFID chip (Ω)
Z_a	complex impedance of tag antenna (Ω)
$Z_{c,1}$	high impedance state at the load (Ω)
$Z_{c,2}$	low impedance state at the load (Ω)
Z_{chip}	complex impedance of the chip (Ω)
Z_0	internal impedance of the Tagformance and Impedance analyser (Ω)
Z_{in}	input impedance of a dipole/tag (Ω)
Z_L	load impedance of the dipole/tag (Ω)
Z^{High_L}	high load impedance state i.e. matched load (Ω)
Z^{Low_L}	low load impedance state i.e. short-circuited load (Ω)

Vectors

\mathbf{E}_s	scattered field vector
\mathbf{E}_i	incident electric field vector
\mathbf{g}	column vector of normalized ports' gain
\mathbf{I}	port input currents vector
\mathbf{I}^{SC}	short-circuited current vector
\mathbf{V}	input voltages vector
\mathbf{V}^{OC}	open circuit voltages vector due to the illumination of the electromagnetic field
\mathbf{V}_{in}^{OC}	induced voltage vector including the effect of coupling in the presence of other loaded dipoles/tags
\mathbf{V}_L	port voltages vector at the load
\mathbf{V}_{in}	voltage vector at the tag antenna
Z_{in}	input impedance of a dipole/tag

Greek letters

η_0	free space impedance (Ω)
Γ_{50}	reflection coefficient due to the mismatch between Z_{chip} and Z_0
Γ	reflection coefficient due to the mismatch between Z_{chip} and Z_a
Γ_{int}	reflection coefficient due to the mismatch between Z_L and Z_{in}
σ	radar cross section (dBm^2)
$\Delta\sigma$	differential radar cross section (dBm^2)
λ	wavelength (m)

Matrices

\mathbf{Y}_G admittance matrix of the RFID grid

\mathbf{Z} impedance matrix of dipole array

\mathbf{Z}_{mod} modified impedance matrix of a network of dipoles/tags in the presence of other loaded dipoles/tags

\mathbf{Z}_L diagonal matrix containing the loads of the dipoles/tags

LIST OF TABLES

Chapter 1

Introduction

This manuscript commences with a brief demonstration of the operating principle of Radio Frequency Identification (RFID) technology. To develop a communication link between the reader and the tag, a detailed study of RFID applications and their evolution related to the expansion of the Internet of Things (IoT) is studied. The targeted application domain chosen for this manuscript deals with the analysis of the RFID systems in a context of high tag density, by identifying the factors limiting the deployment of the technology. We built up a brief state of the art of work intended to improve, characterize and quantify the performance of RFID systems when the concentration of tags is high. From this coalescence, we define the objectives of the thesis and we present the methodology and the associated tools that are implemented. We end this part with a general presentation of the organization of the manuscript.

1.1 RFID: from the context to the problem statement

A brief history

The concept of RFID emerged during the Second World War for the identification and differentiation of fighter aircraft of different militaries. In 1948, H. Stockman [1] laid out the basic concepts of RFID which was further followed by F. L. Vernon [2], D. B. Harris [3] and R. Harrington [4] to develop an exploration of RFID techniques that are valid till today. Until the 1970s, RFID technology was mainly used in the military field to control access to sensitive areas such as military bases or nuclear sites. The private sector started showing interest in RFID only in the late 1970s. The 1990s marked a pivotal decade for RFID innovation, as it gained more attention for improving tracking and access applications in various sectors. This included areas like manufacturing, livestock identification, retail stock management (especially textiles), as well as supply chain management in industries and trade.

Working Principle

RFID is a simple wireless system used to control, detect and track objects [5]. It has been developed as an alternative to barcode technology, which requires the scanner to be in close proximity to the object being identified while maintaining direct line-of-sight communication. On the contrary, RFID can be used to detect and read multiple tagged objects at the same time without being in the line of sight. Moreover, the technology has an ever-growing demand with the advancements in IoT, as it can be deployed in automation systems with minimal requirement of manual involvement. RFID systems operate at widely different frequency bands: LF (125–135 kHz), HF (13.56 MHz), UHF (860–960 MHz) and Microwave (2.45 GHz & 5.8 GHz) where the communication techniques and reading range are different depending on the frequency band. Communication between the reader and the tag in the LF and HF band is done by inductive coupling in the near field from a few cm to 1.5m. On the other hand, communication in the far field is done by the electromagnetic field radiated in the UHF and microwave frequency band over a few meters or even a few tens of meters. Among them, the UHF RFID system has drawn a great deal of attention because of its numerous benefits, such as cost, size and reading range. In particular, the reading range of the UHF RFID system is comparatively large, due to the use of electromagnetic fields to transfer power and data. The increased reading range makes it possible for RFID to revolutionize various commercial applications, such as supply chain management. Moreover, the reading range has been considered the most important feature representing the performance of a UHF RFID system. RFID tags can be active, passive or semi-passive tags. An active tag has its own power supply typically a battery to run the chip and sends data to the reader without using the backscattering concept. The semi-passive and passive tags, both use the modulated backscattered signal to communicate with the reader, while the read-range is improved for a battery assisted tag. The protocol used in UHF RFID communication as illustrated in Figure 1.1, is detailed in EPC Gen 2 [6] and ISO/IEC 18000-6 [7] standards. These protocols define the format and structure of the data that is transmitted between the tag and the reader, as well as the rules for how the communication is established and maintained.

The basic infrastructure of a passive UHF RFID system is generally composed of two fixed elements called an interrogator (reader) and a transponder (tag). These elements are shown in Figure 1.1(a). The reader transmits radio waves to power up the tag. In response, the tag sends data back to the reader through a modulated backscattered signal. The data exchange between the reader and the tag is half-duplex and is accomplished in two steps. First, during the forward link or direct link (reader-to-tag), the reader either sends continuous wave (CW) signals or modulated commands to activate the tag. After the tag is selected and interrogated by the reader, it sends data

1.1 RFID: from the context to the problem statement

back in one of the CW periods by switching its impedance between two states in the reverse link or backscatter link (tag-to-reader). This switching of states is between two loads and at the reader side it could be identified as amplitude and/or phase modulation depending on the environment.

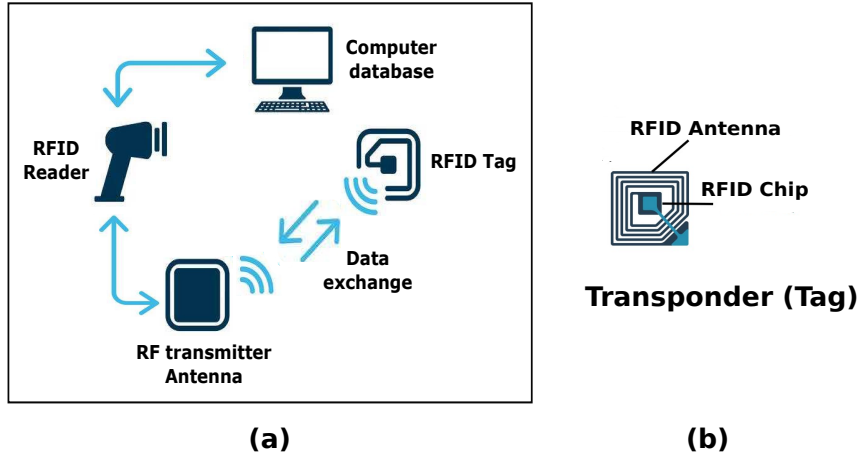


Figure 1.1: Schematic diagram of RFID system

The tag has an application specific integrated circuit (ASIC) chip for storing and processing information, modulation and demodulation of signals, and an antenna for receiving and transmitting RF signals as shown in Figure 1.1(b). Both antenna and ASIC chip of the tag has complex impedances. The chip collects power from the RF signals transmitted by the reader and sends data back to the reader by modulating the backscattered signals as shown in Figure 1.2.

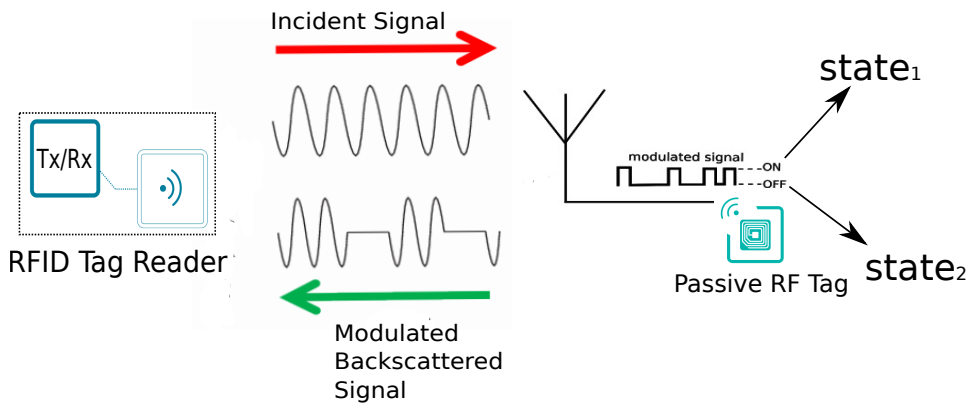


Figure 1.2: Principle of backscattering

The level of backscattering signals highly depends on the complex input impedance of the chip associated with the tag. Data exchange is done by employing a load modulation scheme by switching its impedances between two states. One of the impedance states is usually high which means matched to the antenna and another is low which

could be short-circuited or open-circuited to provide a significant difference in backscattered signal. An anti-collision algorithm is used when multiple tags respond at the same time to increase the detectability of RFID tags [8], [9]. Nevertheless, the reader may initiate several rounds of interrogation until it hears all the tags in that area.

Current and emerging applications

RFID technology has played an important role in industrial and commercial logistics. It has gained more attention due to the growing need for the identification, traceability, and monitoring of the environment in manufacturing companies, agriculture, hospitality, parking management and transportation sectors, and opening up new development of perspectives with the growth of the Internet of things. In agriculture, it has been used to identify and track livestock animals and it is one of the earliest RFID applications. Researchers suggested that this tagging technology used in traditional agriculture could be expanded towards a smart approach in order to monitor the quality of crops/harvest. Recent studies show that RFID tags can be associated with different types of sensors to improve the harvest quality and safety of perishable goods such as fresh vegetables/fruits as they have short shelf lives which could reduce food wastage [10]. However, despite its numerous advantages, RFID technology still brings out many challenges and it is important in particular to make data more reliable i.e. many times tag fails to be identified by the reader because of either the reading distance between the reader and the tag or due to the collision with other RF devices and all of this is strongly correlated with the surrounded environmental conditions [11]. For inventory applications in the field of logistics and supply chain management, where RFID technology can be used to improve productivity, the major obstacle is the implementation costs which can be significantly higher to make the communication process more reliable between the reader and the tags. Also, these scenarios are often complex due to the close environment around the tags that would be known with uncertainties and could have heavy metallic objects and other surrounding radiating elements which can interfere with and modify the quality of the tag-to-reader communication link.

Even though the work on RFID technology has existed for more than 60 years, the problem linked to the high density of randomly distributed RFID tags only appeared recently. It corresponds to the applications associated with industrial and commercial logistics as shown in Figure 1.3.

In the following examples, tags can be found in large numbers and placed at a very close distance to each other:

- The warehouse where tagged objects are stacked.

1.2 State of art

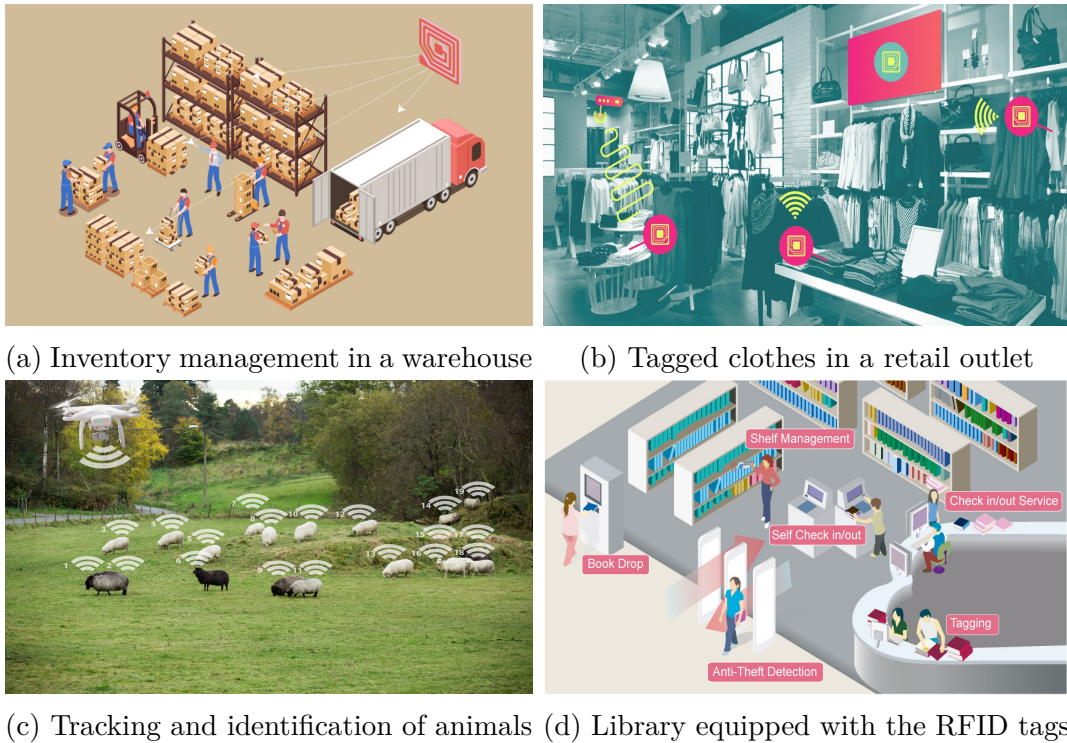


Figure 1.3: Practical examples of UHF RFID technology in a high-density context (Web figures)

- Tracking linens, uniforms and garments in a retail outlet.
- Livestock management entails managing cattle and supervising farm workers.
- Library systems for self-checkout terminals and automated media return.

As the position and orientation of tags in a high-density context are often random parameters as shown in Figure 1.3, the matching and radiation properties of a tag would experience random variations, which differ accordingly. In such a frame of reference, the large number of RFID tags present in an uncontrolled environment and thus a strong electromagnetic coupling among the radiating elements and with the surrounding objects degrades the performance of the RFID system.

1.2 State of art

Our current research is focused on studying RFID communication links in a high density context. The existing literature identifies a common issue which is the degradation of the link budget when reading co-located tags. Currently, this difficulty is addressed by different existing solutions which bring improvements to various aspects, ranging from the reading system to the underlying algorithms. Finally, due to the random spatial distribution of tags, the use of statistical techniques need to be considered.

The state of the art is presented through the 3 following axes which are of interest for this research work.

Mutual coupling effects in RFID

We know that the positioning, orientation and distance between the antennas as well as their intrinsic parameters such as polarisation, working frequency and radiation pattern influence the intensity of mutual coupling and therefore may impact the detection performance in an RFID system. In the RFID context with a high density of tags, certain studies empirically highlight the degradation of the radio link related to the electromagnetic interactions between the antennas [12]. For example, authors in [13] study the performance of a UHF RFID system in a real case scenario for retail store application. Facing this approach, it is possible to introduce physical models including the coupling effects which allow to quantify the impact of coupling in a high density of tags on the performances of an RFID link.

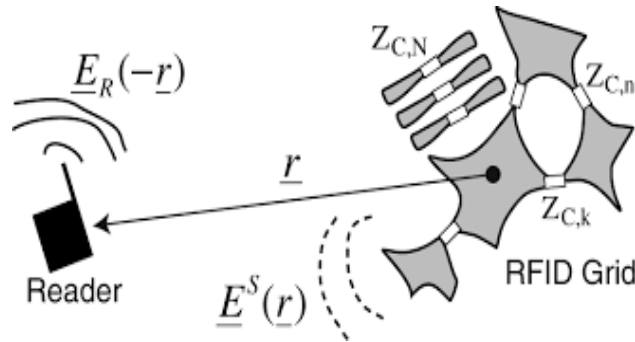


Figure 1.4: Communication between a reader and a set of multiple RFID tags terminated with their chip impedances. [14]

In this section, we analyse the work presented by [15], with the purpose to extend the given RFID N-port equations to develop our power link budget model which will be used later in our study to quantify the forward and reverse link in a high-density context. To model the communication between the reader and multiple RFID tags in a complex system, G. Marrocco was inspired by the work of JR Mautz and RF Harrington presented in [16], having N-port circuit based on Thevenin and Norton models. He developed an RFID grid in [14] and [17], to represent a set of tags where the microchip serves as a termination load (Figure 1.4) and the impedance matrix take into account the mutual impedances between tags. By using this model, he was able to depict more accurately the complex interactions between multiple tags in an RFID system. The balance equations for the N-port network were derived, which describe the power flow and signal transmission between the reader and tags. His work allows a better understanding and modelling of a complex RFID system.

1.2 State of art

The N-port system collecting the incident electromagnetic wave is modelled by an equivalent Thevenin voltage generator circuit, shown in Figure 1.5. The embedded realized gain (\hat{G}_n) at a desired polarisation angle of an incident field is given as,

$$\hat{G}_n = 4\eta_0 R_{C,n} |[\mathbf{Y}_G]_n \cdot \mathbf{g}|^2 \quad (1.1)$$

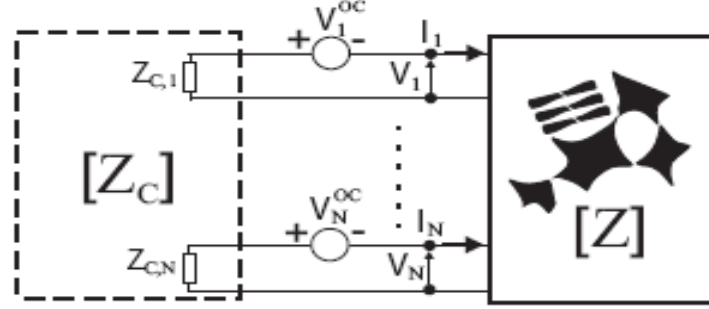


Figure 1.5: Thevenin network model for an RFID grid. [14]

where $[\mathbf{Y}_G] = [\mathbf{Z}_G]^{-1}$ with $\mathbf{Z}_G = [\mathbf{Z} + \mathbf{Z}_C]$ composed of the impedance matrix of the grid as well as the diagonal matrix of chip impedances $[\mathbf{Z}_C] = \text{diag}(Z_{C,1}, Z_{C,2}, \dots, Z_{C,N})$, in $[\mathbf{Y}_G]_n$ the index n denotes the n th line of the matrix, \mathbf{g} is the column vector of normalized ports' gain and $R_{C,n}$ is the resistance of the n th chip impedance. The author concluded that the embedded realized gain of a tag of interest is degraded due to the coupling introduced by the surrounded tag in a side-by-side configuration compared to the case when it is isolated. This deterministic model encouraged us to analyse both RFID links using a grid representation of tags as illustrated in Figure 1.5.

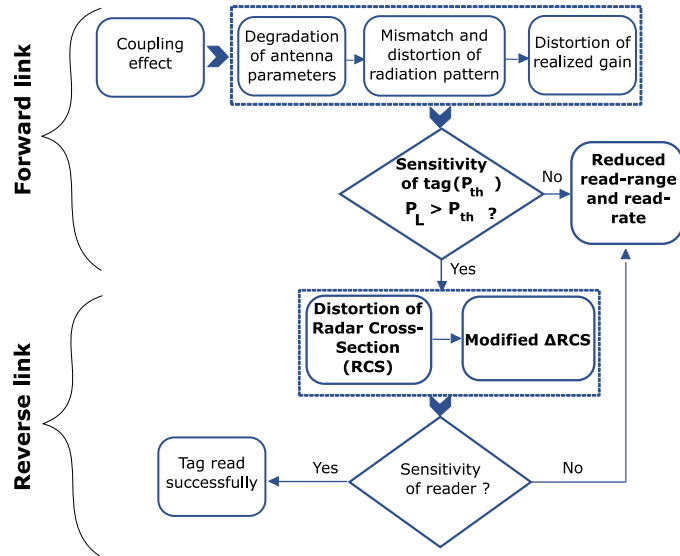


Figure 1.6: Effects of mutual coupling on the forward and reverse links of an RFID system

In an existing work in ESYCOM laboratory, a former PhD student I. Adjali anal-

used in his work [18], two degraded antenna parameters as a result of coupling, i.e. the mismatch and the distortion of the radiation pattern of a surrounded tag. Numerical estimations using commercial simulators as well as an analytical technique, based on IEMF method [19], had been developed. In [20], I. Adjali quantified the forward link in terms of the degradation of matching properties of the isolated driven tag modified in the presence of neighbouring tags. The observable in this paper is the reflection coefficient of surrounded tags which is a measure of associated mismatch and in turn may degrade the RFID system performance. This research work mainly focused on exciting one tag at a time with a voltage source of 1V while keeping other tags terminated by a load. In our work, we intend to illuminate the tags with an incident wave and the actual induced voltage is going to be estimated. Consequently, we consider a more realistic scenario where all the tags are illuminated simultaneously while they are terminated with their respective loads. Besides, we intend to go beyond the mismatch and the radiation pattern which are antenna parameters and get closer to system performance quantifying parameters, such as the read-range.

In Figure 1.6, we can identify two crucial observables that can be evaluated in RFID forward and reverse links:

- Minimum activation power: This is the power required to turn the tag’s chip on, which depends on the chip’s sensitivity.
- Re-radiated power: This parameter relates to the reader’s sensitivity and can be explored in terms of radar cross section and the associated differential radar cross section.

Existing solution to overcome the degradation phenomenon

To address the issue of coupling between tags that can decrease reading speed and distance, a potential solution is to increase antenna diversity by deploying multiple reader antennas as implemented in [21]. Deploying RFID readers with a variety of antennas and implementing solutions that affect the reading structure can result in a significant increase in cost and open up various challenges during deployment. While using hand-held readers to manually move the antennas may be a low-cost option, it is not the most optimal choice for real-time management. Employing low scattering tag antennas [22], introducing load switching at the neighboring tag antennas [23] or stirring the surrounding environment of the tags [24] have also been proposed. We can also name other techniques, such as post-processing of data, depointing of array antennas, frequency diversity, and optimized communication protocols, that can be used to address these issues.

The aim of this thesis is not to suggest alternative solutions to enhance the existing methods for improving the reading range and reading rate. Instead, it focuses on contributing to the analysis of above mentioned parameters by utilizing statistical methods. The objective is to assist one in determining the best-suited RFID architecture by keeping the prior knowledge of coupling mechanism under various physical parameters of the system such as matching and radiation properties, chip's and reader's sensitivity, polarisation of the incident wave and potentially other factors.

Statistical Modeling

The electromagnetic coupling between antennas is a deterministic phenomenon, that could require a statistical approach if the unknown spatial distribution of tags adds a random dimension to the problem. Consequently, a purely deterministic modelling is not realistic and the development of statistical modelling is required. In the literature, statistical analysis for RFID technology has been mainly used in two categories: classification problems and tag readability assessment. While the first category is considered to be out of the scope of this research work, the second one focuses on the same objective which is to assess the reliability of an RFID system. These studies suggest benchmarking of RFID tags in different environment and subject to simultaneous or separate variation of different parameters, such as: tag size, distance from the reader, tag orientation with respect to reader, materials used for embedding tags, etc. The readability of RFID tags has been analysed using various experimental approaches, followed by statistical analysis of the empirical data using regression models or other advanced techniques. The statistical analysis can be based on variability of the performance metrics of one tag [25], [26] or multiple tags [27], [28] versus the surrounding environment.

To our knowledge, statistical analysis has not been applied before in the physical layer of an RFID link, notably to assess the electromagnetic phenomenon of coupling. A Monte Carlo approach [29] refers to a computational technique that involves the use of random sampling of input variables to simulate and analyze the output of complex systems or processes. In Monte Carlo simulations, a large number of random samples are generated, and the behaviour of a system is analyzed based on these samples. Despite the poor efficiency of Monte Carlo [30], the simplicity of its implementation makes it a good candidate for the analysis of uncertainties in various electromagnetic and antenna problems. In the RFID context, by randomly generating different scenarios, such as orientation and placement of the tags and analyzing the read rates of these scenarios, statistical analysis can be used to identify the optimal settings for a given RFID scenario.

1.3 Objectives of the thesis

This thesis deals with UHF RFID communication for which a set of randomly distributed RFID tags are concentrated in an electrically small area. In a high-density context of tagged objects, both RFID links (forward and reverse) are subject to degradation, among other reasons, as a result of the electromagnetic coupling between tags and due to their surrounding environment. This concentration decreases the performance of the tag antenna which in turn causes the degradation of its read range and read rate. In this context, the objective of this thesis is to set up a simulation model which is closer to a realistic RFID system than the model studied in the previous PhD work [18]. In this work, an electromagnetic field is used to illuminate all the tags simultaneously instead of applying an external current source to an individual tag. A circuit model is presented to analyze the degradation of the RFID system's performance, primarily focusing on two parameters, i.e. the minimum threshold power required to turn on the tag in the forward link, and the backscattering phenomenon related to the reverse link is studied in terms of Radar cross section (RCS) and the associated Differential radar cross section (Δ RCS). The position and the orientation of the tags are random parameters in a high-density context due to which a purely deterministic approach cannot describe the evolution of threshold power and RCS/ Δ RCS realistically. Therefore, the study would be extended further in a statistical aspect to consider the impact of high-density context, which is possible through a large number of simulations. In the scope of this thesis, the following are the steps involved in formulating the objective in various phases:

- We use real commercial tags to analyse the key parameters of both RFID links. To this aim, an appropriate measurement setup was designed to characterise the sensitivity of the chip and the impedance of both the tag antenna and the chip using three pieces of equipment, i.e. Voyantic Tagformance system, an Impedance Analyzer and a Vector Network Analyzer. The tag antenna impedance as well as the chip impedance constitute a complete model to be used in an electromagnetic simulator such as HFSS. A simplified model of an RFID system composed of half-wave dipoles and T-matched dipoles has been presented with the aim of getting a low-cost model to be simulated by NEC.
- The understanding of physical phenomena underline the impact of degradation in a high-density context is studied by modelling a classic network of a random array of tags. This network model is analyzed by measuring the following parameters of an RFID system,
 - i **The Power budget:** The impact of coupling on the position and orientation of antennas under various conditions such as the density of the antennas,

1.4 Organisation of the Manuscript

polarisation of the incident wave and the angle of incidence has been studied firstly in terms of power budget analysis of different configurations using the proposed conventional network model. The study delves deeper into two critical power levels of this power budget analysis: the absorbed power in the forward link and the backscattered power linked in the reverse link.

ii **The absorbed power associated with the forward link:** The absorbed power describes the amount of power required to turn on the passive RFID tags' chips when they are illuminated by the electromagnetic fields transmitted by the reader. In the forward link, this power is absorbed by the chip to run its circuitry to initiate the communication between the reader and the tag. The goal is to observe the similarities or correlations between the three chosen antennas.

iii **The backscattering phenomenon associated with the reverse link:** After powering up by the electromagnetic field received from the reader by the tag, the communication between the tag and the reader is established by switching its chip impedance between the two distinct states which results in a modulation of the signal backscattered towards the reader. The backscattered field of the tag can be analyzed in terms of its mono-static radar cross section. The modulation of the signal depends on the difference between the two chip impedances and is estimated in terms of differential radar cross section.

- Based on the concept of high-density context, purely deterministic modelling is not realistic and a large number of random profiles of tags/dipoles are generated to analyze the antenna's parameters. A development of a statistical approach is required to quantify the impact of degradation in both RFID links of highly coupled tags.

1.4 Organisation of the Manuscript

Chapter 2, outlined a simple and practical methodology for measuring the sensitivity and impedance of RFID chips and provided experimental results for two RFID chips. we also highlighted the effect of randomness in the context of a high density of loaded tags. On account of similar radiation behaviour observed in [31] and statistical similarities observed in [20], the set of N tags is modelled by a set of dipoles, with or without a T-match network. The automated simulation setup has been presented for the simplification of the tag antenna after discussing the observed similarities between the behaviour of the RFID tag and a half-wave dipole (with and without T-match) in order to obtain a low-cost model. Two electromagnetic simulators (NEC and HFSS)

have been discussed in detail, which will be used later in the following chapters to analyze the complete link budget of RFID systems.

Chapter 3, presents a network grid of an RFID system consisting of randomly distributed N-loaded tags over a specific area, illuminated by an incident electromagnetic field. The effect of randomness versus the polarisation of the incident field as well as the mutual coupling is evaluated in this chapter in terms of power budget analysis. The formulation of the absorbed power at the load level and the re-radiated power of a tag are of interest in the forward and reverse links respectively are also presented in this chapter. The re-radiated power from a set of loaded scatterers is then estimated in terms of scattered electromagnetic field, which is used to calculate the related Δ RCS of the tags. The results discussed in this chapter are mainly obtained from the electromagnetic simulators (NEC and HFSS) and for the deterministic cases of dipoles, with and without T-match and real commercial tags.

In Chapter 4, a statistical study of the impact of coupling and the polarisation of an incident field is analysed on the random orientation of dipoles (with or without T-match) and tags. The degradation of the absorbed power in the forward link and the differential RCS in the reverse link are statistically quantified as a function of the density of dipoles and tags. Using the HFSS simulator, a statistical study of the forward RFID link on these commercial RFID tags is carried out and the result is compared to the half-wave dipoles and T-matched dipoles.

Finally, the conclusion and future perspective have been presented.

Chapter 2

Characterisation of an RFID tag and its simplified model

In practical applications, a tag antenna can never be completely isolated in its environment. It is always subjected to the impact of interference caused by the parasitic elements present in the surrounding environment which includes several diffracting or reflecting objects, metallic things, and other electronic devices. In our case study, the tag antenna is perturbed by other surrounding tags. Consequently, the electromagnetic interactions among the tag antennas degrade the performance of the RFID system and cause a reduction in read range and read-rate. A passive UHF RFID system is composed of a reader antenna and a tag which includes an antenna and a chip. In the forward link, the tag is powered up thanks to the electromagnetic field introduced by the reader. In the backward link, the responding tag switches its chip impedance between two distinct states which results in a backscattered field towards the reader to be detected. As presented in the context of this study, we wish to study a statistical analysis of highly coupled tags due to the complexity and diversity of the scenarios discussed in the introduction. Obtaining converging results statistically requires an analysis carried out on a large computation volume with a large number of iterations. Therefore, imposing an efficient and low-demand model in terms of computing capacity is important. In this context, both RFID links are subject to degradation, among other reasons, as a result of the electromagnetic coupling between tags. The higher the density of tag antennas in a given area, the greater the coupling effects appear on the RFID communication link.

In this chapter, we focus on modeling an RFID system that comprises a randomized arrangement of tag antennas. The study aims to analyse the effect of randomness on the link budget in terms of position, orientation, and density of tags placed within a predetermined surface area. Prior to conducting the analysis of the randomness of the tags, we must begin by characterizing the RFID tag and the attached integrated chip

that makes up the RFID system. An appropriate measurement setup was designed to do this characterisation, which includes three steps, firstly, the impedance and sensitivity of the chip are measured using two pieces of equipment i.e. Impedance analyser and Voyantic Tagformance system. Second, the impedance of the tag antenna without chip, was measured using a differential probe and vector network analyser (VNA). The measured impedance of the tag antenna is then incorporated into an electromagnetic simulator (EM), such as HFSS. The third aspect of this characterisation involves assessing the tag antenna and chip as a unified entity. We conducted this evaluation using the Voyantic cabinet, connected to the Voyantic Tagformance system. The goal was to determine the maximum tag's read range, which includes both the RFID links that power up the tag (the forward link) and the communication back to the reader (the reverse link). After having the characterisation of real RFID tags, it would be interesting to effectively compare commercial RFID tags with other simplified antennas. Therefore, a set of randomly distributed commercial tag antennas is then modeled by a set of half-wave dipoles. Another impedance-matching technique has been adapted by employing a T-match network with dipoles to get a complex conjugate of antenna impedance allow for an efficient comparison with the real RFID tags. Two electromagnetic (EM) simulators, NEC and HFSS, were employed to integrate the design of a dipole antenna, both with and without a T-match network. However, the inclusion of a tag was exclusively carried out in HFSS due to its complex structure. Subsequently, both NEC and HFSS were utilized for analyzing the link budget of the proposed RFID system in the later chapters of this thesis. To commence our study, it is imperative to begin by outlining the tools and methodology chosen for the characterisation of real commercial RFID tags. Following this, we will then introduce the real tags and their simplified model.

2.1 Tools and techniques used in the study

This section elucidates the measurement bench and simulation tools used to characterise the real commercial tags. Firstly, the two pieces of equipment included in the measurement bench to characterize the chip are presented. Following that, we present the characterisation of the tag antenna without a chip using a differential probe and a VNA. The subsequent section delves into the discussion of the Voyantic cabinet, which is utilized for measuring both the tag and chip together. Finally, the two EM simulators, NEC and HFSS are discussed, which will be used later in our work for the analysis of the power budget and the key parameters of the forward and reverse link explicitly.

2.1 Tools and techniques used in the study

2.1.1 Measurement bench to characterise the UHF RFID chips

The measurement bench shown in Figure 2.1, is used to measure the impedance of the UHF RFID chips connected to the RFID tags. This bench consists of a Keysight Impedance Analyser E4991B that works for the characterisation and evaluation of electronic components, semiconductor devices, and materials. This piece of equipment works at a frequency range of 1 MHz to 3 GHz with a power sweep limit of -40 dBm to 1 dBm. This device is deployed with a fixture component 16194A to connect the device under test (DUT) to the analyser. The two electrodes at the fixture component are used to properly hold the DUT, shown in Figure 2.1. The latch is used to push the end of the DUT or to adjust the pressure towards the electrodes in order to have a proper connection between them. Equipment calibration is a very important step in the measurement process. The keysight 16195B calibration kit consists of four components, i.e. open load, short load, 50-ohm load and low loss load and is used to calibrate the impedance analyser. This calibration comprises a two-step procedure. First, the impedance analyser is calibrated without the fixture component using the provided calibration kit. Then, the fixture component is affixed to the analyser, and a second calibration step is performed for the fixture component calibration using the fixture component calibration option on the impedance analyser. This needs to be calibrated considering the short and open circuit connection between two electrodes of the fixture component. The spacing between the two electrodes for creating the short and open connection depends on the dimension of the DUT.

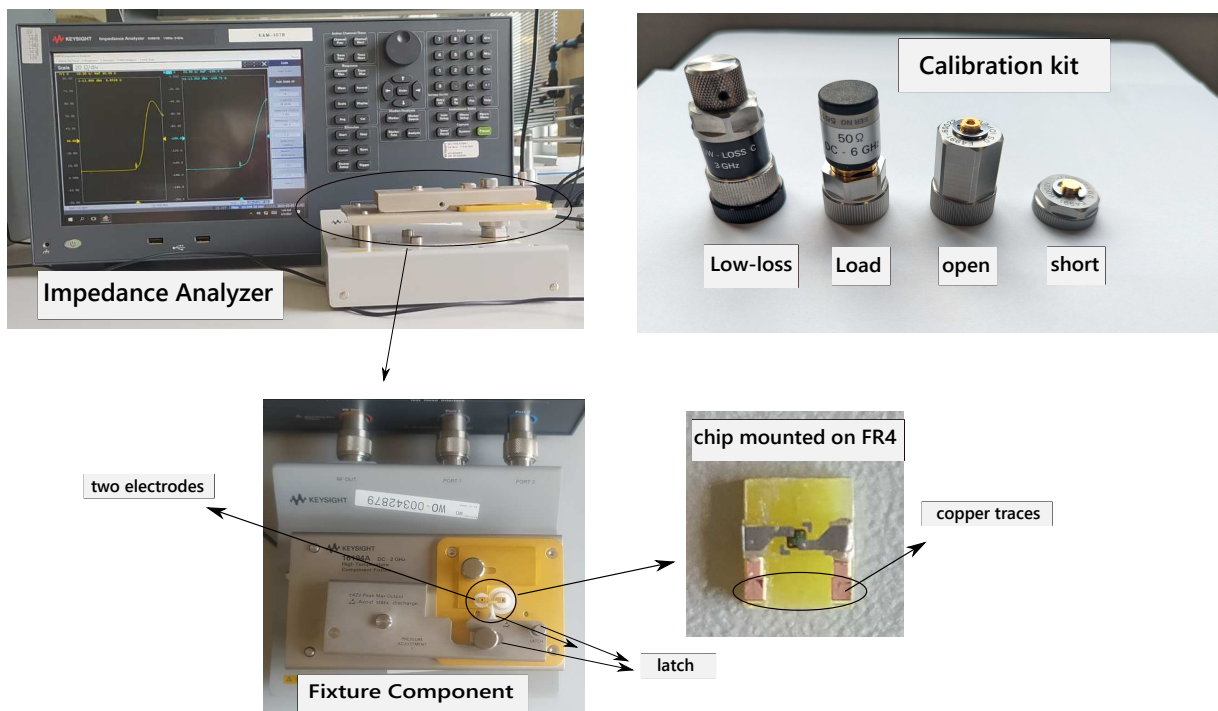


Figure 2.1: Measurement bench to measure the complex impedance of the UHF RFID chip.

In our study, the DUT is a chip (Higgs-3 [32]) that is very small in size (around 1 mm) and needs to be handled properly to avoid any unwanted reflections which could interfere with the results. Therefore, we use FR4 substrate, as a base to paste our chip as shown in Figure 2.1. The copper is etched onto the surface of the FR4, and usually, the two ends of the chip are soldered onto the copper traces to have a good base for the chip. However, in our case, the chip does not have two ends to be soldered as it is already connected to a commercial tag. So we used a slight part of the printed antenna attached to the chip in order to mount it on the FR4 substrate with the conducting glue. The dimensions of the copper trace on the FR4 substrate depend on the dimensions of the electrode at the fixture component. This dimension of the FR4 substrate depends on the size of the calibration kit short circuit component we used for creating a short between two electrodes, in order to avoid any unwanted disturbance in the results of chip impedance.

The second piece of equipment in our measurement setup is the Voyantic Tagformance system. It is a complete measurement solution for analyzing the performance of RFID tags and tagged items. The system consists of the Tagformance measurement device, one or more software packages, anechoic measurement cabinet and accessories that complete the system. It has the functionality of the RFID reader over a large frequency band (from 800 to 1000 MHz), it can send commands to the tag and receive tag replies. We used Tagformance to measure the minimum power required to wake up the chip. It varies its transmit power until the chip is turned-on. For this step, the DUT or the chip (in our study) is soldered to a standard 50 Ω SMA connector assembly as shown in Figure 2.2. After connecting the chip-connector assembly to the Tagformance, one can measure the minimum transmitted power required to wake up the chip, which will be further used to characterise the chip attached to the RFID tag.



Figure 2.2: Experimental setup to measure the threshold of the chip, connected with SMA.

2.1 Tools and techniques used in the study

2.1.2 Measurement bench to characterise the UHF RFID tag antennas without chip

The experimental setup depicted in Figure 2.3 is designed for the measurement of the complex input impedance of RFID tags lacking integrated chips. This configuration comprises a Voyantic cabinet [33], a ROHDE & SCHWARZ ZNB8 Vector Network analyser (VNA), and a calibration kit for VNA calibration. The RFID tag antenna is positioned inside the Voyantic cabinet to minimise unwanted signal reflections. Two terminals of the differential probes are soldered to the centre of the tag antenna for excitation purposes, as demonstrated in Figure 2.3. The remaining two ends of these probes are connected to the two ports of the VNA. This methodology of exciting the antenna using a differential probe technique [34], is employed to minimize the impact of cable connections on the antenna's performance, which is particularly critical for electrically small antennas or those with a symmetric feeding system. A complete 2-port calibration is then performed following the procedure outlined in [18] and [34]. To calibrate the VNA system, an open circuit (nothing connected), a short circuit (a direct short), and a load (50-ohm impedance) are connected to the two VNA ports individually. After performing open, short and load calibration, disconnect them and connect thru load at the two ports of VNA as an end-to-end connection between them. This calibration will remove errors introduced by the cables and connectors. With the calibration complete, one can now characterize the DUT (tag antenna, in our case) and perform measurements for the complex impedance.

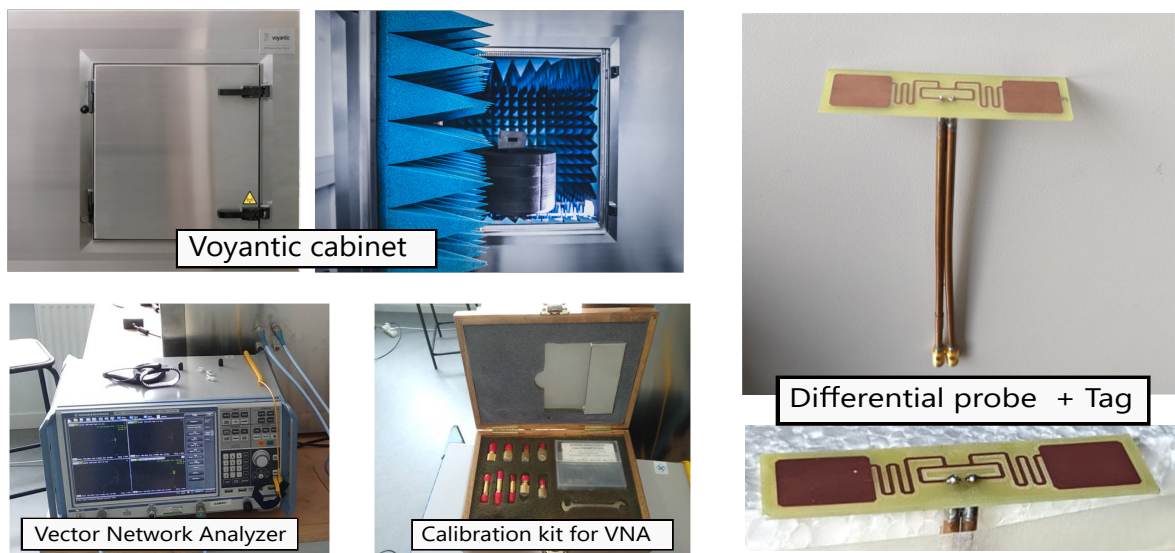


Figure 2.3: Experimental setup to measure the complex impedance of UHF RFID tag without a chip.

2.1.3 Measurement bench to characterise UHF RFID tag antenna and chip together

This measurement is conducted using the experimental setup shown in Figure 2.4, which includes the Voyantic cabinet and the Tagformance system. Before conducting measurements for the read range of an actual RFID tag, it's essential to validate the measurement setup. There is no specific calibration step required in this experimental setup, the only thing is that the manufacturer [33] provides a reference tag with pre-saved path loss measurements in its memory. These saved path loss measurements will be used for calculating the read range of the reference tag. This validation process involves comparing the test results obtained using the reference tag with the data stored in the Tagformance software's memory for reference to ensure the setup's accuracy and reliability. The measurement setup is all set to proceed further if the test results with the reference tag is similar to the pre-saved data in its memory.

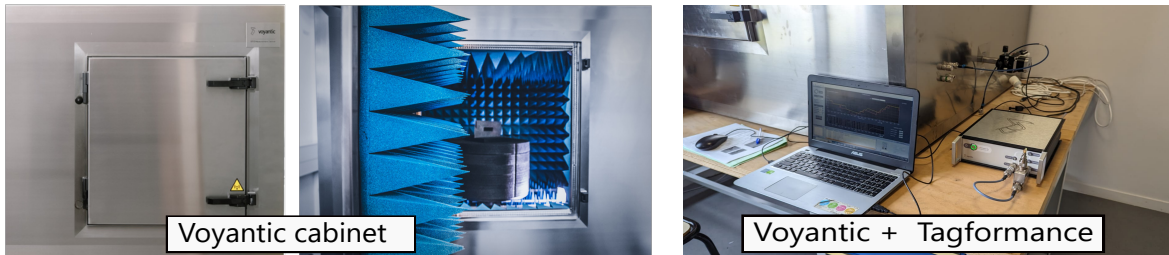


Figure 2.4: Experimental setup to measure the read range of UHF RFID tag.

2.1.4 Simulation tools

The second part of useful tools for our study are EM simulators, i.e. NEC and HFSS. They both are popular software tools used for electromagnetic analysis and simulation. While they serve a similar purpose, they have some key differences. NEC is based on the Method of Moments technique, which discretizes the structure into small segments and solves the integral equations to determine the electromagnetic behaviour. It is commonly used for analyzing antennas and structures in the radio frequency and microwave frequency range. It offers a range of analysis for antennas, such as radiation patterns, input impedance, and near-field analysis. It also supports wire structures and simple dielectric structures (in advanced versions such as NEC3 and MININEC but with limited specifications). It allows the user to specify excitation sources, such as a current or a voltage source, to simulate different feeding methods [35]. It is a popular software tool for modeling and simulating wire antennas, including various types of dipole, Yagi-Uda, and loop antennas, among others. HFSS, on the other hand, is based on the Finite Element Method (FEM), which subdivides the structure into

2.2 Characterisation of the RFID tags and the chip

small elements and solves differential equations to predict the electromagnetic response. HFSS is capable of simulating electromagnetic phenomena in a wider frequency range, including microwave frequencies and beyond. It is a comprehensive tool with extensive capabilities for simulating complex 3D electromagnetic structures, including antennas, waveguides, transmission lines, and integrated circuits. It provides detailed results like S-parameters, electromagnetic near and far fields, and radar cross section [36]. The software offers advanced features like adaptive meshing, automatic optimization, and parametric analysis for efficient design exploration and optimization. Both NEC and HFSS provide accurate results; however, the accuracy can depend on factors like mesh density, discretization, and convergence criteria. HFSS is best suited for complex structures and high-frequency analysis while NEC is more efficient for wire-based simple structures.

2.2 Characterisation of the RFID tags and the chip

Continuing with the tools and methodology mentioned above in terms of measurement and simulation, this section focuses on the incorporation of real commercial RFID tags. These tags will be characterised first, along with their chips. The primary objective is to perform an in-depth analysis of the key parameters of both RFID links for our proposed RFID system. Before delving into the characterisation of the tag and its attached chip, it is imperative to provide an introduction to the real commercial tag itself which is presented in the following subsection.

2.2.1 Real commercial UHF RFID tag

We used real commercial UHF RFID tag antennas to investigate the quality of both RFID links, which are manufactured by ALIEN Technology (ALN-9662), [31]. A schematic of the tag with its dimensions is shown in Figure 2.5. It is functional in the UHF frequency band ranging between 840–960 MHz. The integrated chip of the tag is connected to the antenna through a matching network, commonly called a T-match network. The design of this tag utilizes a printed meandered dipole that is loaded capacitively. Due to its intricate structural design, in all the following studies, the tag’s antenna has been simulated using Ansys HFSS electromagnetic simulator.

The communication performance between the reader and a tag strongly depends on the matching between the tag’s chip and the tag antenna. To ensure power optimization, the input impedance of the antenna must be the complex conjugate of the chip’s input impedance. In this contribution, a measurement method is presented to determine whether the tag antenna impedance is actually in the conjugate matched with the chip input impedance or not. The equivalent circuit model of the chip of

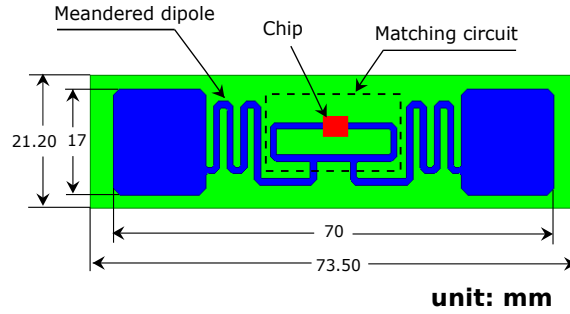


Figure 2.5: Schematic of real commercial UHF RFID tag (ALN-9662).

ALN-9662 is given in [32]. This chip has resistance R_p in parallel with a capacitance C_p equal to 1500Ω and 0.85 pF as per the data sheet provided by the manufacturer [31]. This indicates that the tag antenna has an input impedance characterised by a low resistive component and a significantly high reactive component, designed to facilitate efficient power transfer within the RFID system. In this section, we describe the sensitivity and the impedance measurement method for the Higgs-3 chip using the impedance analyser and compare it with the impedance of the tag antenna measured using a differential probe technique explained in [18].

2.2.2 Characterisation of the RFID tag

The first thing to measure in an RFID tag is its attached chip. The measurement bench to characterise the chip (Higgs-3) installed on real commercial tags (ALN-9662) was presented in Figure 2.1. The procedure for measuring the chip impedance is described below. Following the calibration steps of the impedance analyser over the frequency band of $850 \text{ MHz} - 950 \text{ MHz}$, the initial step involves measuring the minimum turn-on power required to wake up the chip. This power measurement will be utilized in the subsequent step to measure the chip impedance across the frequency band. We are using three different samples of Higgs-3 chip for the measurement process. The measured complex chip impedance of the chip using an impedance analyser is shown in Figure 2.6, for two frequencies, i.e. 868 MHz and 928 MHz , chosen arbitrarily in order to measure and observe the behaviour of the wake-up power (P_{\min}) of the chip. It is observed that the measured chip impedance in absorbing mode is low for lower power and it drastically changes at higher power levels.

It can be seen that the chip did not respond till it received enough power to get turned on, which is approximately greater than -9 dBm (c.f Fig. 2.6) and it could be any value after -9 dBm visibly as per the wake-up response of the chip for both frequencies. The chip impedance of any RFID chip can be obtained from an impedance analyzer as a function of turn-on power (P_{\min}) for different frequencies. If we choose one frequency then what would be the value of P_{\min} to be given to the impedance

2.2 Characterisation of the RFID tags and the chip

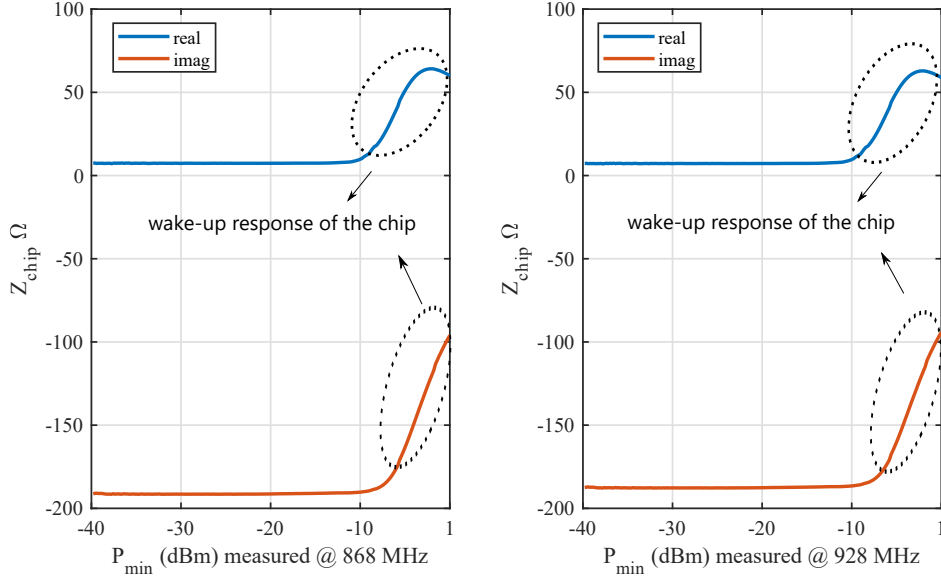


Figure 2.6: Measured impedance of the UHF RFID Higgs-3 chip over a range of input powers in the impedance analyser.

analyzer to get chip impedance from impedance analyzer. Therefore, at this point, the important parameter to choose is the correct value of P_{\min} which will be used in the second step to measure the chip impedance over the frequency sweep. Therefore, we chose the Voyantic Tagformance system. It allows one to find the P_{\min} which can not be reliably found only from the impedance analyser in the form of impedance behaviour versus wake-up power sweep as shown in Figure 2.6.

Following the mentioned methodology of chip-connector assembly connected to the Tagformance, explained in section 2.1.1, the measured minimum power required to activate the chip is, approximately similar over the frequency band from the Tagformance. We intend to choose the working frequency of 928 MHz (arbitrarily) and the wake-up power, $P_{\min} = -7.2$ dBm is measured for this particular frequency in Tagformance. Since the shown chip-connector assembly is usually lossless and it was found to be less than -0.7 dB. The mismatch due to the internal impedance (Z_0) of both the Tagformance system and the impedance analyser is calculated as [37],

$$|\Gamma_{50}|^2 = \left| \frac{Z_{\text{chip}} - Z_0}{Z_{\text{chip}} + Z_0} \right|^2 \quad (2.1)$$

where Z_{chip} is the complex chip impedance and $Z_0 = 50 \Omega$. Then the threshold power sensitivity (P_{th}) of the chip can be calculated as [37],

$$P_{\text{th}} = P_{\min}(1 - |\Gamma_{50}|^2) \quad (2.2)$$

The P_{th} of the chip is calculated after measuring the Z_{chip} . Following the above-

mentioned experimental setup (section 2.1.1), we first measured the complex impedance of the three samples of Higgs-3 chip and compared the values, as shown in Figure 2.7.

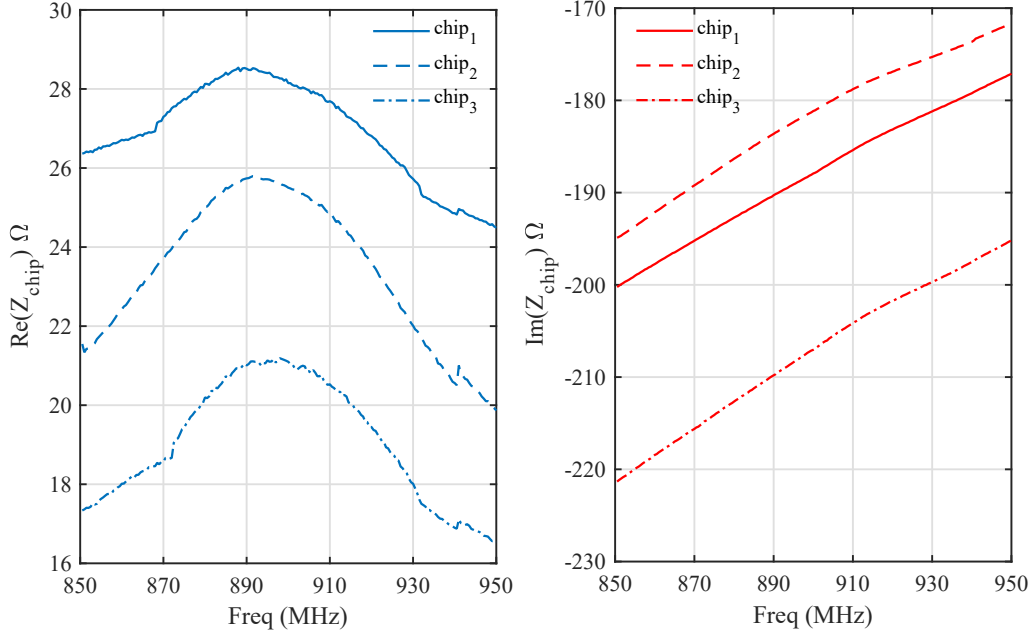


Figure 2.7: Measured real and imaginary parts of the impedance of three samples of Higgs-3 chip using the impedance analyser.

It is observed that the measurements obtained from the three chips are highly inconsistent. Despite observing similar frequency dependence changes in both real and imaginary parts, the chip impedance exhibits important variations from one chip to another. The difference in measurements may arise from the compact strap-based packaging of Higgs-3 in the ALN-9662 tag, making precise measurement challenging. Also, it could be due to the chip being low-cost and issued from a bulky production compromising its accuracy.

Given that the measurements are not repeatable, the measured Higgs-3 impedance can not be used further in our study. However, we can use the simulated chip impedance of Higgs-3 from the datasheet [32] later in our work. To verify our experimental setup, we decided to employ an alternative chip manufactured by the same company, Alien Technology, instead of the Higgs-3 chip. The replacement chip, known as the Higgs-9 [38], is the latest integrated chip offered by the company with thicker packaging which was easy to handle in measurement procedures. It is a choice to get this chip with thicker packages to verify our experimental setup and is claimed to possess superior features such as increased storage capacity, higher sensitivity, reduced cost and dimension.

2.2 Characterisation of the RFID tags and the chip

The chip impedance is measured using the same procedure explained above in section 2.1.1 and P_{\min} is first measured from Tagformance, as shown in Figure 2.8. To verify the experimental setup, the chip impedance of a few samples of the Higgs-9 is used to ensure that we obtain similar values from different samples, without uncertainties like in the case of the previous Higgs-3 chip.

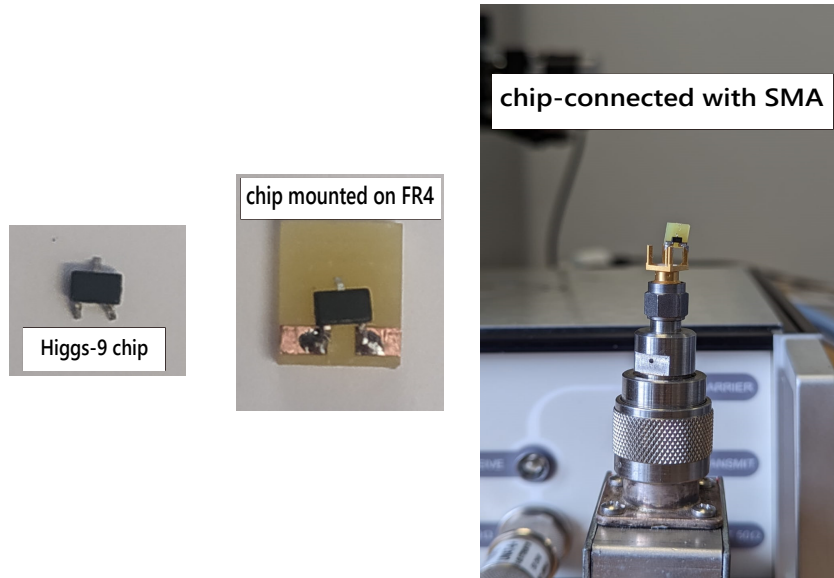


Figure 2.8: Higgs-9 chip connected with SMA and experimental setup to measure P_{\min} .

The measured wake-up power of the Higgs-9 chip is approximately constant over the frequency band and is equal to, $P_{\min} = -9.2$ dBm for the chosen working frequency of 928 MHz. This power is used as the input power for the impedance analyser, and the measured chip impedance of the two Higgs-9 chips is presented in Figure 2.9. The measured real and imaginary parts of the two samples of Higgs-9 chips are in good agreement which shows the data integrity and reliability of the chip.

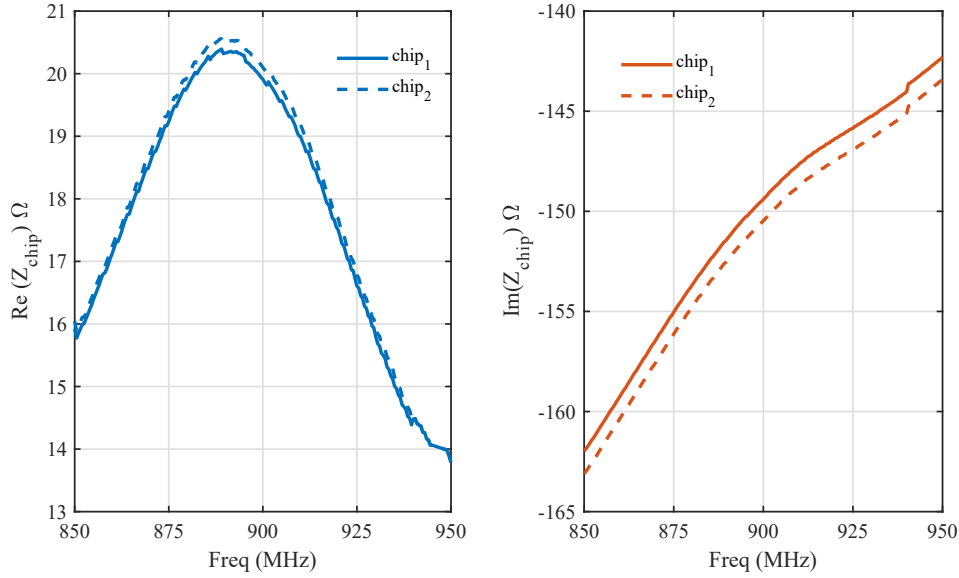


Figure 2.9: Measured real and imaginary parts of the impedance of two samples of Higgs-9 chips using the impedance analyser.

The measured chip impedances of two samples of Higgs-9 are coherent from one chip to another over the frequency band and for a given turn-on power. Now, we can estimate the chip sensitivity (P_{th}) over the frequency band. Using equation 2.2, the sensitivity of the Higgs-9 chip is shown in Figure 2.10 (a). It would be interesting to observe the mismatch between Z_{chip} and Z_0 in terms of reflection coefficient (in dB) which is also traced in 2.7 (b) using equation 2.1.

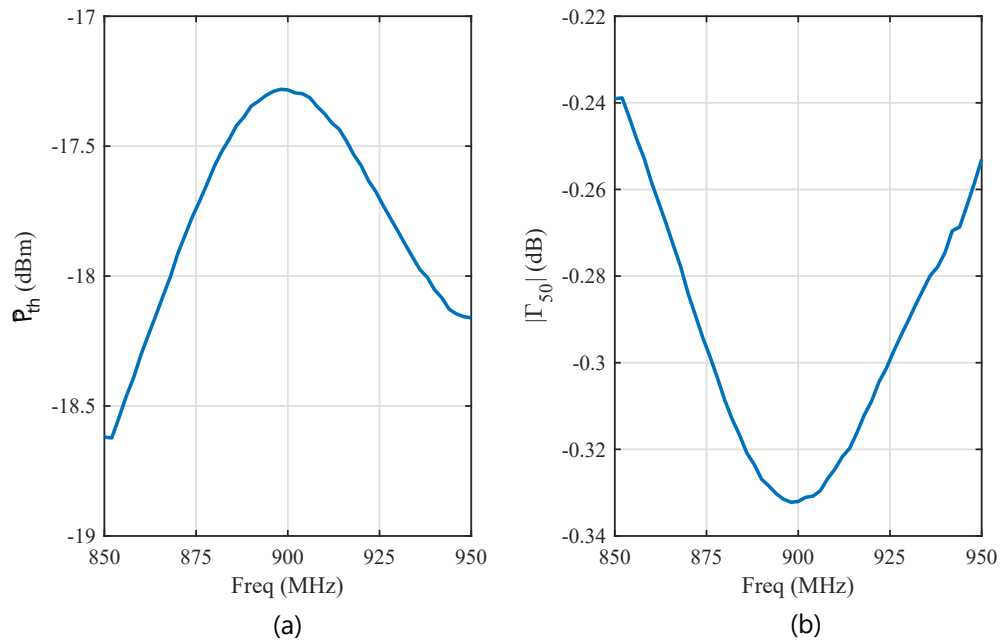


Figure 2.10: Power absorbed, P_{th} by the chip in dBm (a) and Γ_{50} of the Higgs-9 chip (b).

2.2 Characterisation of the RFID tags and the chip

According to Figure 2.10(a), the chip sensitivity P_{th} of the Higgs-9 chip is -17.85 dBm for a chosen working frequency of 928 MHz. In the datasheet, the given bare die read sensitivity of the Higgs-9 chip is -17.7 dBm over the frequency band. The chosen power sensitivity (P_{th}) is -18.2 dBm at the most matching frequency of 862 MHz for a home-made tag. After characterising the Higgs-3 and Higgs-9 chips, the next step is to characterise the tag antenna associated with these chips.

The ALN-9662 tag is built around the Higgs-3 chip and as mentioned, there is no reference tag associated with the Higgs-9 chip, so with the help of my fellow Ph.D. student and our team, we designed a capacitively loaded meandered dipole antenna which should be conjugately matched to the Higgs-9 chip. A schematic of the designed tag antenna with its dimensions is shown in Figure 2.11. The design of this tag antenna is based on that of ALN-9662, etched on a plastic substrate. The home-made tag has been realised on an FR4 substrate. The properties of the substrate have been adjusted through reverse simulations with respect to the measurements.

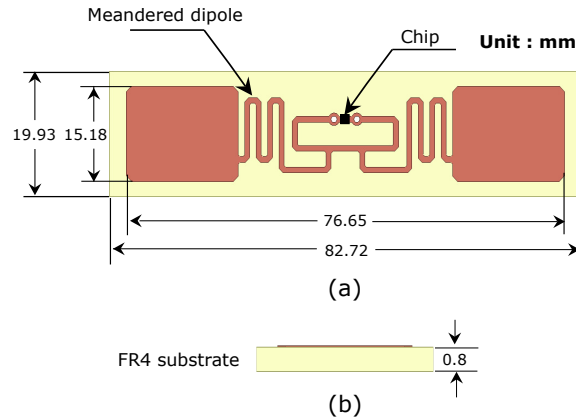


Figure 2.11: Schematic of the home-made RFID tag with its dimensions (top view in (a) and side view in (b)).

The characterisation of the ALN-9662 tag and a home-made tag without their associated chips have been carried out using the experimental setup explained in section 2.1.2. The complex input impedance (Z_a) of the tag antenna is measured with a VNA using a differential excitation technique explained in [18]. A differential excitation consists of feeding the antenna using two coaxial cables constituting the two input ports of the antenna. The antenna input impedance as a function of the S parameters is obtained by using the current-voltage equations related to the impedance matrix of the two cables using VNA [34]. After following the methodology explained in section 2.1.2, we obtain the differential S parameter matrix of the tag antenna. Then from the differential S matrix we obtain the S11 which is then used to calculate the antenna input impedance as shown in Figure 2.12.

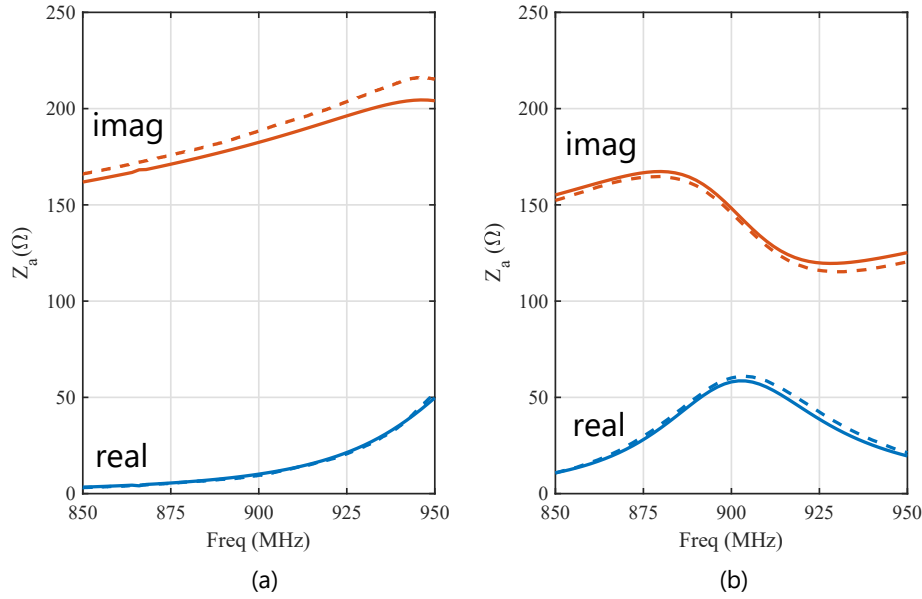


Figure 2.12: Measured (dotted line) and simulated (solid line) impedance of ALN-9662 tag (a) and home-made tag (b) over the frequency band.

The results of tag antennas without their associated chips indicate that the simulated input impedance of both tag antennas matches well with the measured impedance over a range of frequencies. Previously, it was observed that the measured impedance for Higgs-3 was found to be unreliable for practical use. Consequently, we opted to present the simulated chip impedance of Higgs-3 in order to assess its matching condition with the ALN-9662 tag, as shown in Figure 2.13. The value given in the datasheet has a resistance in parallel with capacitance to have a chip impedance. This approach differs from that of measured Higgs-9, which exhibits conjugate matching with a home-made tag at a frequency of 862 MHz, as illustrated in Figure 2.14.

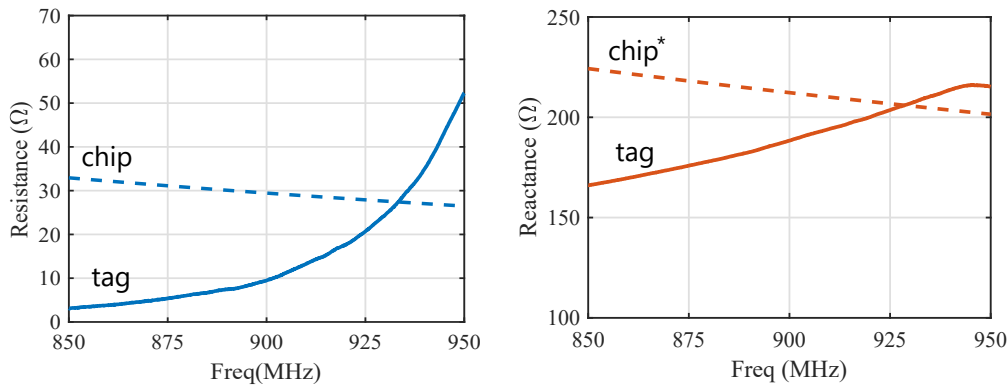


Figure 2.13: Real and imaginary parts of the commercial ALN-9662 tag (measured: solid line) and chip (simulated: dotted line).

Following the characterisation of the chip and tag separately and their respective matching condition, it would be interesting to evaluate a complete RFID tag having both antenna and chip together. Among the available possibilities of evaluating both

2.2 Characterisation of the RFID tags and the chip

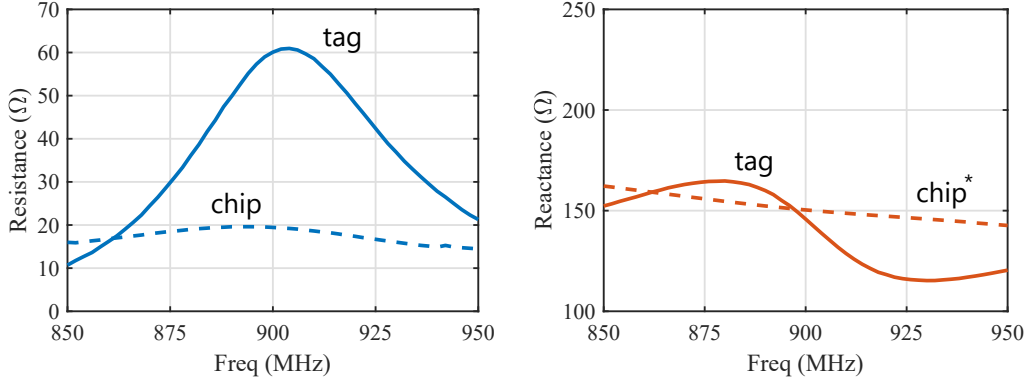


Figure 2.14: Measured real and imaginary parts of the impedance of the home-made tag (solid line) and the Higgs-9 chip (dotted line).

forward and reverse link with their respective key parameters, we would work on the forward link and read-range is the available observable to evaluate on system-level in the forward link. To achieve this, the tag antenna connected to its chip is further used to measure the read range. The experimental setup discussed in section 2.1.3 is used to characterise the tag antenna with its chip as a unified entity. The maximum reading range is related to the power absorbed by the chip (P_{th}) using the following equation [39]:

$$d_{\max} = \sqrt{\frac{P_{\text{EIRP}_{\max}} G_{\text{tag}} (1 - |\Gamma|^2) \lambda}{P_{\text{th}} 4\pi}} \quad (2.3)$$

where, $P_{\text{EIRP}_{\max}}$ is the maximum regulated effective isotropic power radiated by the reader antenna, P_{th} is the chip sensitivity, G_{tag} is the maximum gain of the tag antenna of interest, and $|\Gamma|$ is the reflection coefficient due to the mismatch between the tag antenna and the chip, expressed as:

$$|\Gamma| = \left| \frac{Z_{\text{chip}} - Z_a^*}{Z_{\text{chip}} + Z_a} \right| \quad (2.4)$$

where Z_{chip} is the chip impedance and Z_a is the impedance of the tag antenna of interest. To characterize the tag and chip together, three samples of isolated ALN-9662 tag attached with its Higgs-3 chip and home-made tag attached with its Higgs-9 chip are first measured by placing them in a Voyantic cabinet individually to directly measure their maximum read range using the Tagformance system. The second approach for estimating the maximum read range of an RFID system in meters involves simulation, utilising equation 2.3. To undertake a simulation-based approach, we define the characteristics of the RFID system as follows:

- G_{tag} is estimated by simulating ALN-9662 tag and home-made tag in HFSS over the frequency band.
- Z_{chip} is calculated from datasheet for Higgs-3 and measured for Higgs-9.

- Z_a is measured and simulated for both ALN-9662 tag and home-made tag.
- $|\Gamma|$ is obtained from measured and simulated Z_a using equation 2.4. It is also traced in Figure 2.15.
- $P_{th} = -16$ dBm for Higgs-3 (from datasheet), and -18 dBm for Higgs-9 (from measurement).
- $P_{EIRP} = 3.28$ W (from Voyantic)

The data depicted in Figure 2.15 illustrates that the ALN-9662 tag resonates at 928 MHz and home-made tag is at 862 MHz.

2.2 Characterisation of the RFID tags and the chip

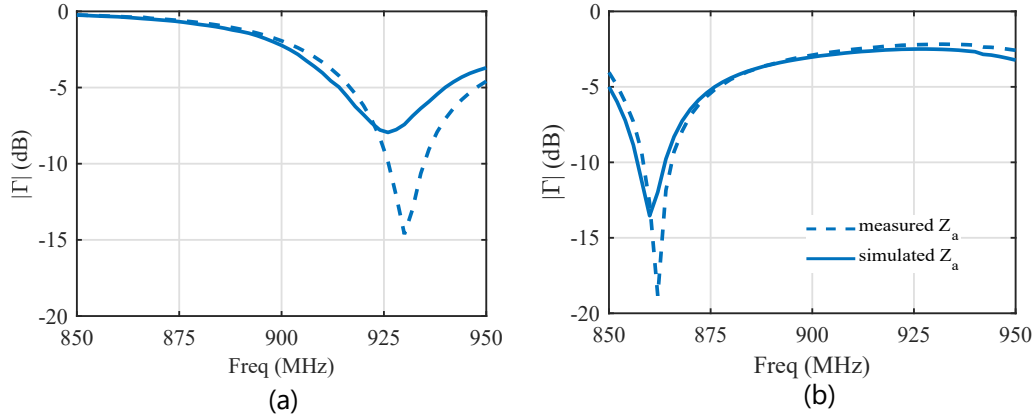


Figure 2.15: Measured and simulated reflection coefficient in dB of ALN-9662 tag (a) and home-made tag (b).

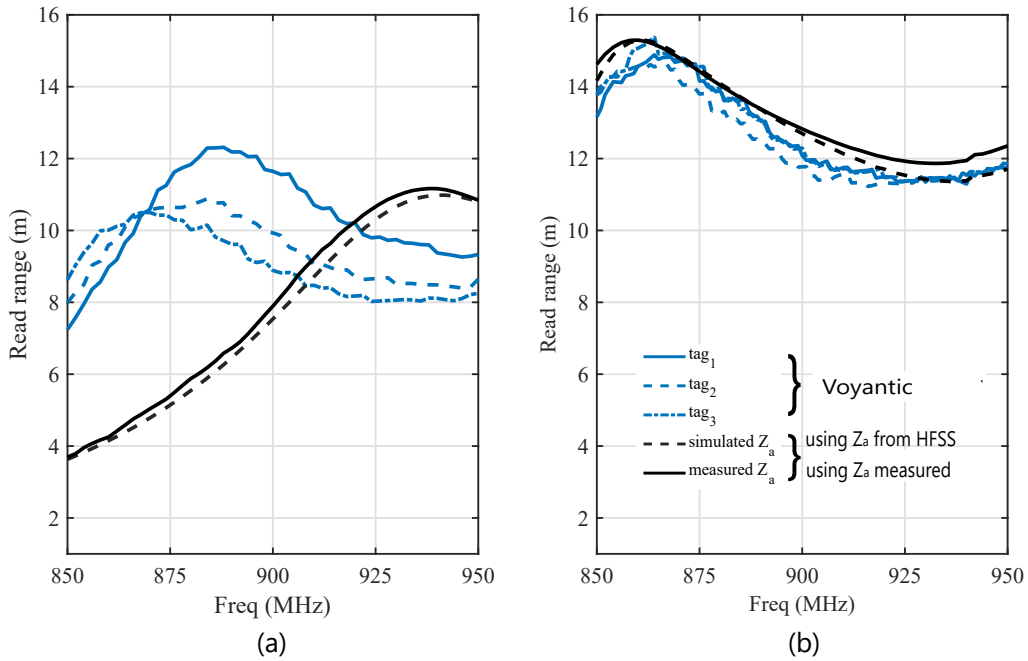


Figure 2.16: Measured and simulated read range (m) of three samples of ALN-9662 (a) and home-made tag (b).

According to Figure 2.16, the maximum read range of home-made tag is observed as approximately 15 meters while in the commercial tags, the inconsistency is observed in the measured read range evolution of the ALN-9662 tags across the frequency band. This is attributed to the discrepancies seen in the characterisation of chip impedance among different chips. In contrast, for homemade tags, the read range remains consistent from one tag to another. In a simulation, two read range curves are presented: one represents the read range using the measured antenna impedance (black dotted line), while the other depicts the read range based on the simulated antenna impedance (black solid line). The measured read range for all three samples of our homemade

tags closely matched the simulated read range. However, this consistency did not hold for the commercial tag, as it exhibited significant unpredictability in the measurement of chip impedance.

After comprehensively characterising the RFID tag across various parameters, our focus now shifts to advancing our work, primarily centred on the random deployment of tags within a designated area. Given the observed issue of non-repeatability in Higgs-3 impedance for the ALN-9662 tags, we will proceed with our work using the chip impedance calculated from the datasheet, which is in a matching condition with the ALN-9662 tag antenna.

2.3 Dipole-based RFID system

Our study primarily focuses on the impact of multiple stacked tags in a reduced volume in free space. To investigate this phenomenon, we present an RFID system in which the RFID tags, are distributed in a specified surface area in an arbitrary manner without any predetermined pattern or arrangement as shown in Figure 2.17(a). It consists of a random distribution of commercial tags over a specified area in one plane. As an initial step to fully analyse all the possible aspects of both RFID links, we developed a model in 2-D for the sake of simplicity. Also, there are practical applications such as tracking items on a conveyor belt in factories or retail outlets, where RFID tags can be attached to items moving on a surface. In such cases, the tagged items could be considered to be distributed uniformly or randomly on a plane, which is analysed in the scope of this study. In Figure 2.17(a), a reader is positioned at a point in space and is used to illuminate the tags. Each of the tags is composed of its antenna loaded with its complex chip impedance. The tag centres are assumed to be distributed randomly over the specified area and each tag is randomly oriented following the condition that they do not overlap to avoid complexities.

Within the context of this study, we aim to analyze the key parameters to assess the quality of the forward and reverse link taking into account, the polarisation of the plane wave, the random position, and orientation of the tags, the density of the tags and the effect of mutual coupling due to the polarisation of plane wave and tag's randomness. In order to reduce the complexity of the scenario shown in Figure 2.17(a), a simplified model is presented in Figure 2.17(b). The reader illuminating the set of randomly distributed tags is replaced by an incident plane wave which can be linearly or circularly polarised and the tags are replaced by two other antennas, dipole and T-match dipoles. The main reason for simplifying the model presented in Figure 2.17(a) is to address the challenges posed by the complex structure of the RFID tags and

2.3 Dipole-based RFID system

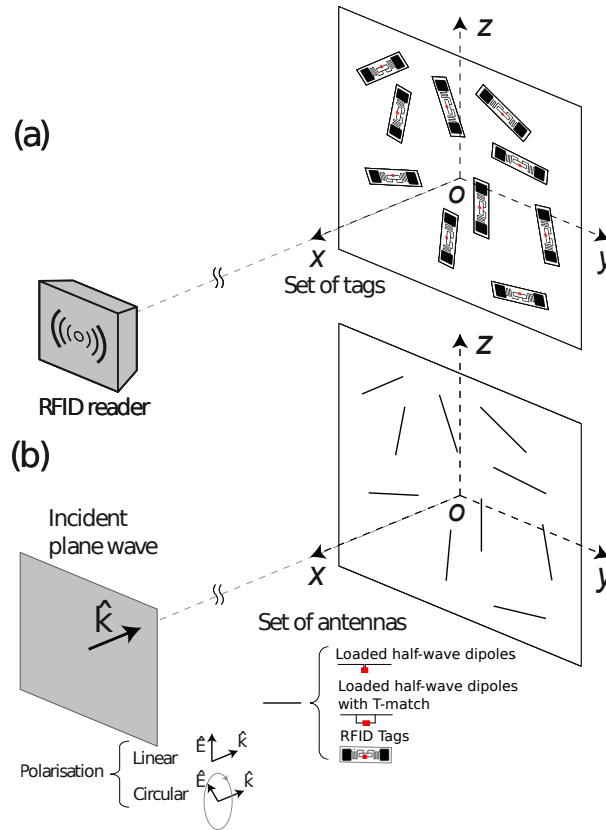


Figure 2.17: (a) RFID tags and reader modeled by (b) loaded dipoles illuminated by a linearly or circularly polarised plane wave.

the diversity of scenarios in which they are used. Analyzing such a complex system in the initial stages can be difficult and time-consuming. Therefore, it is preferable to proceed with a simplified approach using basic antennas. Among the available options, dipoles prove to be a suitable candidate for representing RFID tags due to their simplicity and effectiveness. Moreover, it is observed in [31], that the radiation pattern of an isolated tag antenna is similar to that of an isolated half-wave dipole. Also, the statistical similarities between RFID tags and half-wave dipoles in terms of mismatch in reflection coefficient have been illustrated in [20]. Based on these observations, the simplified model seems relevant but needs to be justified during the following chapters. As, the tag antenna has to be matched with the integrated chip for the maximum power transfer, and one typical matching circuit method is the T-match network, which is a common technique employed to ensure that the input impedance of a dipole-like antenna is properly matched to the input impedance of the integrated chip [40]. Consequently, a dipole antenna equipped with a T-match network seems to be a suitable replacement for creating a simplified model of an RFID system.

2.3.1 Half-wave dipole, with and without T-match network

The simplified model for a tag antenna can be based on the basic structure of a half-wave dipole. Consequently, the dipole can be designed with a matching network to be closer to the initial tag antenna topology following [40] and [41], as shown in Figure 2.18(a). A simpler equivalent model can also be adopted using a dipole without the matching network as in Figure 2.18(b).

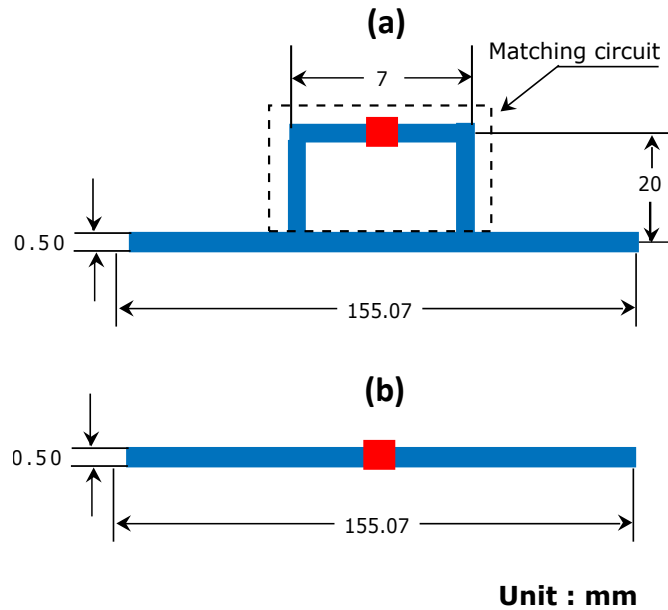


Figure 2.18: Schematic of dipole, with (a) and without Tmatch (b) network indicating its respective dimensions.

The length of the dipole and T-matched dipole is chosen to be 0.48λ at the frequency of 928 MHz, with a diameter of 0.5mm. The dimensions of the dipole were chosen to have a resonance at 928MHz taking into account the complex conjugate of the chip impedance. The T-match circuit has a length of 7mm and a spacing of 20mm. The dimensions of the T-match were chosen using the trial and error method to have an input impedance with low resistance and very high reactance, as in the case of a real commercial UHF RFID tag taking into account the complex conjugate of the chip impedance. The structure of the dipole with T-match is based on the insertion of a second folded dipole connected to the centre of the first dipole. The two simpler wire antennas allow the use of NEC solver, [35]. Due to the simpler geometry, all the required parameters of a dipole with and without T-match have been simulated by 4NEC2 and compared to HFSS in the rest of the thesis.

2.3.2 Impedance of a tag compared with dipole, with and without T-match

The input impedance of an isolated tag antenna and the complex conjugate of the impedance of the chip (Higgs-3) over the frequency band, which was obtained through simulation, is presented in Figure 2.19 in black and grey solid curve respectively. The figure indicates that the tag antenna and the chip are closely matched at 928 MHz as per the simulations performed. In an isolated case, the ideal matching condition is achieved between the impedances of the tag antenna and the chip to optimize the power transfer. The input impedance that was calculated for an isolated case of the tag antenna is $23.6 + j197.9 \Omega$, which is a quasi-complex conjugate of the impedance of the chip, i.e. $26.66 - j198.2 \Omega$, at the frequency of 928 MHz.

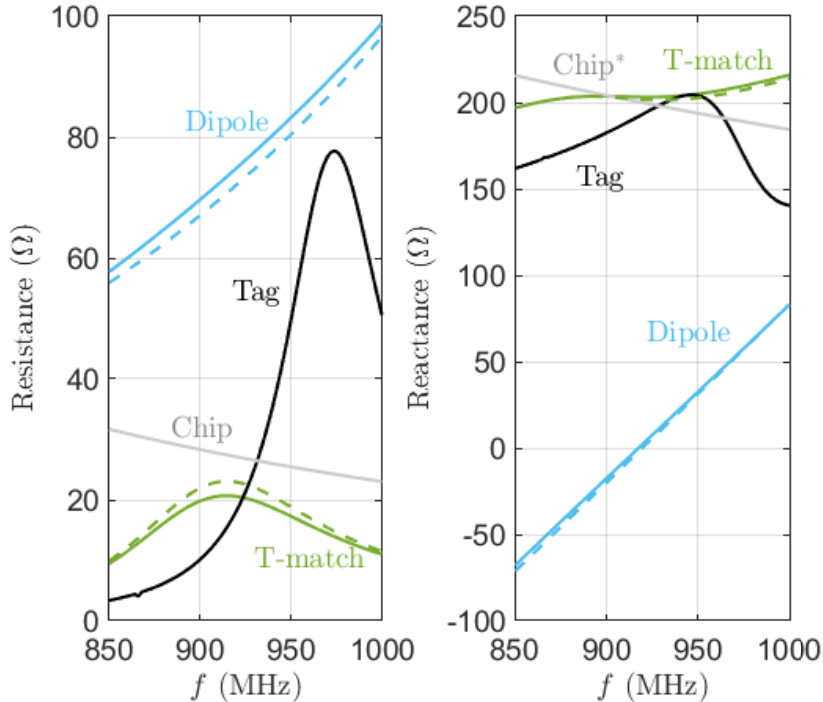


Figure 2.19: Real and imaginary parts of the impedance of the tag and the dipole with and without T-match using HFSS (solid line) and NEC (dashed line).

The other two candidates (dipole, with and without T-match) were designed taking into account the matching condition at this frequency. The input impedances of an isolated dipole and T-matched dipole were also estimated in Figure 2.19 in blue (solid and dotted) and green (solid and dotted) curve respectively. The results were obtained from NEC and validated from HFSS. It can be inferred from the results shown in Figure 2.19 that the accuracy of estimating the input impedance of wire antennas using NEC is acceptable, making it a suitable tool for this purpose. We will show later that this is not only true for the isolated case but also for the random configurations of

highly coupled dipoles. We observe that the impedance values for the three antennas over the frequency band are different. The input impedance of three antennas at 928 MHz is shown in Table 2.1.

	Dipole	T-match	Tag
HFSS	$77.0 + j10.5 \Omega$	$20.0 + j203.2 \Omega$	$23.6 + j197.9 \Omega$
NEC	$74.2 + j8.7 \Omega$	$22.2 + j201.5 \Omega$	—

Table 2.1: Input impedance of the isolated dipole with and without T-match network and real tag at 928 MHz.

In the following sections, the idea is to show that the dipole and dipole with the T-match network would be a good candidates to model the behaviour of the tag and can be used to assess the quality of both RFID links. The study will investigate both deterministic and statistical approaches to evaluate the power received at different levels of the tag in the forward link and the backscattered field re-radiated from the tags in the reverse link. All three types of antennas mentioned above will be employed in this investigation.

2.4 Conclusion

In this chapter, we have outlined a simple and practical methodology for measuring the sensitivity and impedance of RFID chips and provided experimental results for two RFID chips (Higgs-3 and Higgs-9) developed by Alien Technology. These chips operate at UHF frequencies (860-960 MHz) and support the EPC global Class 1 Gen 2 protocol. Our methodology offers a straightforward and accessible way to measure the performance of RFID chips, which can be useful for a wide range of applications in the field of RFID technology. A new home-made tag is fabricated to have a matched impedance with a Higgs-9 chip. The read range of both commercial tag (ALN-9662) and home-made tag is measured along with their antenna impedance. After discussing the observed similarities, the RFID tags are modelled by a set of half-wave dipoles, with and without T-match, and the reader is replaced by a plane wave in order to obtain a low-cost model. Two electromagnetic simulators (NEC and HFSS) have been discussed in detail, which will be used later to analyze the complete link budget of RFID systems.

2.4 Conclusion

,

Chapter 3

RFID grid modelling: A comprehensive study

In the preceding chapter, we presented a comprehensive overview of a generic RFID system, which comprised a random arrangement of antennas. In the upcoming sections, we will delve into an in-depth analysis of this proposed RFID system on a circuit level. By examining the system's circuit-level attributes, we aim to gain valuable insights into its performance and operation. Therefore, this chapter deals with the modelling of a conventional network incorporated into an RFID system, including the random distribution of dipoles with and without T-match, and the real RFID tags. The goal is to analyze and comprehend the correlation between the three types of antennas. This has been done in terms of the power budget analysis of different configurations using the proposed conventional network. The impact of coupling on the position and orientation of antennas under various conditions such as the density of the antennas, polarisation of the incident wave and the angle of incidence has also been studied. The related parameters of the forward and the reverse link have also been discussed explicitly in this chapter.

3.1 Network representation of an RFID grid

To analyze the RFID grid on a circuit level, a loaded N-port network model can be used. An electromagnetic field illuminates a set of loaded scatterers that can be modelled using an equivalent circuit model shown in Figure 3.1(a). As described in [16] and [14], the induced open-circuit voltages caused by the electromagnetic field can be represented by a vector $[\mathbf{V}_{OC}]$. The open-circuit voltages can also be used as a substitute source of excitation for the incident plane wave because they can provide equivalent information about the behaviour of the electromagnetic field as they can simplify the analysis and computation of the electromagnetic field. The terminating load impedances, which make up the "load network", are represented by another vector

3.1 Network representation of an RFID grid

$[\mathbf{Z}_L]$. The coupling effects are taken into account by an $N \times N$ impedance matrix $[\mathbf{Z}]$, which represents the "scatterer network". The input current and voltage at the n^{th} port are denoted by I_n and V_n , respectively.

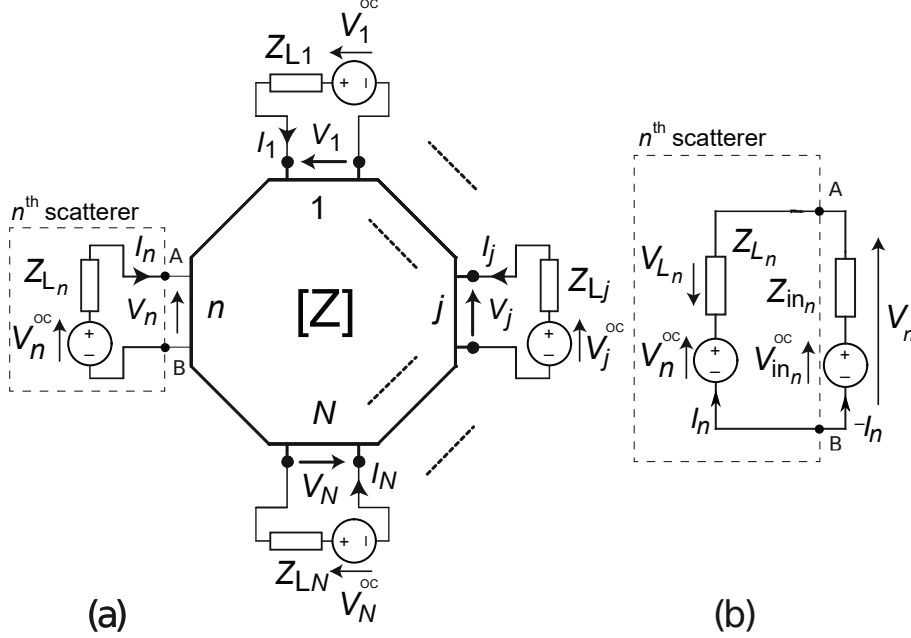


Figure 3.1: Equivalent circuit model of (a) N loaded tag antennas exposed to an incident electromagnetic wave (b) the circuit as seen by the n^{th} tag antenna.

The circuit between A and B nodes, seen by the n^{th} tag, can be replaced by a Thevenin equivalent model shown in Figure 3.1(b), to investigate both RFID links. The Thevenin equivalent circuit is composed of an overall open-circuit voltage $V_{\text{in}_n}^{\text{oc}}$ which accounts for all the voltage sources V^{oc} , on the remaining $N - 1$ ports due to the illumination of an electromagnetic field on the set of loaded scatterers. The input impedance Z_{in_n} of the overall network as seen by the n^{th} driven tag, which includes all the couplings are also included in 3.1(b). Two power values can be calculated at the level of the two voltage sources : $P_{V_n^{\text{oc}}}$ is the power induced at the level of the n^{th} tag when it is exposed to an incident electromagnetic field. $P_{V_{\text{in}_n}^{\text{oc}}}$ is the power induced by the other $N - 1$ tags seen by the n^{th} tag including all coupling effects. They can be estimated as,

$$P_{V_n^{\text{oc}}} = \frac{1}{2} \Re \left(V_n^{\text{oc}} I_n^* \right) \quad (3.1)$$

and

$$P_{V_{\text{in}_n}^{\text{oc}}} = \frac{1}{2} \Re \left(V_{\text{in}_n}^{\text{oc}} - I_n^* \right) \quad (3.2)$$

The equivalent network model of Figure 3.1 (b) offers the possibility to draw up the power budget of the network. The algebraic sum of these two powers ($P_{V_n^{\text{oc}}}$ and $P_{V_{\text{in}_n}^{\text{oc}}}$),

is divided between the power absorbed by the load (Z_{L_n}) to turn on the integrated chip of n^{th} tag and the power received by the tag's antenna (Z_{in_n}) in order to communicate back with the reader i.e. $P_{V_n^{\text{OC}}} + P_{V_{\text{in}_n}^{\text{OC}}} = P_{L_n} + P_{\text{in}_n}$. The behaviour of the two voltage sources is determined by the sign convention of the port current I_n . One of these sources must act as a generator, supplying power to the circuit, which then divides between the antenna and the load levels of the tag. Let's consider the power induced by a plane wave, denoted as $P_{V^{\text{OC}}_n}$. According to the sign convention of I_n , if $P_{V_n^{\text{OC}}}$ is positive, the voltage source operates as a power generator within the circuit. Conversely, if it's negative, the source functions as a power receiver within the circuit. Similarly, the power induced by coupling due to the presence of $N - 1$ active ports is expressed as $P_{V^{\text{OC}}_{\text{in}_n}}$. According to the sign convention of I_n , a positive value for $P_{V^{\text{OC}}_{\text{in}_n}}$ indicates constructive coupling, making the source act as a generator supplying power to the circuit. Conversely, a negative value means the voltage source operates as a receiver, providing power to the other tags. It's crucial to note that both voltage sources cannot be negative simultaneously because the circuit requires at least one generator to function. For the forward link analysis, the voltage across the load of the n^{th} driven tag can be computed using the voltage divider theorem as,

$$V_{L_n} = \frac{Z_{L_n}}{Z_{\text{in}_n} + Z_{L_n}} (V_n^{\text{OC}} - V_{\text{in}_n}^{\text{OC}}) \quad (3.3)$$

where, Z_{in_n} is the input impedance of n^{th} driven tag in the presence of other loaded $N - 1$ tags, and can be computed using the modified impedance matrix of the network shown in Figure 3.1(a) using the following equation illustrated by [20],

$$Z_{\text{in}_n} = \frac{1}{\mathbf{Z}_{\text{mod}_n}^{-1}(n, n)} \quad (3.4)$$

The modified impedance matrix $\mathbf{Z}_{\text{mod}_n}$ is obtained by adding the tag's load impedance over the corresponding diagonal elements of the impedance matrix \mathbf{Z} except for Z_{nn} ,

$$\mathbf{Z}_{\text{mod}_n} = \begin{bmatrix} Z_{11}+Z_{L_1} & \cdots & Z_{1i} & \cdots & Z_{1n} & \cdots & Z_{1N} \\ \vdots & & & & & & \\ Z_{j1} & \cdots & Z_{jj}+Z_{L_j} & \cdots & Z_{jn} & \cdots & Z_{jN} \\ \vdots & & & & & & \\ Z_{n1} & \cdots & Z_{ni} & \cdots & Z_{nn} & \cdots & Z_{nN} \\ \vdots & & & & & & \\ Z_{N1} & \cdots & Z_{Ni} & \cdots & Z_{Nn} & \cdots & Z_{NN}+Z_{L_N} \end{bmatrix} \quad (3.5)$$

The most important parameter of the forward link is the collected (absorbed) power at the load of the n^{th} tag which will be used to turn on the tag and can be calculated as,

3.1 Network representation of an RFID grid

$$P_{L_n} = \frac{1}{2} \Re(V_{L_n} I_n^*) = \frac{1}{2} \left| \frac{V_n^{\text{OC}} - V_{\text{in}_n}^{\text{OC}}}{Z_{L_n} + Z_{\text{in}_n}} \right|^2 \Re(Z_{L_n}) \quad (3.6)$$

In this network model, all the loaded scatterers are activated simultaneously. These expressions can be given as a function of the reflection coefficient, which is defined as the mismatch between the antenna and terminated load impedances of each of the scatterers in the presence of other activated loaded antennas. For this, equation (3.6) can also be re-written as,

$$P_{L_n} = \frac{1}{2} \Re(V_{L_n} I_n^*) = \frac{1}{2} \Re(Z_{L_n} I_n I_n^*) = \frac{1}{2} |I_n|^2 \Re(Z_{L_n}) \quad (3.7)$$

and can be expressed as,

$$P_{L_n} = \frac{|V_n^{\text{OC}} - V_{\text{in}_n}^{\text{OC}}|^2}{8R_{\text{in}_n}} (1 - |\Gamma_{\text{int}_n}|^2) \quad (3.8)$$

where Γ_{int_n} is the mismatch between the load impedance (Z_{L_n}) and input impedance (Z_{in_n}) of the tag of interest in the presence of other activated loaded tags and can be expressed as,

$$\Gamma_{\text{int}_n} = \frac{Z_{L_n} - Z_{\text{in}_n}^*}{Z_{L_n} + Z_{\text{in}_n}} \quad (3.9)$$

The derivation of equation (3.8) is presented in Annex A. Furthermore, the tag will be powered up after having the collected power (P_{L_n}) greater than the minimum required power, i.e. the sensitivity of the chip in case of real tags. After the tag is powered up, the power re-radiated from the n^{th} tag antenna to the reader can be estimated. In the real case scenario, the chip impedance of the tag is asynchronously changed to achieve the backscattering modulation i.e. the responding tag switches its chip impedance between two states [42]. In a tag equivalent model (c.f Figure 3.1(b)), two different load impedance values can be considered for the n^{th} driven tag [14]. The voltage division using the Thevenin equivalent circuit is then operated with the two loads, $Z_{L_n}^{\text{High}}$ and $Z_{L_n}^{\text{Low}}$ in the reverse link and can be computed as follows,

$$V_{\text{in}_n} = \frac{Z_{\text{in}_n}}{Z_{\text{in}_n} + Z_{L_n}^{\text{High/Low}}} (V_n^{\text{OC}} - V_{\text{in}_n}^{\text{OC}}) \quad (3.10)$$

The power absorbed by the load is the portion of the total induced power that is used by the tag for its operation. The remaining power absorbed by Z_{in_n} of n^{th} tag after losses is the re-radiated power towards the reader and can be expressed as,

$$P_{\text{in}_n} = \frac{1}{2} \Re(V_{\text{in}_n} I_n^*) = \frac{1}{2} \left| \frac{V_n^{\text{OC}} - V_{\text{in}_n}^{\text{OC}}}{Z_{L_n}^{\text{High/Low}} + Z_{\text{in}_n}} \right|^2 \Re(Z_{\text{in}_n}) \quad (3.11)$$

Equation (3.11) can also be written as,

$$P_{\text{in}_n} = \frac{1}{2} \Re(V_{\text{in}_n} I_n^*) = \frac{1}{2} \Re(Z_{\text{in}_n} I_n I_n^*) = \frac{1}{2} |I_n|^2 \Re(Z_{\text{in}_n}) \quad (3.12)$$

and can be expressed in terms of the reflection coefficient, Γ_{int_n} as follows (cf. Annex A),

$$P_{\text{in}_n} = \frac{|V_n^{\text{OC}} - V_{\text{in}_n}^{\text{OC}}|^2}{8R_{\text{in}_n}} |1 - \Gamma_{\text{int}_n}|^2 \quad (3.13)$$

where Γ_{int_n} can be calculated from equation (3.9) using two impedance states: $Z_{L_n}^{\text{High/Low}}$ and $Z_{L_n}^{\text{High/Low}}$. The modulation that occurs in backscattering is due to the difference between the two re-radiated powers and is a result of the difference between the two levels of load impedance as well as the coupling between the surrounding tags. This can be analyzed as the differential radar cross section of the modulated tag explained in [42].

To estimate the power equations (3.1 - 3.13) described above, the following key parameters need to be calculated: the two voltage sources, namely the induced open-circuit voltage V_n^{OC} resulting from the illumination of a plane wave, $V_{\text{in}_n}^{\text{OC}}$ which includes the effect of all the voltage sources on the remaining $N - 1$ ports due to the incident electromagnetic field and the port current I_n of each of the tags. In NEC, the two voltage sources (V_n^{OC} and $V_{\text{in}_n}^{\text{OC}}$) can not be directly obtained and need to be calculated from the current (I_n) generated at the n^{th} port. Therefore, a set of loaded tags is illuminated by a plane wave, and a series of port currents included in the vector $[I]$ are obtained by NEC. The column of port currents is related to the open-circuit voltage column vector $[\mathbf{V}^{\text{OC}}]$ by the following matrix equation,

$$\begin{bmatrix} V_1^{\text{OC}} \\ V_2^{\text{OC}} \\ V_3^{\text{OC}} \\ \vdots \\ V_N^{\text{OC}} \end{bmatrix} = \begin{bmatrix} V_1 \\ V_2 \\ V_3 \\ \vdots \\ V_N \end{bmatrix} + \begin{bmatrix} Z_{L_1} & Z_{L_2} & Z_{L_3} & \cdots & Z_{L_N} \end{bmatrix} \begin{bmatrix} I_1 \\ I_2 \\ I_3 \\ \vdots \\ I_N \end{bmatrix} \quad (3.14)$$

where \mathbf{V} is the column vector of input voltages and Z_L is the row vector of terminated load impedance. The input voltages $[\mathbf{V}]$ between the two nodes A and B of the circuit model of N tags (as shown in Figure 3.1 (b)) are related to the port currents $[\mathbf{I}]$. This

3.1 Network representation of an RFID grid

relationship is accounted for by an impedance matrix of size $N \times N$, which considers all the mutual couplings among the tags and the relationship can be expressed as,

$$[V] = [Z][I] \quad (3.15)$$

where, $[Z]$ is estimated using two-port network theory in [40] having the effect of mutual couplings. The second voltage source shown in the Thevenin model of Figure 3.1 (b), is $V_{in_n}^{OC}$, which can be computed in the presence of other loaded tags using the following formula,

$$[V_{in}^{OC}] = [V] - [I][Z_{in}] \quad (3.16)$$

where $[Z_{in}]$ is the row vector of input impedances in the presence of loaded tags. Using the above explained equations (3.1) - (3.13), one can determine the power of interest of N tags.

However in HFSS, the power of interest can be computed directly using the corresponding values of the voltages and impedances. For example, the induced power at the level of n^{th} tag when it is exposed to an incident electromagnetic field, i.e. $P_{V_n^{OC}}$ can be computed as,

$$P_{V_n^{OC}} = \frac{1}{2} \Re \left(V_n^{OC} \left(\frac{V_n^{OC}}{Z_{L_n}} \right)^* \right) \quad (3.17)$$

where, Z_{L_n} is the load impedance and the open-circuit voltage V_n^{OC} across the tag can be calculated directly as a post-processing step after the electromagnetic simulation. To obtain this value, the tag of interest is loaded with an open circuit load and all the other tags are with the matched load. Thereafter, the field calculator in HFSS can be utilized to calculate the voltage drop at the port between two endpoint locations on a line. This is accomplished by integrating the electric field along the line using the following formula:

$$V_n^{OC} = \int_l \vec{E}_n \cdot d\vec{l} \quad (3.18)$$

where \vec{E}_n represents the electric field vector, and $d\vec{l}$ denotes the differential length along the line (l). By performing the integration of the dot product between the electric field and the differential length, the voltage source at the desired port can be computed for an unloaded antenna. Similarly, the other voltage values (V_L) can be calculated using the same method explained by the equation (3.18), keeping the antenna terminated with the load impedance. The remaining two voltage values V_{in}^{OC} and V_{in} are calculated using equations (3.16) and (3.10) (by Z_L^{High} and Z_L^{Low}) respectively.

The powers at different circuit levels Figure 3.1 (b) can thus be calculated using the corresponding methodology in NEC and HFSS. The next phase involves utilizing these power equations to analyze the power budget in an RFID scenario. This analysis will be carried out using three types of antennas: dipoles, dipoles with T-match, and real tags. It enables us to determine how power is distributed across the system components of each of the antennas, taking into account the position and orientation of the antennas and coupling versus the polarisation of the incident wave.

3.2 Power Budget analysis

To accurately forecast the quality of both RFID links, it is essential to examine the power distribution at the load level and the antenna level of the driven tag as a part of the power budget analysis. The amount of power at various levels of the driven element is a function of both its tilt with regard to the incident wave polarisation (linear or circular) and the coupling with the surrounding tags. It would be interesting to refer to the power at various circuit levels of an isolated tag, supposing that it would represent a reference communication scenario from the reader to the tag, in the absence of any coupling effects. The following subsections present the power budget analysis of three different types of antennas for some deterministic configurations.

3.2.1 Isolated case

An isolated half-wave dipole, a T-matched dipole, and an RFID tag are placed symmetrically about the origin along the z -axis as shown in Figure 3.2. The dimensions of chosen antennas are already discussed earlier in Chapter 2. The results for the half-wave dipole, both with and without T-match, are simulated using 4NEC2 software and validated with HFSS. The parameters to assign a plane wave in NEC and HFSS software are detailed in Annex B and C. In NEC, the power levels at various circuit stages of the dipoles (with and without T-match) can be obtained either directly or by calculating open-circuit voltage as explained in section 3.1. The second approach involves two steps, first a plane wave is used to obtain the open-circuit voltage across the dipole while keeping the dipole unloaded. Secondly, the loaded dipole is stimulated by its respective open-circuit voltage V^{OC} . Calculations are performed to determine the power levels at both voltage sources (V^{OC} and $V_{\text{in}}^{\text{OC}}$) and at the load and antenna level (Z_L and Z_{in}). Based on the input impedances of three antennas shown in Table 2.1, each of the antennas is terminated with its respective matched load for maximum power transfer. Linear and circular polarisations of a plane wave ($E_Z = 1$ V/m) in normal incidence are used to obtain the results presented in Figure 3.3(a) and 3.3(b). The normal incidence is the most practical case to illuminate the set of tags because the reader antenna faces the tags. Therefore, a power budget analysis has been done

3.2 Power Budget analysis

for this incidence angle.

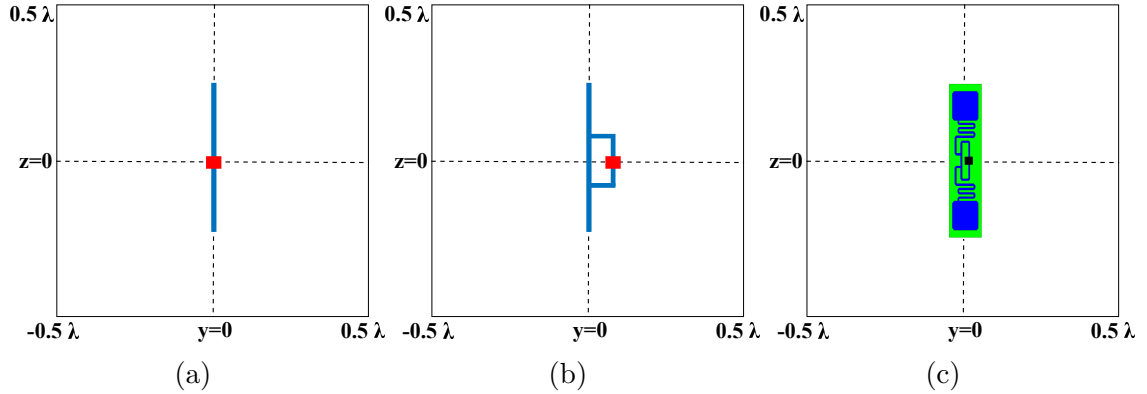
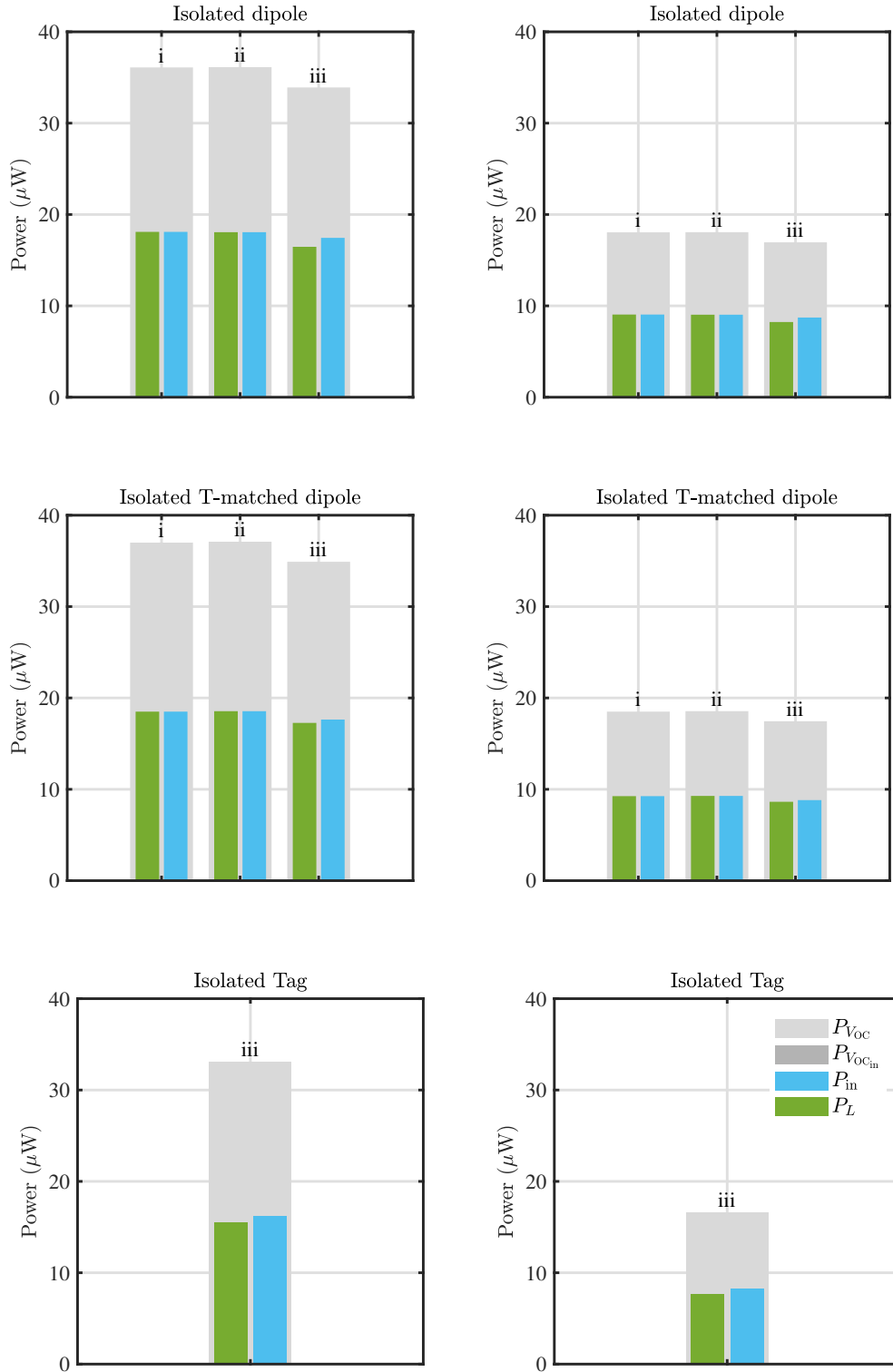


Figure 3.2: Isolated (a) dipole, (b) T-matched dipole and (c) tag, illuminated by a plane wave in normal incidence.

The power budget analysis in Figure 3.3 is presented using: (i) the plane wave directly by NEC, (ii) the equivalent V^{OC} by NEC and (iii) the plane wave directly by HFSS. Since there is a polarisation mismatch between the vertical antennas and the circularly polarised incident wave, the obtained power values for a circularly polarised incident wave are divided by $\sqrt{2}$ compared to those of a linearly polarised wave. The power levels for the dipole, with and without T-match, are similar and differ more from those of the tag. It is observed that in the absence of surrounding elements, the power induced by the coupling effects ($P_{V_{\text{in}}^{\text{OC}}}$) is null. It is worth noting that the two NEC-based models exhibit good agreement with HFSS for the case of an isolated dipole, with and without a T-match network. According to NEC, the voltage induced by the plane wave and the associated power at the voltage source $P_{V_{\text{OC}}}$, is equally divided between the load and the antenna impedance as the isolated dipole is matched. In the case of HFSS, the powers are slightly unequally divided between the load and the antenna which is due to the difference in meshing in every simulation. Each simulation has a different meshing in HFSS. However, the power at various levels obtained from HFSS is always slightly less than the ones obtained from NEC. This is due to the difference in impedance values of the antenna obtained from NEC and HFSS.

This suggests that the circuit model is validated for both polarisations of a plane wave. For a simulation setup, these power values in an isolated case could be considered a good reference to evaluate the effect of coupling in a high density context.



(a) Linear Polarisation

(b) Circular Polarisation

Figure 3.3: Power levels of the isolated antennas employing the linearly polarised plane wave in (a) and circularly polarised plane wave in (b) under three numerical techniques: i. direct plane wave excitation in NEC, ii. open circuit voltage V^{OC} from NEC, iii. direct plane wave in HFSS. P_{VOC} : Induced power on the antenna, $P_{VOC_{in}}$: Induced power by other antennas, P_{in} : Re-radiated power by the antenna, P_L : Absorbed power by the load.

3.2 Power Budget analysis

In a real case scenario, P_L represent the power absorbed by the load (chip), which should be greater than the sensitivity of the chip to turn on the tag and P_{in} is the re-radiated power that goes to the antenna, to communicate back with the reader. However, here in this simulation, the absorbed power is calculated with an incidence of a plane wave of $E_z = 1$ V/m and is considered to be the reference value in order to quantify the degradation brought by the impacting factors. Here, P_L is approximately equal to $19\mu\text{W}$ (-17.4 dBm) for both dipoles and T-match dipoles, and $15\mu\text{W}$ (-18.1 dBm) for the tag in the case of linear polarisation. In the case of circular polarisation, the absorbed power is approximately $9\mu\text{W}$ (-20.4 dBm) for dipoles and T-match dipoles, and $7.7\mu\text{W}$ (-20.1 dBm) for the tag. We intend to quantify the degradation of the various power levels in terms of the position and orientation of antennas and the mutual coupling in the presence of other antennas, compared to the isolated case. To predict the behaviour of antennas in various configurations requires significant computer resources and would be time-consuming in the case of HFSS, therefore, we use only 4NEC2 to analyze the impact of the orientation of dipoles/T-match dipoles versus the polarisation of the plane wave as well as the mutual coupling between them in the following sections.

3.2.2 A set of two parallel antennas

Consider a set of two linearly polarised parallel antennas (dipoles, with and without T-match and real tags), loaded with their respective isolated matched load placed along the yo z plane. They are spaced at a distance of d as shown in Figure 3.4. Each set of antennas is illuminated by a linearly polarised plane wave in a normal incidence. We intend to analyze the change in the amount of power received at various circuit levels of each element in the presence of another antenna, which introduced mutual coupling between them. This change is also analyzed in terms of spacing between antennas because the closer the antennas, the more will be the coupling. Therefore, three distances of $d_1 = 0.1\lambda$, $d_2 = 0.2\lambda$, and $d_3 = 0.3\lambda$ were chosen at a frequency of 928 MHz.

The power budget analysis, presented in μW , illustrates the characteristics of three different types of antennas, as shown in Figure 3.5. In this particular scenario, two parallel antennas are arranged in each group. These antennas are identical and equipped with matched loads, ensuring that they receive an equal amount of power from a linearly polarised plane wave. However, due to mutual coupling introduced by the presence of the other dipole/tag, the absorbed power (P_L) and re-radiated power (P_{in}) within each set are distributed unevenly between the load and antenna levels. The observed trend is that mutual coupling decreases as the spacing between two antennas increases. Consequently, less power is absorbed by the load, and more power is transferred to the antenna level in each set of two parallel antennas. However, the

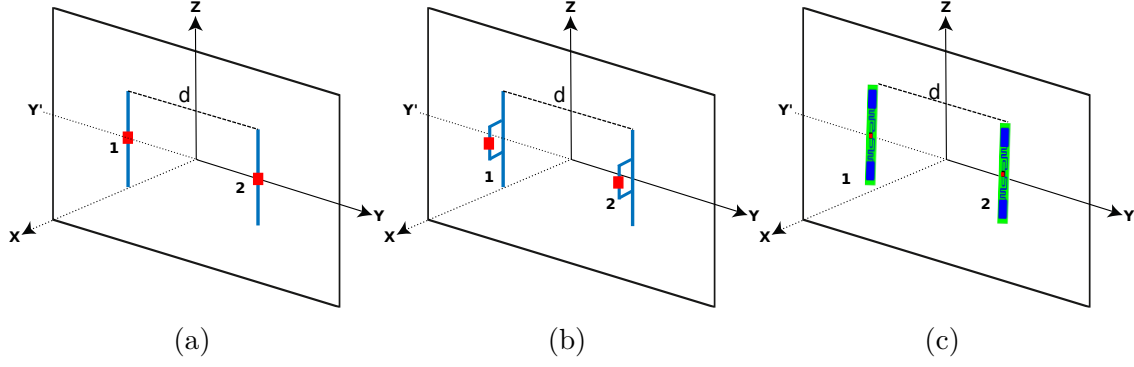


Figure 3.4: A set of two parallel dipoles (a), T-matched dipoles (b), and tags (c), placed at a distance d from each other and illuminated by a plane wave in a normal incidence.

distribution of powers at the load level of dipoles does not exhibit similar behaviour with those of T-matched dipoles and tags. A slight difference can be observed in the power division at the two voltage sources of two parallel tags, which is attributed to the variation in meshing during the HFSS simulation. However, no definitive conclusion could be made for a set of two parallel antennas. For instance, Figure 3.5 (a) depicts the case of two parallel dipoles, where the coupling effect induces a negative power at the voltage sources, V_{in}^{OC} . A negative power value could indicate that one of the voltage sources is working as a receiver instead of a generator. This would be the case if the source is absorbing power from the system rather than supplying power to it. According to the direction of current flow in an equivalent circuit of Figure 3.1 (b), a positive power for V_n^{OC} is considered to be supplied while for $V_{in_n}^{OC}$ is considered to be received. Consequently, a negative power for $V_{in_n}^{OC}$ indicates that the voltage source works as a generator and this is specifically observed in the case of dipoles. On the other hand, the induced power in the other two sets of antennas has a positive value at both voltage sources, indicating that the power is flowing in the positive to negative direction. In all cases, the algebraic sum of the two powers at the two voltage sources equals the summation of power absorbed by the load and antenna levels, i.e. $P_{V_n^{OC}} + P_{V_{in_n}^{OC}} = P_{L_n} + P_{in_n}$. The circular polarisation of the incident wave is not discussed here as it would show similar behaviour but with lesser amplitude. After incorporating the effects of coupling between antennas, it would be insightful to further investigate the impact of the orientation of antennas in a deterministic scenario before proceeding to the evaluation of the forward link in terms of absorbed power. At present, we have opted to use dipoles exclusively to streamline the process and expedite the evaluation of the network model using an alternative approach.

3.2 Power Budget analysis

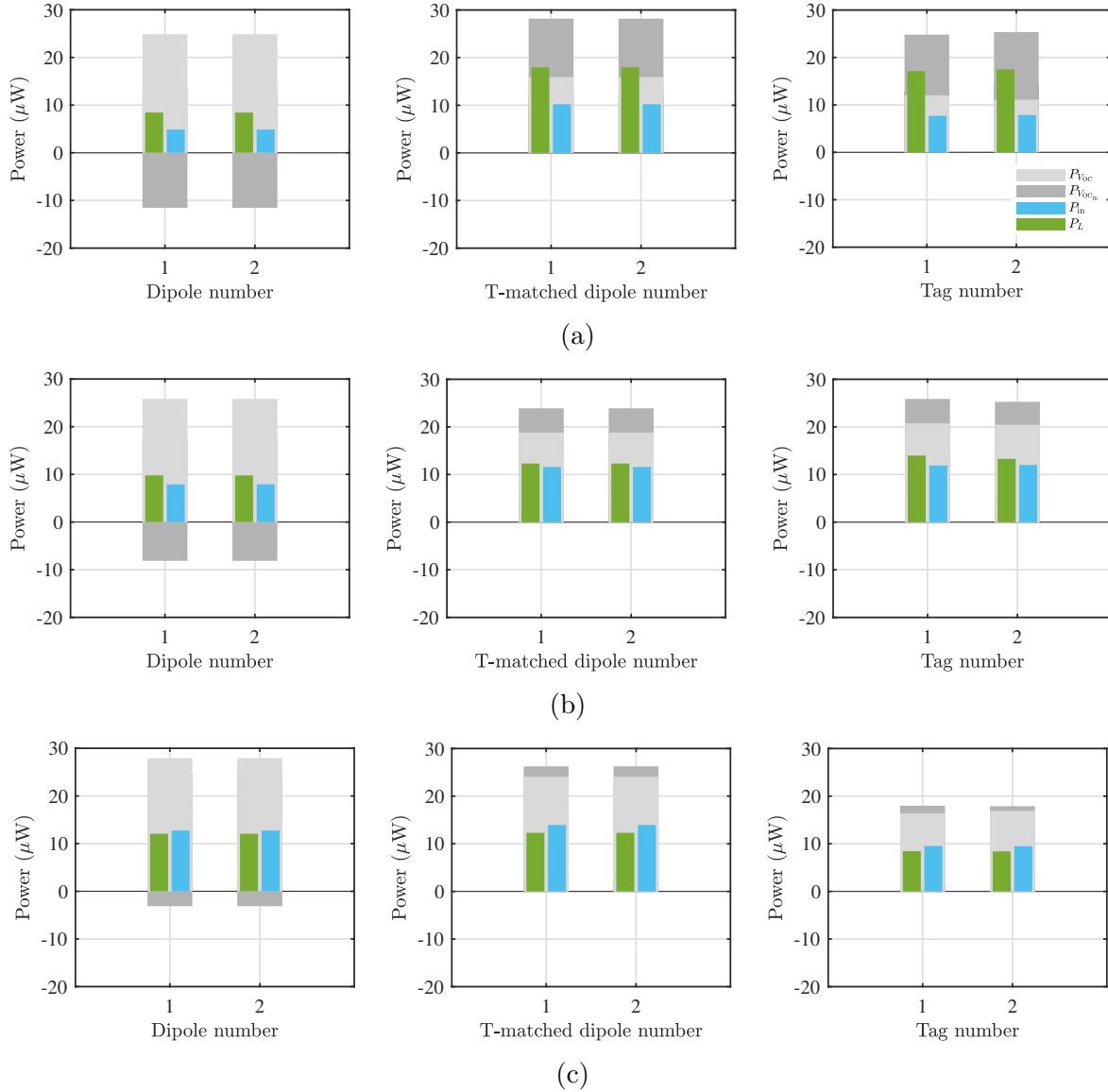


Figure 3.5: Power levels of two parallel dipoles, T-matched dipoles and tags, spaced at a distance of (a) 0.1λ , (b) 0.2λ and (c) 0.3λ . P_{VOC} : Induced power on the antenna, $P_{VOC_{in}}$: Induced power by other antennas, P_{in} : Re-radiated power by the antenna, P_L : Absorbed power by the load.

To add more complexity to this scenario considering coupled tags, we aim to analyze the contribution of randomness in terms of position, orientation, and density of antennas in a given surface area with the polarisation of the incident field, with or without the effect of mutual coupling between them. To achieve this, a set of simulations has been performed for the arbitrarily distributed antennas which will be discussed next in this section.

3.2.3 Array of ten randomly distributed antennas

To quantify the power budget in a configuration presenting a higher complexity, a set of ten antennas is considered. In order to be time efficient, only a set of dipoles is simulated in 4NEC2. Let us consider an area of dimensions $1\lambda \times 1\lambda$ in yoz plane where ten identical half-wave matched dipoles are distributed randomly, as shown in Figure 3.6. Each dipole has random centre coordinates and orientation following the condition that they do not overlap. The set of dipoles is illuminated by a linearly and circularly polarised plane wave in a normal incidence.

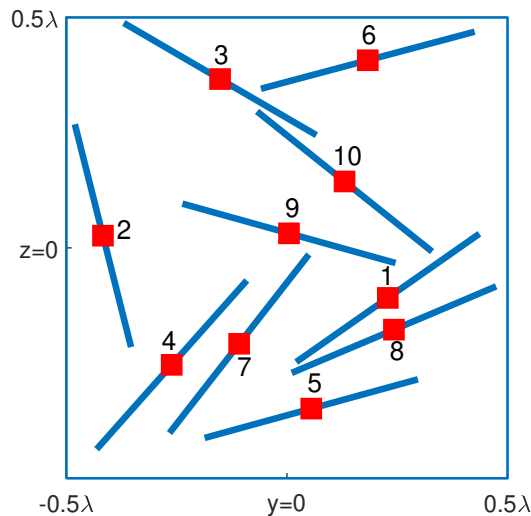


Figure 3.6: Ten loaded half-wave dipoles randomly distributed over a surface of dimensions $1\lambda \times 1\lambda$.

The open-circuit voltage (V_n^{OC}) across each loaded dipole has been calculated using 4NEC2 by considering the respective polarisation of the incident field while keeping all the other dipoles in the array simultaneously unloaded. In a second simulation, the plane wave is removed, and the dipoles are driven by their respective V_n^{OC} while terminated on their matched load. Consequently, the different electrical quantities in Figure 3.1(b) have been calculated. Figure 3.7 illustrates for each dipole, from 1 to 10, the power budget analysis in μW for both linearly and circularly polarised plane wave. At first, we considered each dipole in its original position and orientation, without accounting for mutual coupling, i.e. only the orientation of the dipoles was taken into account. To do this, we suppressed mutual coupling and focused solely on the behaviour of each dipole. The power budget of such a case is shown in the first row of Figure 3.7.

Without the mutual coupling and in the case of linear polarisation, we observe that the power at the source, denoted as $P_{V_n^{\text{OC}}}$, differs for each dipole depending on

3.2 Power Budget analysis

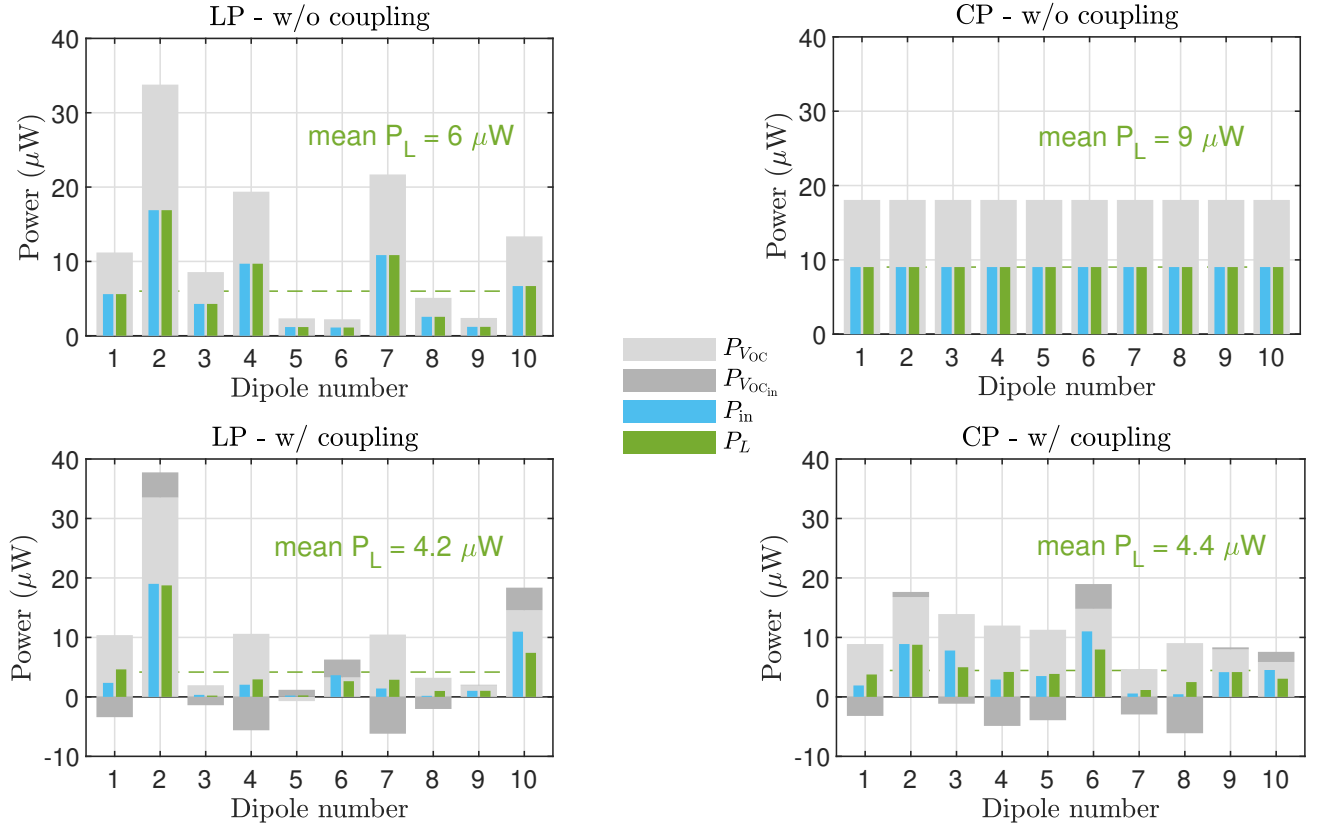


Figure 3.7: Power budget for a grid of 10 randomly distributed matched dipoles using linear (LP) and circular (CP) polarisation, with (w/) and without (w/o) mutual coupling at a polarisation angle of $\phi = 0^\circ$. $P_{V_{oc}}$: Induced power on the antenna, $P_{V_{oc_{in}}}$: Induced power by other antennas, P_{in} : Re-radiated power by the antenna, P_L : Absorbed power by the load.

its tilt. However, for circular polarisation, this power is equal regardless of the orientation. This equality is due to circular polarisation not taking the effect of orientation into account, as shown in Figure 3.3. In the absence of coupling between the dipoles, the power induced by the other dipoles, denoted as $P_{V_{oc_{in}}}$, is naturally zero for both polarisations. Moreover, the absorbed power (P_{L_n}) and the re-radiated power (P_{in_n}) are therefore identical ($P_{L_n} = P_{in_n}$) for both polarisations. However, when all ten dipoles are considered together, the power budget changes. The second row of Figure 3.7 illustrates this scenario. Due to the random positions and orientations of the dipoles, as well as the coupling between them, different power values are observed at the two voltage sources, $P_{V_{oc}}$ and $P_{V_{oc_{in}}}$, for both polarisations. All the dipoles are identical in shape but oriented differently and connected to their isolated matched loads, the power is divided unequally between them due to the mismatch caused by mutual coupling effects. As a result, the absorbed power (P_{L_n}) and the re-radiated power (P_{in_n}) are not equal in this case. On average, the absorbed power by the dipoles decreases due to the coupling effects. However, the effect of coupling on each individual dipole is a random phenomenon. For example, in the case of linear polarisation, P_{L_2} slightly

increases due to coupling, while P_{L_3} vanishes. Moreover, P_{L_2} decreases with circular polarisation, while P_{L_5} increases. Considering the direction of current flow, positive power for V_n^{OC} indicates power supply, while negative power for $V_{\text{in}_n}^{\text{OC}}$ indicates power received by the voltage source acting as a generator. From the above results, it can be concluded that the degradation of antenna performance is more significant in linear polarisation compared to circular polarisation. This is because linear polarisation takes into account both randomness and coupling effects, whereas circular polarisation only considers the coupling effect.

The powers of interest specifically in the RFID forward link and backward link would be P_L and P_{in} . Therefore, we will analyze the RFID links in the next section.

3.3 RFID forward link

As previously discussed, conducting a power budget analysis entails assessing two crucial power levels: the absorbed power P_L , primarily associated with the forward link, and the re-radiated power at the tag's antenna level denoted as P_{in} , which is vital for establishing the backward link. As the main concern of the RFID forward link is the load absorbed power, therefore, in this section we compare the three antennas only in terms of the absorbed power P_L and the degradation on the improvement could be compared to the ideal isolated case. Figure 3.8 shows the real absorbed power in μW of three different antennas when illuminated by a linearly polarised plane wave of $E_Z = 1 \text{ V/m}$, in a normal incidence. The density of ten identical antennas distributed is the same as the configuration of Figure 3.6. The associated absorbed power is obtained from 4NEC2 and HFSS and compared to those of real tags.

It is observed that the two EM simulators show an excellent agreement for dipoles, with and without T-match as shown in Figure 3.8 (a) and (b) respectively. There is a difference in amplitude in all three chosen antennas which is as expected because their intrinsic properties are different from one another. Even though the amplitude of the absorbed power may differ from one antenna type to another, it can be observed that the evolution of the absorbed power as a function of antenna number is similar for different antenna types. Hence, we can normalise the absorbed power of the dipoles, with and without T-match, and the tags distributed over a surface area, by their respective absorbed power when they are isolated, to show the correlation between them.

The normalised ($P_{L_{\text{norm}}}$) and the subsequent RMSE (Root Mean Square Error) for the absorbed power ($P_{L_{\text{norm}}}^{\text{RMSE}}$) of a dipole/tag of interest (n) using HFSS or NEC is calculated using the following formula,

3.3 RFID forward link

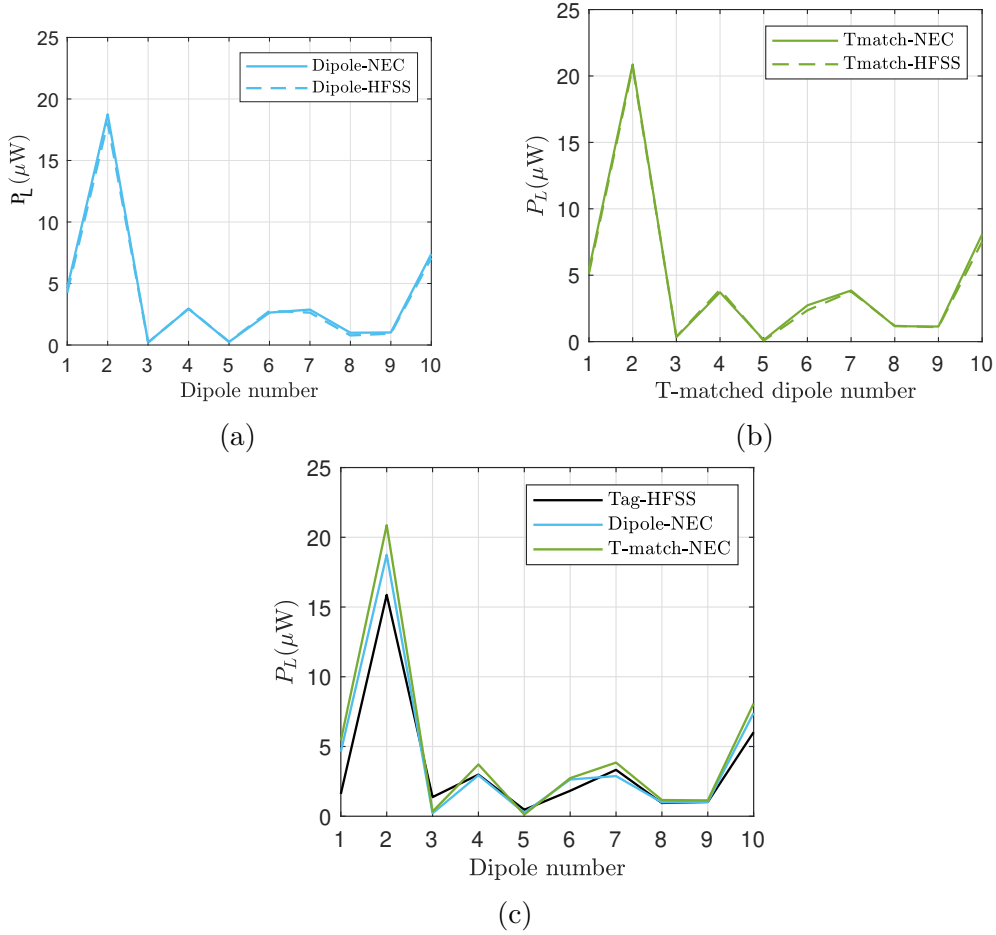


Figure 3.8: Absorbed powers (P_L) of (a) dipoles and (b) T-matched dipoles obtained by NEC and HFSS and (c) compared to those of the tags, in the random configuration shown in Figure 3.6.

$$P_{L_{\text{norm}}} = \frac{P_L}{P_L^{\text{iso}}} \quad (3.19)$$

where P_L is the real absorbed power of the dipole, with and without T-match or tag obtained from HFSS/NEC and P_L^{iso} is the real absorbed power of dipole, with and without T-match or tag in an isolated state obtained from HFSS/NEC. After having the normalised absorbed power values both from HFSS ($P_{L_{\text{norm}}}^{\text{HFSS}}$) and NEC ($P_{L_{\text{norm}}}^{\text{NEC}}$), RMSE is estimated for each of the antennas. It is a commonly used metric to measure the difference between two sets of values and it gives an indication of the overall accuracy or precision of the two sets of values. Therefore, this metric estimation is used to compare the results obtained from both NEC and HFSS simulations and to determine if the NEC simulations are accurate enough to be used instead of HFSS for a high-density context. Since NEC simulations are faster and require less computing capacity, they can be used instead of HFSS simulations for dipoles provided that their accuracy is satisfying. The RMSE of the normalised absorbed power ($P_{L_{\text{norm}}}^{\text{RMSE}}$) can be estimated as,

$$P_{L_{\text{norm}}}^{\text{RMSE}} = \sqrt{\text{mean}(P_{L_{\text{norm}}}^{\text{HFSS}} - P_{L_{\text{norm}}}^{\text{NEC}})^2} \times 100 \quad (3.20)$$

Using equations 3.19 and 3.20, the normalised absorbed power curves of dipoles/tags of the configuration shown in Figure 3.8, and the estimated RMSE results are presented in Figure 3.9. The RMSE values being small, the normalised absorbed power by 4NEC2 are validated by HFSS as mentioned in Figure 3.9 (a) and (b) for dipoles and T-match dipoles. Figure 3.9 (c) shows that although the normalised powers for the three antenna types are not identical, there is a clear correlation between the evolution of power levels of all three antenna types which can justify that the dipoles, with and without T-match, are the good candidates to replace the tags in a random scenario.

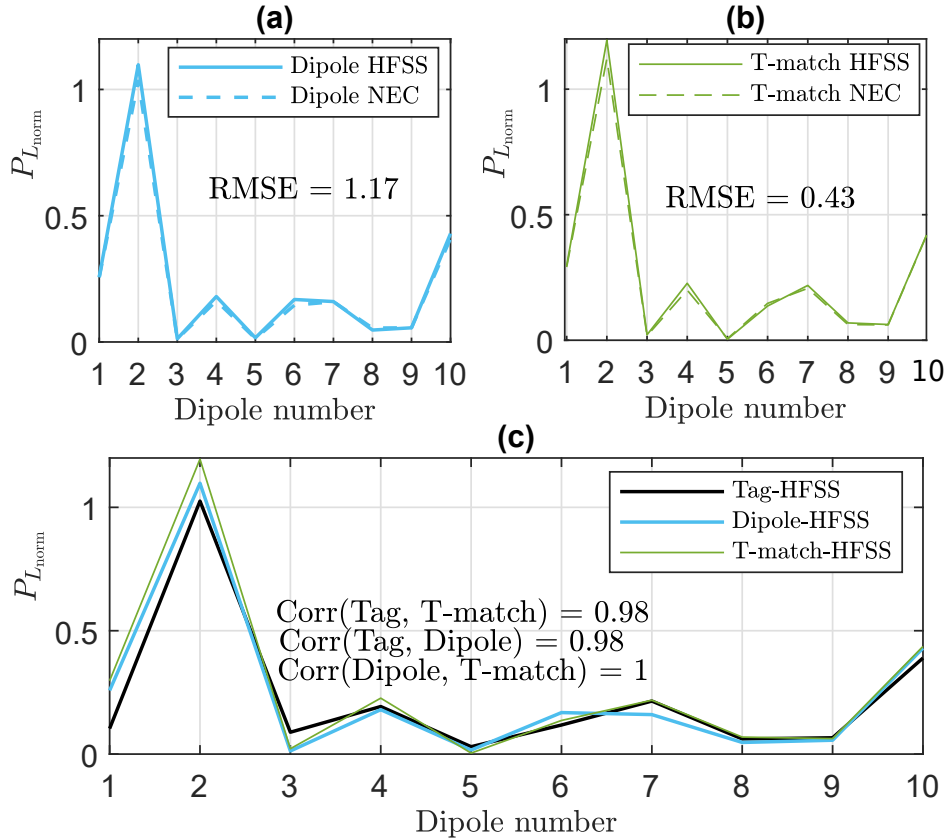


Figure 3.9: Normalized absorbed powers ($P_{L_{\text{norm}}}$) of (a) dipoles and (b) T-matched dipoles obtained by NEC and HFSS and (c) compared to those of the tags, in the random configuration shown in Fig. 3.6 with respect to their isolated P_L .

The load absorbed power can be used to estimate the percentage of the tags that got powered up with a given RF signal transmitted by the reader. This load absorbed power is a result of the free space losses between the reader and the tag as well as the mismatch between the chip (load) and the tag antenna. In a real measurement scenario with real tags connected to their chips, the power absorbed by the chip P_L is

3.3 RFID forward link

related to the reader's power and tag-to-reader distance by the following formula:

$$P_L = P_{\text{EIRP}} G_{\text{tag}} (1 - |\Gamma|^2) \left(\frac{\lambda}{4\pi d} \right)^2 \quad (3.21)$$

where $P_{\text{EIRP}} = P_t G_t$ is the isotropic power radiated by the reader antenna, P_t and G_t are the transmitted power and the gain of the transmitting antenna respectively. G_{tag} , is the gain of the tag antenna, $|\Gamma|$ is the reflection coefficient due to the mismatch between the tag antenna and chip, and d is the distance between the tag and the reader. For a practical RFID scenario, P_{EIRP} is fixed by the user with regulatory limit and the maximum reading range d_{max} is obtained for P_L equal P_{th} which is the chip sensitivity.

Here, we explain how the normalised power can be helpful to obtain the percentage of the activated tags. For an isolated tag within the system's reading range, the power absorbed by its chip is denoted as P_L^{iso} :

$$d \leq d_{\text{max}} \quad \implies \quad P_L^{\text{iso}} \geq P_{\text{th}} \quad (3.22)$$

On introducing surrounding tags, the turn-on power would be altered, positively or negatively, by coupling effects. The modified turn-on power of the tag of interest in the presence of coupling is referred to as $P_L^{\text{non-iso}}$. The normalised power is defined for any distance d as follows:

$$P_{L_{\text{norm}}} = \left. \frac{P_L^{\text{non-iso}}}{P_L^{\text{iso}}} \right|_{\forall d} \quad (3.23)$$

In order to know if the tag is powered up, for an arbitrary distance $d_0 < d_{\text{max}}$, one needs to compare $P_L^{\text{non-iso}}$ to the threshold power P_{th} . To power up the surrounded tag:

$$P_L^{\text{non-iso}} \Big|_{d=d_0} \geq P_{\text{th}} \quad (3.24)$$

Both sides of (3.24) can be divided by P_L^{iso} estimated at distance d_0 :

$$\frac{P_L^{\text{non-iso}} \Big|_{d=d_0}}{P_L^{\text{iso}} \Big|_{d=d_0}} \geq \frac{P_{\text{th}}}{P_L^{\text{iso}} \Big|_{d=d_0}} \quad (3.25)$$

According to the definition in (3.23):

$$P_{L_{\text{norm}}} \geq \frac{P_{\text{th}}}{P_L^{\text{iso}} \Big|_{d=d_0}} \quad (3.26)$$

This means that if $P_{L_{\text{norm}}} \geq 10 \log_{10} \left(\frac{P_{\text{th}}}{P_L^{\text{iso}} \Big|_{d=d_0}} \right)$ dB the tag is powered up.

At the maximum read-range $d = d_{\text{max}}$, we note $P_L^{\text{iso}} \Big|_{d=d_{\text{max}}} = P_{\text{th}}$. Consequently,

$P_{L_{\text{norm}}} \geq 0$ dB would designate an activated tag. This relationship between the normalised absorbed power and wake-up percentage of the tags is more explicitly quantified in the next chapter where a large number of random profiles of real tags is generated in a high density context. The results of the deterministic analysis presented in this section highlight the effect of coupling and randomness of antennas on the power budget which cannot be predicted for different configurations. A statistical study is therefore needed to compare the absorbed power of dipoles, with and without T-match to those of real tags in a high-density context.

3.4 RFID reverse link and differential RCS

The RCS of a tag does not only depend on its shape but also on its complex chip impedance. The tag responds to the reader by switching its input impedances between two states, typically a matched load (high impedance state) and a low impedance state, close to a short-circuit [37]. For each impedance state, represented by $Z_{L,1}$ and $Z_{L,2}$, the RFID tag exhibits a specific radar cross section, denoted by σ_1 (RCS₁) and σ_2 (RCS₂), respectively as illustrated in Figure 3.10. The difference between the RCS of two impedance states is referred to as differential RCS (ΔRCS) denoted by $\Delta\sigma$. In practice, RCS of a set of tags does not give any valuable information in an RFID system instead the readers are sensitive to differential radar cross section of a tag.

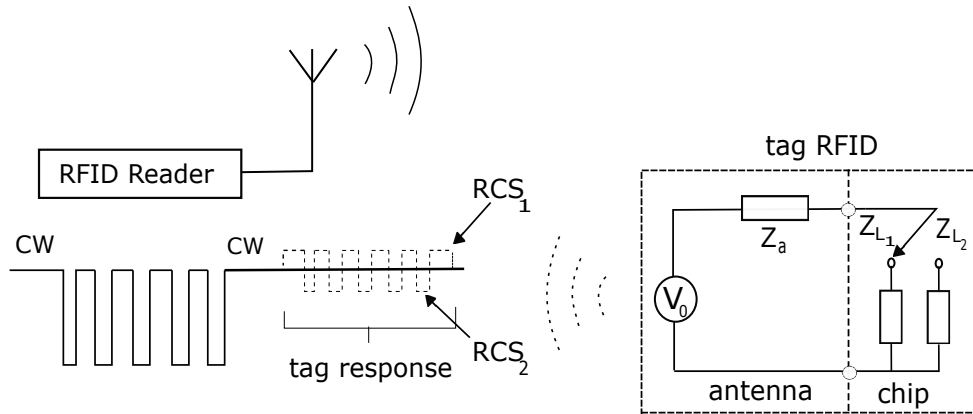


Figure 3.10: Data exchange between an RFID reader and a tag [42]

The section aims to analyze the distortion in backscattering when the distribution of the antennas is random in terms of position, orientation, and density. The monostatic RCS (σ) in dBm^2 of a set of randomly distributed loaded antennas is calculated first and then the differential RCS (in dBm^2) of each antenna in a set of randomly distributed antennas is estimated. Following are the techniques applied to calculate the RCS and consequently, ΔRCS of a tag in a set of randomly distributed antennas.

3.4.1 RCS definition [43]

The Radar Cross Section (RCS) can be defined as the effective area that an isotropic reflector would need to have in order to return the same amount of power per unit solid angle as the actual target when illuminated by an incident power density of P_i (measured in W/m^2). In mathematical terms, the power intercepted by the target with RCS (σ in m^2) from the incident power density P_i is σP_i . This intercepted power is then scattered uniformly in all directions, covering a full sphere of 4π , resulting in a power of $\frac{\sigma P_i}{4\pi}$ per steradian (W/str). Subsequently, considering a receiver with a certain power density (P_r) at its level in W/m^2 , the power intercepted by the receiver's antenna with its effective aperture area (A_e) is $P_r A_e$. This intercepted power is the same as the power reflected back to the receiver per unit solid angle, which can be expressed as $\frac{P_r A_e}{\Omega}$ in W/str , where Ω denotes the solid angle subtended by the receiver, and $\Omega = \frac{A_e}{d^2}$, where d is the distance from the target to the receiver. Therefore, according to the definition of RCS,

$$\frac{\sigma P_i}{4\pi} = \frac{P_r A_e}{\Omega} \quad (3.27)$$

After solving equation (3.27), σ is,

$$\sigma = 4\pi d^2 \frac{P_r}{P_i} \quad (3.28)$$

The power carried by an electromagnetic wave is proportional to the square of the electric field,

$$P \propto |E|^2 \quad (3.29)$$

, where $|E|$ is the magnitude of the electric field. If we relate the incident and scattered powers to the incident and scattered electric fields, we get,

$$\frac{P_r}{P_i} = \frac{|E_s|^2}{|E_i|^2} \quad (3.30)$$

Now, substituting equation (3.30) into the RCS equation (3.28),

$$\sigma = \lim_{d \rightarrow +\infty} 4\pi d^2 \frac{|E_s|^2}{|E_i|^2} \quad (3.31)$$

where E_s and E_i are the scattered and incident electric fields respectively. The limit $d \rightarrow +\infty$ indicates far-field conditions to ensure that the wavefront is planar [44]. This approach has been used in simulations in this work. Using NEC, either a plane wave is used to illuminate a set of antennas or an associated open circuit voltage (V^{OC}) is introduced at the level of each antenna instead. The corresponding mono-static RCS of a set of antennas is calculated using equation 3.31. The procedure to calculate the

backscattered electric field of a set of loaded antennas from NEC is detailed in Annex D. RCS obtained from two NEC-based models is further validated by HFSS.

3.4.2 RCS of a loaded antenna

Another method introduced by [45] is also used to calculate the mono-static RCS of a tag. Consider a Thevenin equivalent circuit of an RFID tag where the antenna is directly connected to the chip as shown in figure 3.11. $Z_a = R_a + j X_a$ is the complex antenna impedance and $Z_L = R_L + j X_L$ is the complex chip (load) impedance. To maximize the amount of collected power, the antenna impedance is usually matched with the chip (load) impedance. This is the analytical approach to derive an RCS for an RFID tag antenna terminating with any load impedance.

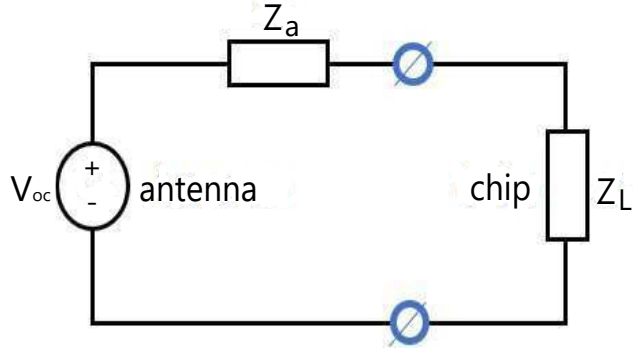


Figure 3.11: Equivalent circuit of an RFID tag

The re-radiated power can be obtained from the equivalent circuit shown in figure 3.11. The incident power density (P_i) in W/m^2 of an electromagnetic wave to the RFID tag antenna in free space is given by

$$P_i = \frac{P_t G_t}{4\pi d^2} \quad (3.32)$$

where P_t is the transmitted power in W, G_t is the gain of the reader and d is the distance from the tag in m. The collected power by the tag antenna P_r can be written as the product of incident power density P_i and effective aperture A_e of the tag antenna by considering the definition of maximum power delivered to the complex conjugate matched load.

$$P_r = P_i A_e \quad (3.33)$$

with

$$A_e = \frac{\lambda^2}{4\pi} G_{tag} \quad (3.34)$$

3.4 RFID reverse link and differential RCS

where G_{tag} is the gain of the tag antenna. The backscattered power P_{bs} from the tag on the reverse link can be found using equation 3.35. It is the power dissipated in the antenna resistance multiplied by antenna gain as

$$P_{bs} = |1 - \Gamma|^2 P_r G_{tag} \quad (3.35)$$

where Γ is the reflection coefficient due to the mismatch between the antenna and the load in the receiving mode and is given as:

$$\Gamma = \frac{Z_L - Z_a^*}{Z_L + Z_a} \quad (3.36)$$

Using equation (3.36), the term $|1 - \Gamma|^2$ is derived as follows,

$$|1 - \Gamma|^2 = \left| 1 - \frac{Z_L - Z_a^*}{Z_L + Z_a} \right|^2 \quad (3.37)$$

$$|1 - \Gamma|^2 = \left| \frac{(Z_L - Z_a) - (Z_L + Z_a^*)}{Z_L + Z_a} \right|^2 \quad (3.38)$$

After solving,

$$|1 - \Gamma|^2 = \left| \frac{Z_a + Z_a^*}{Z_L + Z_a} \right|^2 = \frac{4R_a^2}{|Z_L + Z_a|^2} \quad (3.39)$$

The RCS is then be calculated as

$$\sigma = \frac{P_{bs}}{P_i} G_{tag} = K A_e G_{tag} \quad (3.40)$$

After replacing each term by its expression, equation (3.40) becomes

$$\sigma = \frac{\lambda^2 G_{tag}^2 R_a^2}{\pi |Z_L + Z_a|^2} = \frac{\lambda^2 G_{tag}^2}{4\pi} |1 - \Gamma|^2 \quad (3.41)$$

This equation is valid when an antenna impedance is in static condition meaning that the load is not switched between two states. This analytical expression (3.41) is derived for an isolated case, particularly for a minimum scattering antenna. When the antenna is terminated by open circuit load or $\Gamma = 1$ in this equation (3.41), the scattering electric field from the antenna will be zero, thus the RCS of an antenna is zero and the antenna will turn into minimum scattering antenna [46]. This condition is only verified by the dipole antenna in our case. Therefore, to validate our methodology, a more general analytical formula is used [40], [47]. Inspired by Green's work [48], the scattered electric field (E_s) by an antenna terminated with any load impedance Z_L can be expressed as,

$$E_s = E_{\text{short}} - E_{\text{ant}} \frac{I_{\text{short}}}{I_{\text{ant}}} \frac{Z_L}{Z_L + Z_a} \quad (3.42)$$

where E_{short} and I_{short} are the electric field scattered and short circuit current induced due to the illumination of a plane wave on the antenna with short-circuited load impedance i.e. $Z_L=0$. E_{ant} is the electric field radiated by the antenna in transmitting mode, and I_{ant} is the antenna current in transmitting mode, which is equal to 1A in our study. Z_a is the input impedance of an isolated antenna terminated with any load impedance Z_L . This equation (3.42) will be further used to calculate the RCS of any antenna. However, we used equation (3.42) to estimate the RCS of isolated T-matched dipole and tag. The RCS obtained using formulae (3.41), used for isolated dipole and (3.42), used for isolated T-matched dipole and tag can be compared with the universal equation (3.31) of RCS using a backscattered field explained in the previous section 3.4.1.

3.4.3 Estimation of ΔRCS

As explained earlier, the difference between the two RCS values obtained from two impedance states ($Z_{L,1}$ and $Z_{L,2}$) is known as differential RCS (ΔRCS) denoted by $\Delta\sigma$. We have considered the widely used Nikitin's formulation [37], [42]:

$$\Delta\sigma = \sigma_d = \frac{\lambda^2 G_{\text{tag}}^2}{4\pi} |\Gamma_1 - \Gamma_2|^2 \quad (3.43)$$

with

$$\Gamma_1 = \frac{Z_{L,1} - Z_{in}^*}{Z_{L,1} + Z_{in}} \quad (3.44)$$

and

$$\Gamma_2 = \frac{Z_{L,2} - Z_{in}^*}{Z_{L,2} + Z_{in}} \quad (3.45)$$

where $Z_{L,1}$ and $Z_{L,2}$ are the two impedance states (short-circuited and matched load) of a tag of interest and Z_{in} is the input impedance of a tag of interest when others are terminated with a matched load.

It is important to note that [49] has brought a correction to this formulation, i.e. the total RCS of a modulated tag is given as,

$$\sigma = \sigma_s + \sigma_d = \frac{\lambda^2 G_{\text{tag}}^2}{4\pi} (|1 - \Gamma_s|^2 + |\Gamma_d|^2) \quad (3.46)$$

where $\Gamma_s = \frac{\Gamma_1 + \Gamma_2}{2}$ and $\Gamma_d = \frac{\Gamma_1 - \Gamma_2}{2}$. Consequently the differential RCS (σ_d) according to (3.46) differs from that of equation (3.43) by a factor of $\frac{1}{4}$. As the measurements were further performed using Voyantic Tagformance and the provided ΔRCS in the output file is obtained based on the Nikitin's formulation, the results presented hereafter are obtained by (3.43).

3.4.4 Simulation results of RCS and Δ RCS

Dipoles, with and without T-match and real tags at an operating frequency of 928MHz are used as targets to calculate the mono-static RCS and the associated differential RCS in dBm². Two terminating loads have been chosen to present the RCS results of an isolated antenna: $Z_L = 0$ and $Z_L = Z_a^*$, where Z_a is the input impedance of the antennas (dipole/tag). The rest of the subsection presents the simulation results of RCS and Δ RCS of a few deterministic cases in dBm².

RCS of isolated antennas

An isolated half-wave dipole placed symmetrically about the origin along the z -axis is shown in Figure 3.12 with the three planes ($\phi = 90^\circ$, $\phi = 0^\circ$, and $\theta = 90^\circ$) used for the study. First RCS is computed for two loads (short-circuited and matched) at an observation point P which is at a distance r from the dipole, using the two NEC-based models, validated by HFSS and the analytical equations (3.41) for dipole and (3.42) for T-matched dipole and tag. All three antennas are placed symmetrically about the origin along the z -axis as shown in Figure 3.2. Each of the isolated antennas is terminated with their respective loads employing linear polarisation of the incident field ($E_Z = 1$ V/m), and the results of RCS pattern are presented in Figure 3.13 and 3.14.

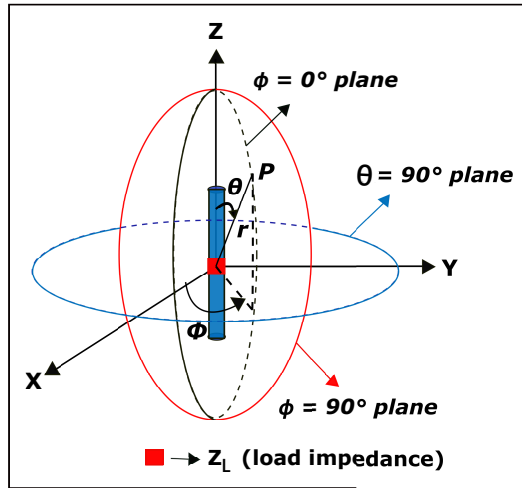


Figure 3.12: Isolated dipole and an arbitrary observation point P , illuminated by a linearly polarised plane wave.

It is observed that both NEC-based models (the plane wave and V^{OC} excitation) exhibit a strong agreement with HFSS and the analytical equation. The results for RCS reveal that the short-circuit load condition exhibits a higher value as compared to the matched load condition. This can be attributed to the fact that all the transmitted power is reflected back, resulting in higher backscattering and consequently higher RCS.

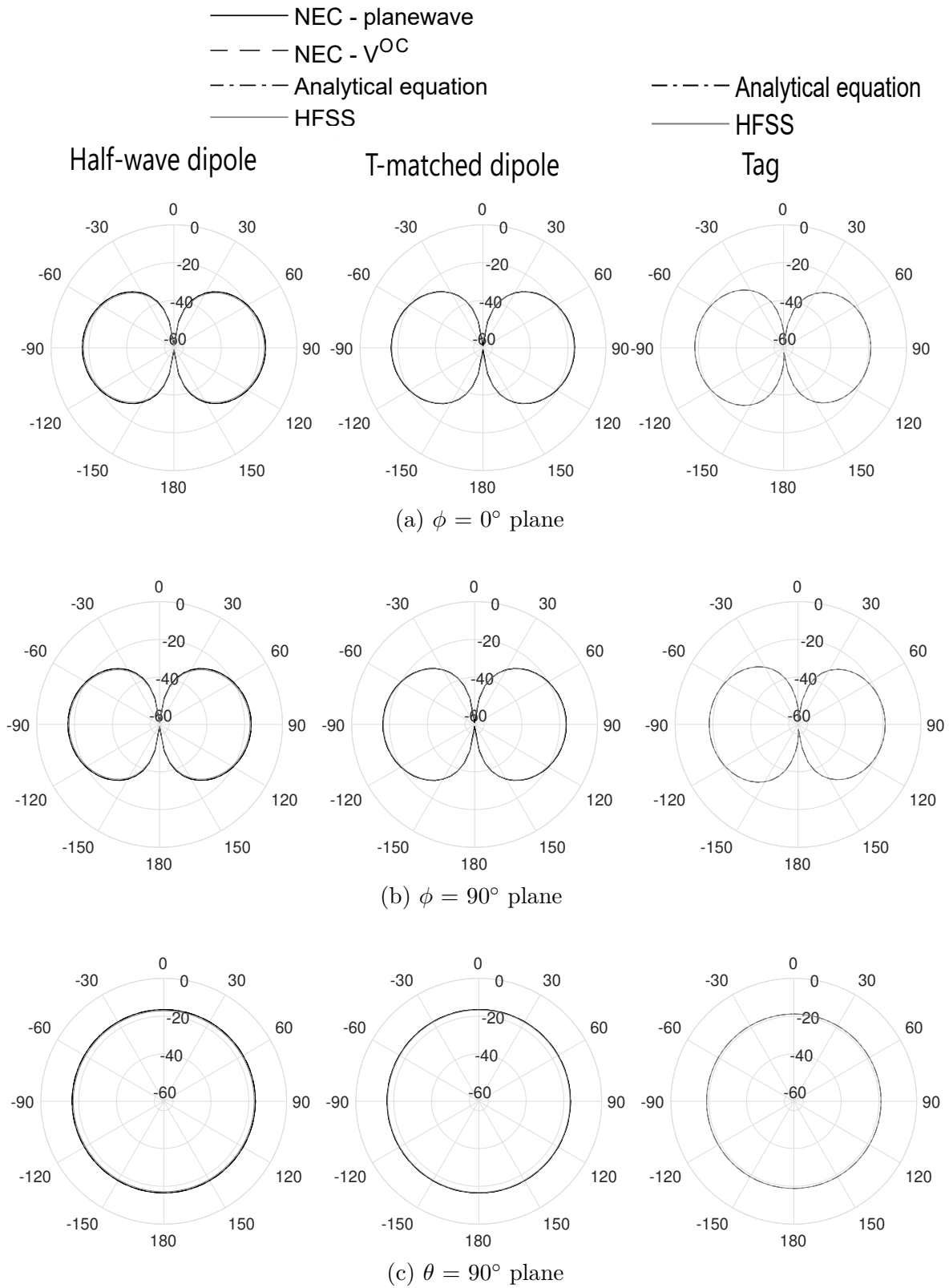


Figure 3.13: Mono-static RCS(σ) in dBm² of an isolated case terminated with matched load for three planes, (a) $\phi = 0^\circ$, (b) $\phi = 90^\circ$ and (c) $\theta = 90^\circ$ for a linear polarised plane wave.

3.4 RFID reverse link and differential RCS

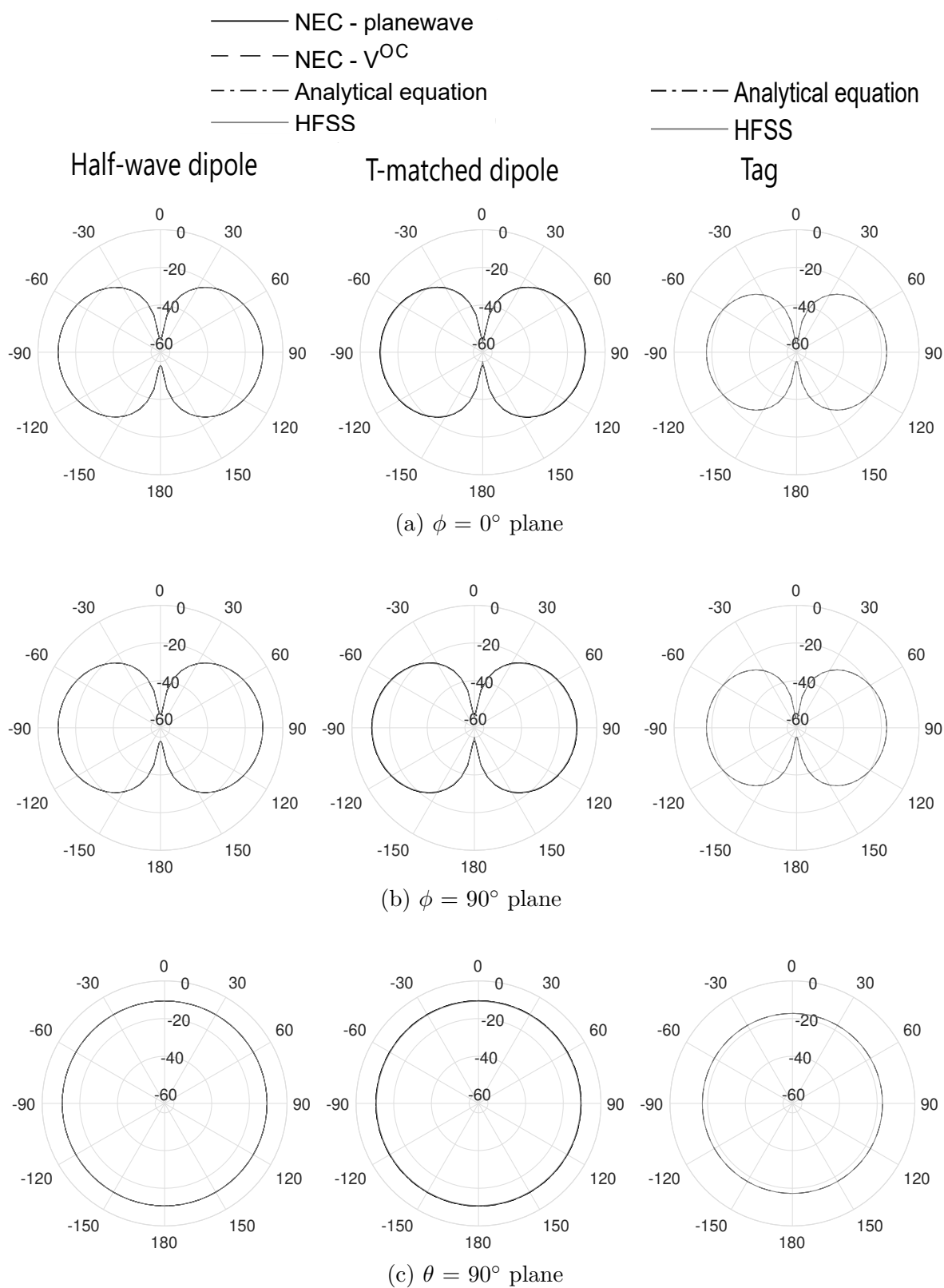


Figure 3.14: Mono-static RCS(σ) in dBm^2 of an isolated case terminated with short circuited load for three planes, (a) $\phi = 0^\circ$, (b) $\phi = 90^\circ$ and (c) $\theta = 90^\circ$ for a linear polarised plane wave.

The RCS pattern in $\phi = 0^\circ$ and $\phi = 90^\circ$ planes are identical as the antenna is isolated and its projection on any angle of ϕ plane would be the same. In the $\theta = 90^\circ$ plane, the angular distribution of RCS over all azimuth angles (ϕ) is observed to be constant. This value is equal to the maximum value of RCS in the $\phi = 0^\circ$ and $\phi = 90^\circ$ planes, as observed in the case of both loads. Although, the RCS values of each type of antenna is different because of the inherently different structures and designs, however, a correlation is observable between all three elements based on their respective RCS patterns as they have similar angular distribution. The absence of surrounding elements excludes the effect of mutual coupling and therefore it would be interesting to analyze the deformation of RCS pattern in terms of coupling in a given confined space. Subsequently, we will present a few configurations to illustrate the deformation of RCS within a high-density context using NEC with plane wave excitation for dipoles and T-matched dipoles and HFSS for the tags in the following section.

RCS of two parallel antennas

Consider a set of two parallel antennas terminated with matched load, placed at a distance d (chosen arbitrarily) from each other as shown in Figure 3.4. The chosen distance is 0.2λ at a working frequency of 928 MHz. NEC and HFSS are used to illuminate the set of dipoles, with and without T-match and tags respectively, by a linearly polarised plane wave of $E_z = 1$ V/m. The total mono-static RCS computed for the three planes is shown in Figure 3.15.

Due to the effect of coupling between two antennas, it is observed that RCS pattern is distorted, which is more visible in $\phi = 90^\circ$ and $\theta = 90^\circ$ planes as compared to the isolated one. Here, only the matched results are presented as short circuit loads will only yield to less amplitude in results. To have an insight into the effect of a more complex scenario, the number of antennas is increased.

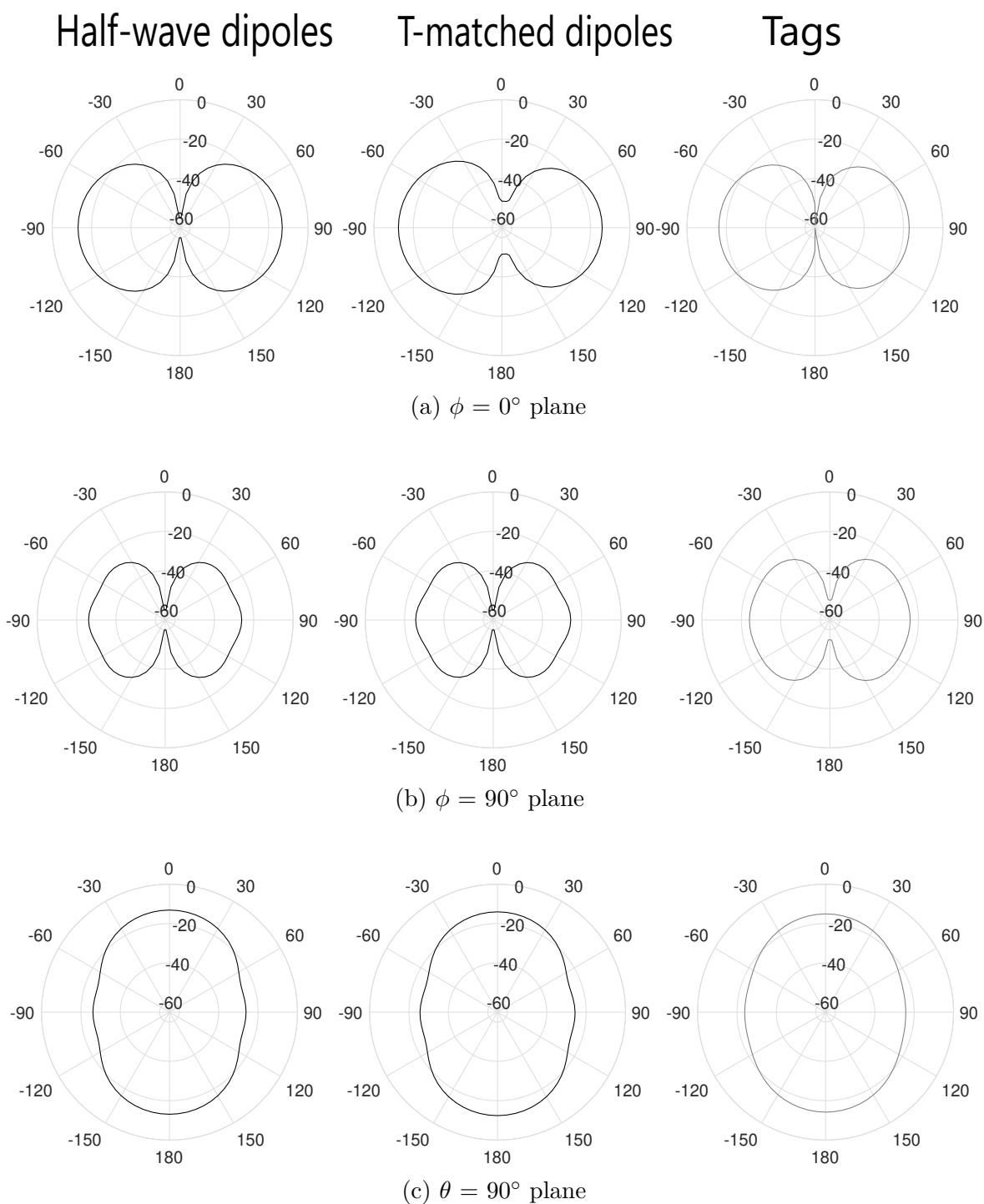


Figure 3.15: RCS(σ) in dBm² of two parallel antennas (c.f Fig. 3.4) terminated with matched load for three planes, (a) $\phi = 0^\circ$, (b) $\phi = 90^\circ$ and (c) $\theta = 90^\circ$ for a linear polarised plane wave using NEC (black solid line) and HFSS (grey solid line).

RCS of a set of ten randomly distributed antennas

Consider a set of ten identical matched dipoles/tags that are distributed randomly, as shown in Figure 3.6. Each antenna has random centre coordinates and orientation following the condition that they do not overlap. The set of antennas is illuminated by a linearly polarised plane wave of $E_z = 1\text{V/m}$. The results for the three planes are presented in 3.16 using NEC for the dipoles and T-match and HFSS for the tags. It is observed from the RCS plots that with increasing dipole density in the system, there will be more coupling among the antennas, resulting in a completely distorted RCS pattern. Due to the arbitrary position and orientation of antennas, it is observed that RCS is random and is difficult to predict in a deterministic manner.

From the above configurations of antennas, it is observed that the RCS patterns of dipoles, T-matched dipoles and tags are similar, although not exactly same. As we discussed earlier, the RCS of a group of antennas does not bring any significant information, therefore, ΔRCS of each of the tags in a set of antennas is calculated in the following section to have an insight of a real RFID scenario.

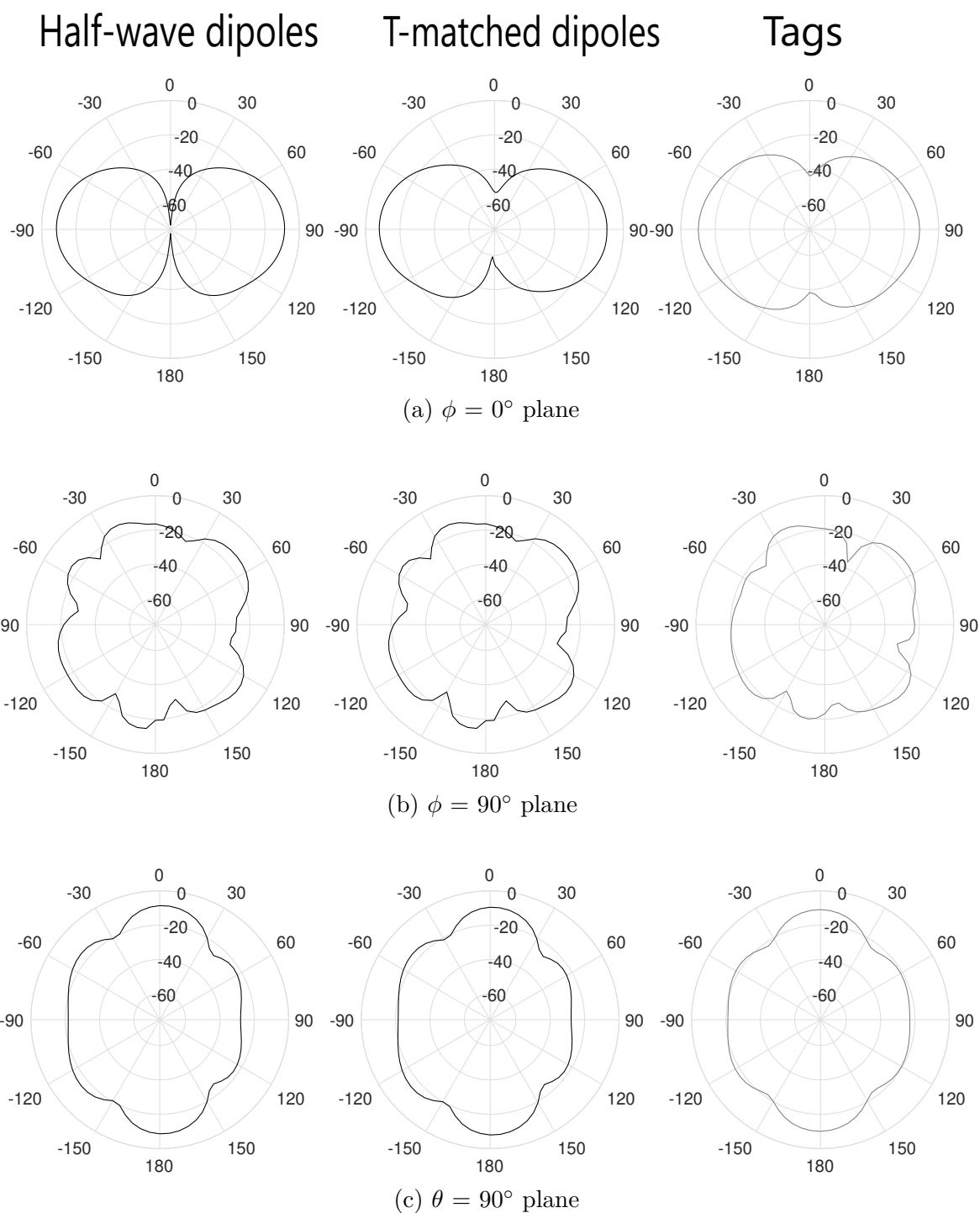


Figure 3.16: Mono-static RCS(σ) in dBm^2 of ten randomly distributed antennas (c.f Fig. 3.6) terminated with matched load for three planes, (a) $\phi = 0^\circ$, (b) $\phi = 90^\circ$ and (c) $\theta = 90^\circ$ for a linear polarised plane wave using NEC (black solid line) and HFSS (grey solid line).

Differential RCS of a few configurations

Let's first discuss the differential RCS in the case of the isolated dipole with and without T-match and real tag as shown in Figure 3.2 using equation (3.43). The gain used in this equation is extracted for $\phi=0^\circ, \theta=90^\circ$ plane, which corresponds to the estimation of ΔRCS in normal incidence. Considering the difference between the matched and short impedance states using equation (3.43), the ΔRCS of the isolated dipole with and without T-match and tag is given in Table 3.1.

Type of antenna	ΔRCS ($\Delta\sigma$) in dBm ²
Half-wave dipole	-16.52
T-matched dipole	-16.78
ALN-9662 tag	-17.59

Table 3.1: ΔRCS in dBm² of the isolated dipole with and without T-match and real tag, illuminated by a linearly polarised plane wave at a normal incidence.

It is observed that the isolated dipole with and without T-match have a similar value of ΔRCS compared to the tag. It would be interesting to find the lower limit of ΔRCS being detected by the reader. Therefore, a typical value of $\Delta\sigma$ as per ISO/IEC 18000-6 [7], should be greater than 0.005m² (-23dBm^2), in order to get detected by the reader. This recommendation is respected for isolated antennas, as their respective ΔRCS is higher than -23dBm^2 (Table 3.1). This anticipation stems from the elimination of coupling, allowing the isolated tag to act as an ideal case, by simply subtracting its two impedance states. For a high-density context, where the tags are strongly coupled and randomly distributed in a reduced volume, let's keep the lower limit in mind for our conclusion.

Another configuration, where a set of two parallel antennas are placed at a distance d , as shown in Figure 3.4 is taken into consideration. The input impedance of an antenna of interest is estimated by exciting it with the current in NEC and by the lumped port in HFSS while keeping the second antenna in matched condition. The gain of the excited antenna is calculated in the direction of normal incidence ($\phi=0^\circ, \theta=90^\circ$). Three distances, $d = 0.1\lambda$, $d = 0.2\lambda$ and $d = 0.3\lambda$, between two parallel antennas are taken into account for the evaluation of ΔRCS . Dipoles and T-matched dipoles are simulated from NEC and HFSS is used for the tag. The ΔRCS in dBm² of two parallel antennas is then estimated using the equation (3.43) and given in Table 3.2.

The degradation in ΔRCS between two parallel antennas compared to the isolated case has been noted. However, a definitive conclusion cannot be drawn at this stage. To further investigate, a more intricate configuration was employed. For this, a set of ten randomly distributed antennas over a surface area of $1\lambda \times 1\lambda$ in YOZ plane,

3.4 RFID reverse link and differential RCS

Table 3.2: Δ RCS in dBm² of two parallel dipoles, T-matched dipoles and tags in the direction of normal incidence, placed at a distance of 0.1λ , 0.2λ and 0.3λ .

Dipoles	0.1λ	0.2λ	0.3λ
N°1	-20.46	-21.43	-20.51
N°2	-20.46	-21.43	-20.51

T-match	0.1λ	0.2λ	0.3λ
N°1	-19.00	-20.09	-19.55
N°2	-19.00	-20.09	-19.55

Tag	0.1λ	0.2λ	0.3λ
N°1	-18.66	-19.00	-21.61
N°2	-18.66	-19.00	-21.61

the same as shown earlier in Figure 3.6. The input impedance of a tag of interest is calculated by exciting the antenna with the current of 1A in NEC and by lumped port in HFSS while keeping all the other antennas in matched condition. NEC is used for the dipoles and T-matched dipoles while HFSS is used for the tag. The gain of the excited antenna in the presence of other loaded antennas is extracted for $\phi=0^\circ, \theta=90^\circ$ plane and Δ RCS has been estimated using equation (3.43). Dipoles and T-match dipoles are simulated with NEC and HFSS is used for the tag. The Δ RCS in dBm² of ten dipoles with and without T-match and tags is given in Figure 3.17.

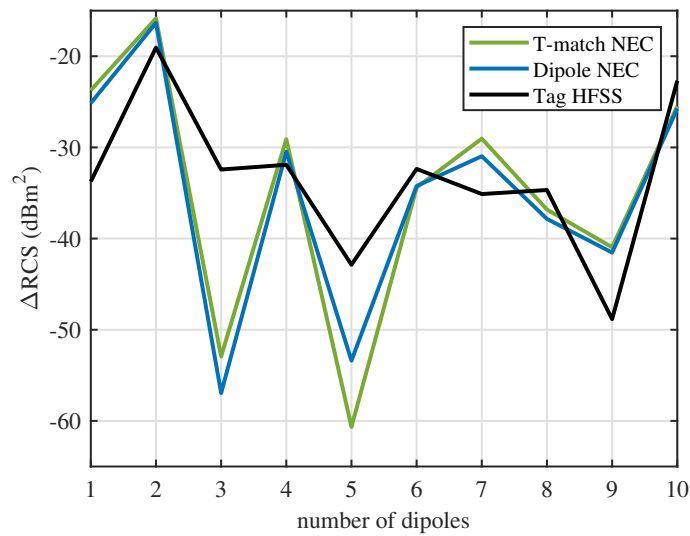


Figure 3.17: Δ RCS of a set of ten randomly distributed antennas over a surface of dimensions $1\lambda \times 1\lambda$.

There is a clear correlation estimated for dipoles and T-matched dipoles and

it seems they are following similar evolution. The tags on the other hand are very different. Among the set of ten dipoles with and without a T-match network and tags, antenna no.2 has a value greater than the given threshold of -23dBm^2 which is due to the fact that this antenna is exposed to less coupling and is far from the other antennas as clearly seen in Figure 3.6. The ΔRCS is a critical parameter to estimate, and therefore to achieve a realistic conclusion, this parameter needs to be analysed on a large scale in a high-density context later in this work. Although it is observed that the evolution of linear ΔRCS is similar to that of the P_L estimated in the forward link which could encourage us to proceed further and allow us to evaluate the similarities between three types of antennas in both RFID links statistically.

3.5 Conclusion

This chapter introduced a conventional network grid of tags and conducted a thorough power budget analysis. We presented two NEC-based models and validated our results through HFSS simulations plus an analytical equation for the isolated cases. We delve into the impact of polarisation and antenna orientation, considering the presence or absence of adjacent dipoles/tags, which either enhance or suppress coupling effects. Examining the absorbed power at the load associated to the forward link, we explored scenarios with a specific antenna density. These antennas were terminated with matched loads, and we explored the linear and circular polarisation of a plane wave. This technique enabled the assessment of the percentage of inactive tags using the concept of normalised absorbed power in the forward link. When combined with the reverse link, we presented the Radar Cross Section (RCS) of loaded scatterers terminated with short-circuited and matched loads. We also introduced the concept of differential RCS while explaining the backscattering phenomenon. Predicting the performance degradation resulting from antennas' position and orientation is challenging with a deterministic approach, particularly for a group of strongly coupled dipoles/tags. Hence, a statistical evaluation becomes essential, especially when dealing with intricate scenarios which will be studied next in this thesis.

3.5 Conclusion

,

Chapter 4

Statistical evaluation of RFID links in a high-density context

After having focused on studying the impact of coupling on the position and orientation of antennas under various conditions such as the density of the antennas, polarisation of the incident wave and the angle of incidence, including the use of dipoles with and without T-match, and the real RFID tags, it was observed that a fully deterministic model is not realistic and a statistical analysis is essential. This approach will eventually make it possible to predict the correlation of the dipole and T-matched dipole to those of real tags in both forward and reverse links in a high-density context. Therefore, the two key parameters of the forward and reverse link i.e. absorbed power and ΔRCS have been analysed statistically in this chapter. This allows us to use the appropriate method to collect data, process and analyze them to present the results effectively in order to facilitate the understanding of the respective phenomena on large random profiles of antennas.

4.1 Methodology

The electromagnetic simulations are performed by NEC and HFSS. These simulators require input data, which are recorded in a file written in a specific format. These input files can be generated manually or automatically using the software's GUI as shown in Figure 4.1. However, both simulators require manual execution of the simulations, which is incompatible with performing statistical studies that involve a high number of realizations. To overcome this issue, we have developed a MATLAB code that automates the generation of input files containing the necessary geometry and simulation parameters. These input files are then transferred to the respective tool either NEC or HFSS without going through the software's GUI. The output files containing the simulation results are also processed by MATLAB. The entire simulation process is automated through various steps, as mentioned in Annex B.

4.1 Methodology

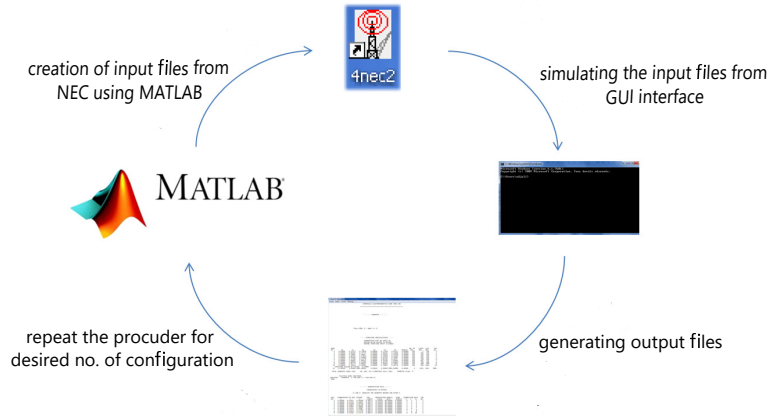


Figure 4.1: Automation steps of simulating files from NEC.

The objective is to generate random profiles, based on a uniform distribution, for the centres and inclination angles of N antennas while adhering to the predefined surface dimensions. The program verifies that there is no overlapping between the antennas before generating a new configuration randomly. This approach is repeated until thousands of configurations of N antennas in each set are generated and randomly distributed on the given surface area. The number of configurations is chosen to guarantee the convergence of the statistical analysis in all cases. The antennas are loaded and excited by a linearly and circularly polarised incident wave in a normal incidence. The angle of incidence has been fixed as for the 2D configuration, the normal incidence seems to be the most instinctive. For each configuration, the power absorbed by the load P_L and ΔRCS is calculated for each antenna using the NEC simulator for dipoles and T-matched dipoles and HFSS for real tags. This process is repeated for different surface areas with varying antenna density, ranging from the lowest density to the highest at 928 MHz. It is interesting to note that the calculation time of the two softwares are not comparable. While HFSS takes months to complete such a large set of simulations for one density and for one polarisation, NEC's calculation time would be around a few hours.

4.2 Statistical analysis in the forward link

In this section, we will examine the forward link analysis of antennas in terms of the absorbed power collected at their load level. The cumulative distribution functions (CDF) of the normalised absorbed power (P_{Lnorm}) are presented using dipoles, with and without T-match and real tags. Our aim is to compare the statistical behaviour of the three types of antennas in the forward link.

The study has been done using a linear and circular polarisation of an incident wave. 10 identical antennas, dipoles (with and without T-match) are distributed randomly in surfaces of different dimensions from $4\lambda \times 4\lambda$ to $1\lambda \times 1\lambda$. The real tags are only considered in the highest density which is $1\lambda \times 1\lambda$, and in the case of linear polarisation, because the simulation would take 7 months to complete all the performed trials with NEC. 2000 random profiles are generated for each area. The antennas are all terminated into their isolated matched load. Before presenting the statistical analysis, the key parameters of the study, are summarised in Table 4.1.

Parameters	Assigned values
Number of antennas	10
Number of configurations	2000
Frequency	928 MHz
Polarisation	Linear and Circular
Plane wave	$E_z = 1V/m, \phi = 0^\circ, \theta = 90^\circ$
Antenna densities ($B\lambda \times B\lambda$)	$B = 1,2,3,4$

Table 4.1: Key parameters of statistical studies for forward link

Table 4.2 gives insight by presenting the mean (μ), the standard deviation (σ), and the coefficient of variation (σ/μ) of the absorbed power for different cases. It can be stated that the mean absorbed power is mainly related to the density of dipoles, i.e. the lower the density, the better would be the level of absorbed power. We find that the dispersion of the absorbed powers decreases with increasing distribution surface. Thus the dispersion is largest for $1\lambda \times 1\lambda$ surface and smallest for $4\lambda \times 4\lambda$ surface area. This is due to the fact that for a high antenna density, the overall impact of the mutual coupling is greater compared to the lower density. This dispersion is even more important for linear polarisation but for a given distribution area, the mean power (μ) for the linear and circular polarisations are almost the same. There is a drastic increase in the mean powers from $1\lambda \times 1\lambda$ to $2\lambda \times 2\lambda$ distribution area. Though it does not change much for the other lower antenna densities.

In sum, the coefficient of variance ($CV = \sigma/\mu$) is always higher for the linear polarisation compared to the circular one while on average there is no impact of po-

4.2 Statistical analysis in the forward link

larisation of a plane wave on the absorbed power. The more dispersion in LP could be due to the fact that a linearly polarised plane wave includes coupling between antennas plus the effect of randomness in the orientation of antennas and polarisation mismatch while in a circularly polarised plane wave, it only includes the effect of coupling between antennas.

Table 4.2: Statistical moments of the absorbed power

		μ		σ		σ/μ
		(μW)	(dBm)	(μW)	(dBm)	
Dipole						
$1\lambda \times 1\lambda$	LP	4.19	-23.78	4.32	-23.65	1.03
	CP	4.19	-23.78	3.02	-25.20	0.72
$2\lambda \times 2\lambda$	LP	7.82	-21.07	6.42	-21.92	0.82
	CP	7.87	-21.04	3.45	-24.62	0.44
$3\lambda \times 3\lambda$	LP	8.72	-20.59	6.71	-21.73	0.77
	CP	8.67	-20.62	2.80	-25.53	0.32
$4\lambda \times 4\lambda$	LP	8.90	-20.51	6.63	-21.79	0.74
	CP	8.90	-20.50	2.30	-26.39	0.26
T-match						
$1\lambda \times 1\lambda$	LP	4.96	-23.04	4.88	-23.11	0.98
	CP	4.96	-23.04	3.19	-24.96	0.64
$2\lambda \times 2\lambda$	LP	8.87	-20.56	7.10	-21.49	0.81
	CP	8.85	-20.53	3.58	-24.46	0.40
$3\lambda \times 3\lambda$	LP	9.75	-20.12	7.43	-21.29	0.76
	CP	9.70	-20.13	2.90	-25.38	0.30
$4\lambda \times 4\lambda$	LP	9.95	-20.02	7.35	-21.33	0.74
	CP	9.95	-20.02	2.37	-26.25	0.24
Tag						
$1\lambda \times 1\lambda$	LP	3.76	-24.25	3.96	-24.02	1.05

We intend to analyse two things primarily. Firstly, to quantify the degradation of the absorbed power as a consequence of coupling and polarisation of the incident wave compared to the isolated case. Secondly, to predict the correlation and statistical similarities between three types of antennas in terms of absorbed power. For these, the CDF plots of normalised absorbed powers of each antenna have been traced for four antenna densities. Figure 4.2 presents the CDF plots of the absorbed power of dipoles/T-match dipoles and tags normalised by their respective absorbed powers when they are isolated and illuminated by a circular polarisation. This can be explained as

follows,

Table 4.3: Isolated power for Linear Polarisation (LP)

	Dipole		T-match		Tag	
	dBm	μW	dBm	μW	dBm	μW
P_L^{iso}	-17.4	18.1	-17.3	18.6	-18.1	15.5

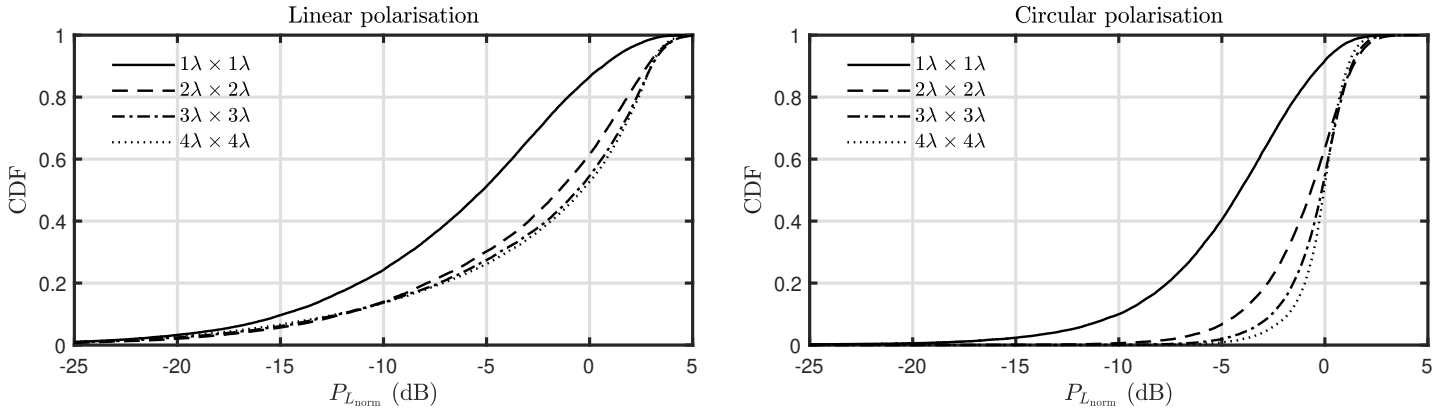
Table 4.4: Isolated power for Circular Polarisation (CP)

	Dipole		T-match		Tag	
	dBm	μW	dBm	μW	dBm	μW
P_L^{iso}	-20.4	9.0	-20.3	9.3	-21.1	7.7

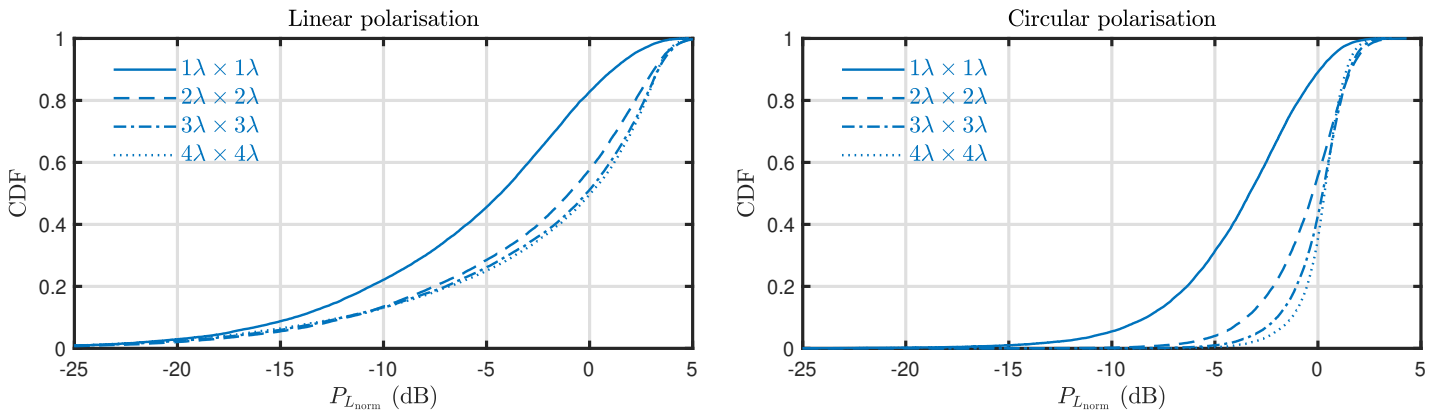
According to Table 4.3, with a linearly (vertically) polarised plane wave with $E_Z = 1$ V/m, the power at the load level of an isolated vertical dipole is equal $P_{L_0} = -17.4$ dBm. An isolated dipole inclined at 45° receives half of this power: $P_{L_{45}} = -20.4$ dBm. On the other hand, the mean value of the absorbed power for 20000 dipoles (2000 configurations of 10 dipoles) without coupling is equal to -20.4 dBm (Figure 3.3). This shows that the 45° inclined dipole can be seen as a good representative of the average polarisation effect in the absence of coupling. According to Table 4.4, with a circularly polarised plane wave with the same field intensity, the power at the load level of an isolated vertical dipole is equal to -20.4 dBm, and this would be the absorbed power at the level of any single dipole, regardless of its orientation. The same argument is valid for the dipole with T-match and the tag. Consequently, the CDF plots of Figure 4.2 have been traced after normalising the absorbed power in each random configuration by the absorbed power of the antenna illuminated by a circularly polarised plane wave.

We observe that the normalised CDF plots of dipole without T-match in Figure 4.2 (a) and with T-match in Figure 4.2 (b) are similar, and a larger difference appears for the denser configuration, i.e. $1\lambda \times 1\lambda$ in both cases. Figure 4.2 (c) presents the CDF plot of tags compared with those of dipoles, with and without T-match, illuminated by a linearly polarised plane wave for a distribution surface of $1\lambda \times 1\lambda$. According to this figure, the normalised $P_{L_{norm}} = 0$ dB represents the absorbed power by the isolated antenna which is called hereafter as P_L^{iso} . The provided Table 4.5, displays the percentages of the dipoles/T-match and tags that are considered appropriate for a specific threshold on the normalised absorbed power. This threshold is fixed at 0 dB.

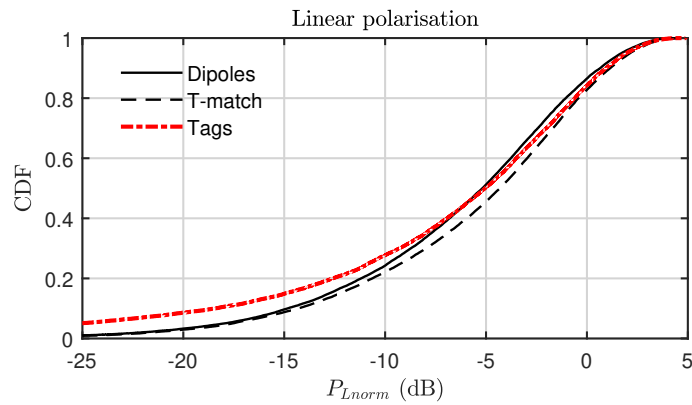
4.2 Statistical analysis in the forward link



(a) Half-wave dipoles



(b) T-matched dipoles



(c)

Figure 4.2: CDF plots for the normalised absorbed power ($P_{L_{\text{norm}}}$) in dB of 2000 configurations of 10 randomly distributed matched dipoles without T-match (black line) in (a) and with T-match (blue line) in (b), illuminated by a linearly and circularly polarised wave over four distribution surface areas and compared with the matched tags (red thick line) for one distribution surface of $1\lambda \times 1\lambda$ in (c) with linear polarisation.

Let us consider the linear polarisation in the case of $1\lambda \times 1\lambda$ distribution area. By referring to the respective CDF curve in Figure 4.2(a) and 4.2(b) and in Table 4.5, one may note that 86% of dipoles without T-match and 83% of dipoles with T-match show a power lower than P_L^{iso} as a result of the mutual coupling. As expected, this percentage is reduced to 53% (without T-match) and 50% (with T-match) for the $4\lambda \times 4\lambda$ randomly distributed case, which has the lowest dipole density. We can observe that the drastic difference is observed only in the highest dipole density which is $1\lambda \times 1\lambda$, while for other dipole densities and distribution surface areas, this percentage is not reduced much. As for the real tag, the normalised CDF relies close to the corresponding CDF plots of Figure. 4.2 (c). This tendency is valid for linear polarisation for all three antennas. In the case of circular polarisation, there is a notable deviation as shown in Table 4.5. The T-matched dipoles for a distribution surface area of $3\lambda \times 3\lambda$ and $4\lambda \times 4\lambda$ have a better percentage in terms of samples having $P_{L\text{norm}} < 0$ dB, compared to the half-wave dipoles. This shows that T-matched dipoles behave better for lower coupling. Figure 4.3 shows the comparison of the T-matched dipoles and half-wave dipoles for two densities in the case of circular polarisation. However, the slope of the curves is very similar for both antennas but there is a clear steep in both curves which is why the percentages are very different.

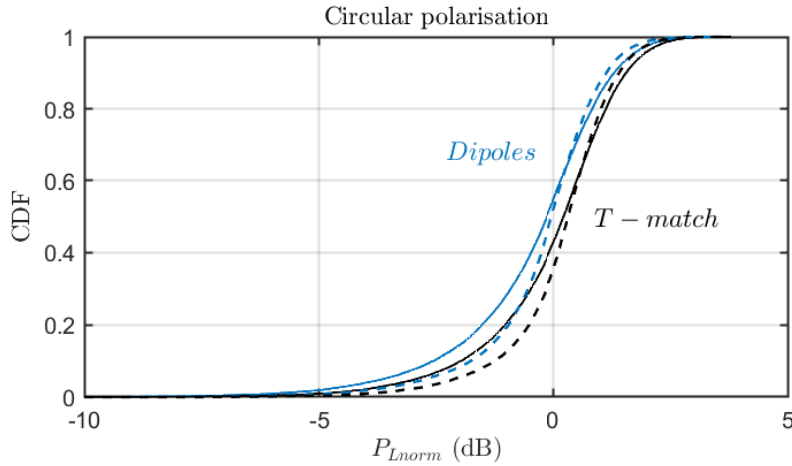


Figure 4.3: CDF plot for the normalised absorbed power in 2000 configurations of 10 randomly distributed matched dipoles and T-matched dipoles illuminated by a circularly polarised wave over $3\lambda \times 3\lambda$ (solid line) and $4\lambda \times 4\lambda$ (dotted line) surface area.

4.2 Statistical analysis in the forward link

Table 4.5: Percentage of dipole, T-match and tag with a normalised absorbed power lower than the $P_{L_{\text{norm}}} = 0$ dB.

Dipole				
	$1\lambda \times 1\lambda$	$2\lambda \times 2\lambda$	$3\lambda \times 3\lambda$	$4\lambda \times 4\lambda$
LP	86%	62%	55%	53%
CP	92%	63%	54%	52%

T-match				
	$1\lambda \times 1\lambda$	$2\lambda \times 2\lambda$	$3\lambda \times 3\lambda$	$4\lambda \times 4\lambda$
LP	83%	58%	51%	50%
CP	89%	56%	43%	35%

Tag	
	$1\lambda \times 1\lambda$
LP	84%

In Chapter 3, we have shown the contribution of coupling and orientation of antennas versus the polarisation of the plane wave in a deterministic case (Figure 3.7), where both orientation and coupling influence the power budget with linear polarisation, as opposed to circular polarisation which is insensitive to orientation due to which the power budget is modified only as a result of coupling. Some dipoles have a better absorbed power with circular polarisation (e.g. number 5) and others with linear polarisation (e.g. number 2). After discussing a deterministic case, it is interesting to compare the CDF plots of dipoles with and without a T-match network illuminated by a linear and circular polarisation of an incident wave for two distribution surface areas, $2\lambda \times 2\lambda$ and $4\lambda \times 4\lambda$ as shown in Figure 4.4. This shows that for a given distribution area, the normalised CDF plots for linear and circular polarisations intercept, meaning that the coupling effects are not always higher for linear polarisation. Also, the mean value of the absorbed power is almost the same for both polarisations (refer to Table 4.2) statistically.

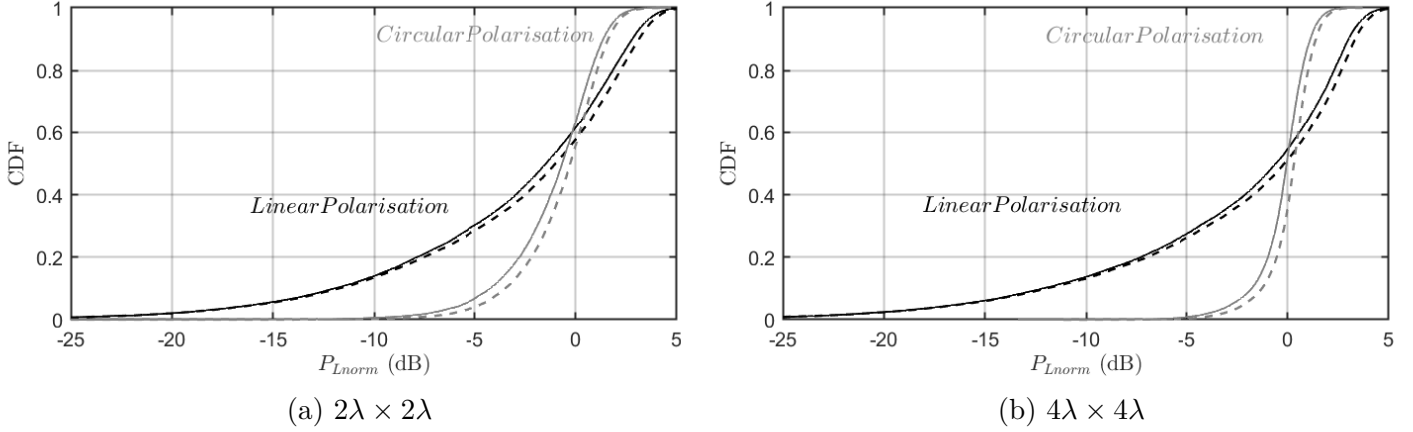


Figure 4.4: CDF plots for the normalised absorbed power ($P_{L_{\text{norm}}}$) in dB of 2000 configurations of 10 randomly distributed matched dipoles without T-match (solid line) and with T-match (dotted line), illuminated by a linearly and circularly polarised wave over two distribution surface areas of $2\lambda \times 2\lambda$ in (a) and $4\lambda \times 4\lambda$ in (b).

Valuable information can be extracted from the empirical cumulative distribution functions (CDF) of the various power levels in the case of a forward link. For example, in a real case scenario, by fixing on the x -axis the minimum required absorbed power (threshold of the tag) and by using the P_L curve, one can read the percentage of tags showing a lower power across their loads. Thus, an estimation of the percentage of non-activated tags may be obtained.

Another important aspect that could be analysed from the normalised absorbed power curves, is the percentage of the tags that are activated. The CDF plots of real tags are also useful to predict this percentage provided that they are accompanied by the tag-to-reader distance as well as the power absorbed by the isolated tag at this distance. The normalised power in dB is defined as $P_{L_{\text{norm}}} = P_L^{\text{non-iso}} - P_L^{\text{iso}}$, where $P_L^{\text{non-iso}}$ and P_L^{iso} are the absorbed powers of the chip in the case of a surrounded tag and an isolated tag, respectively. The normalised power is the same at any distance from the reader. In order to power up a surrounded tag at an arbitrary distance d_0 , the chip power in the non-isolated case $P_L^{\text{non-iso}}$ should be larger than the threshold power of the chip P_{th} . Thus the surrounding tag replies if,

$$P_L^{\text{non-iso}} \Big|_{d=d_0} \geq P_{\text{th}} \quad (4.1)$$

Subtracting $P_L^{\text{iso}} \Big|_{d=d_0}$ from both sides of (4.1):

$$\begin{aligned} P_L^{\text{non-iso}} \Big|_{d=d_0} - P_L^{\text{iso}} \Big|_{d=d_0} &\geq P_{\text{th}} - P_L^{\text{iso}} \Big|_{d=d_0} \\ P_{L_{\text{norm}}} &\geq P_{\text{th}} - P_L^{\text{iso}} \Big|_{d=d_0} \end{aligned} \quad (4.2)$$

4.2 Statistical analysis in the forward link

In this equation P_{th} is known by the data-sheet of the chip and $P_{L_{\text{iso}}}|_{d=d_0}$ should be estimated or measured for a given tag at distance d_0 . The condition obtained in (4.2) designates the statistics of the replying tags over the normalised CDF curve of Figure 4.2 (c). This analysis may lead us to the particular case of the maximum read-range of the system, where $d = d_{\text{max}}$ and the absorbed power of an isolated tag is equal to its threshold $P_L^{\text{iso}}|_{d=d_{\text{max}}} = P_{\text{th}}$. Consequently, the condition obtained in (4.2) is reduced to $P_{L_{\text{norm}}} \geq 0$ dB. In this special case, $P_{L_{\text{norm}}} \geq 0$ dB over the normalised CDF curve of Figure 4.2 (c) designates not only the percentage of tags for which the coupling effects have a beneficial impact but also those of which are going to be powered up. This will be further illustrated by an example. We have reproduced the CDF curve of the tags in Figure 4.5 in order to develop an example.

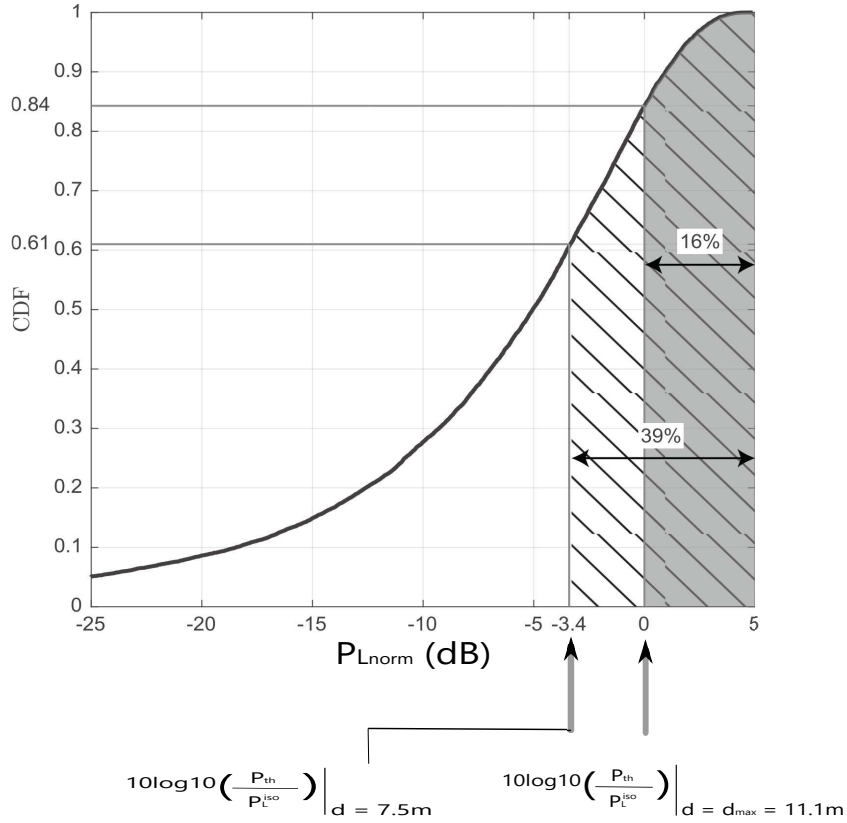


Figure 4.5: CDF plot for the normalised absorbed power in 2000 configurations of 10 randomly distributed matched tags illuminated by a linearly polarised wave over $1\lambda \times 1\lambda$ area.

The characteristics of the RFID system and the real RFID tag are as follows:

- $G_{\text{tag}} = 1.4361$ (by simulating the tag antenna with HFSS)
- $Z_{\text{chip}} = 26.66 - j198.2$ (from data-sheet)
- $Z_{\text{antenna}} = 23.6 + j197.9$ (by simulating the tag antenna with HFSS)

- $|\Gamma| = \left| \frac{Z_{\text{chip}} - Z_{\text{antenna}}^*}{Z_{\text{chip}} + Z_{\text{antenna}}} \right| = 0.0612$
- $P_{\text{th}} = -16$ dBm (from Voyantic)
- $P_{\text{EIRP}} = 3.28$ W (from Voyantic)

The maximum read range of the system is estimated to be $d_{\text{max}} = 11.1$ m using equation (3.21). At this distance, $P_{L_{\text{norm}}} \geq 0$ dB designates the region where the tags are powered-up. According to Figure 4.5, this corresponds to 16% of the tags. At a smaller distance, e.g. $d = 7.5$ m, the absorbed power of an isolated tag can be estimated using (3.21) and would be equal $P_L^{\text{iso}} = -12.58$ dBm while $P_{\text{th}} = -16$ dBm. The CDF curve of Figure 4.5 implies that 39% of the tags are powered-up as $P_{L_{\text{norm}}} \geq -3.42$ dB. The preliminary statistical results show a non-negligible influence of the coupling on the received power at the level of the chip. This technique allows the quantification of the percentage of tags that are not powered up in a given scenario. Combined with the reverse link, this statistical analysis would help the RFID designer to assess the performance of the RFID link.

4.3 Statistical analysis in the reverse link

This section is dedicated to the statistical evaluation of the reverse link in terms of differential RCS in the direction of the reader. The cumulative distribution functions (CDF) of the ΔRCS in dBm² are presented using dipoles, with and without T-match. Our aim is to compare the statistical behaviour of the two types of antennas in the reverse link. Referring to Table 3.1, the ΔRCS of the isolated dipole, T-match and tag is -16.52 dBm², -16.78 dBm² and -17.59 dBm² respectively. The degradation in terms of ΔRCS is also studied here in comparison of the isolated case. The results do not contain the real tags as the electromagnetic simulations using HFSS are extremely time consuming.

The study has been done using the analytical equation (3.43). 10 identical antennas, dipoles with and without T-match are distributed randomly in surfaces of different dimensions from $2\lambda \times 2\lambda$ to $1\lambda \times 1\lambda$. 2000 random profiles are generated for each area. The input impedance and the gain of the antenna of interest are calculated using NEC, while all the other antennas are terminated with their isolated matched load. The gain is extracted for $\phi=0^\circ$, $\theta=90^\circ$ plane in order to estimate differential RCS in a normal incidence. Before presenting the statistical analysis, the key parameters of the study, are summarised in Table 4.6.

4.3 Statistical analysis in the reverse link

Parameters	Assigned values
Number of antennas	10
Number of configurations	2000
Frequency	928 MHz
Gain extracted	$\phi = 0^\circ, \theta = 90^\circ$
Antenna densities ($B\lambda \times B\lambda$)	$B = 1, 2$

Table 4.6: Key parameters of statistical studies for backward link

Table 4.7: Statistical moments of the differential RCS

	μ (m ²)	μ (dBm ²)	σ (m ²)	σ (dBm ²)	σ/μ
Dipole					
$1\lambda \times 1\lambda$	0.0033	-24.84	0.0072	-21.40	2.20
$2\lambda \times 2\lambda$	0.0083	-20.82	0.0129	-18.89	1.56
T-match					
$1\lambda \times 1\lambda$	0.0038	-24.19	0.0120	-19.20	3.15
$2\lambda \times 2\lambda$	0.0090	-20.45	0.0136	-18.65	1.51

Table 4.7 gives insight by presenting the mean (μ), the standard deviation (σ), and the coefficient of variation (σ/μ) of the Δ RCS for different cases. It can be stated that the mean differential RCS is mainly related to the density of antennas, i.e. the lower the density, the better would be the level of Δ RCS. We find that the dispersion of the differential RCS decreases with increasing distribution surface. Thus the dispersion is larger for a $1\lambda \times 1\lambda$ surface than for a $2\lambda \times 2\lambda$ surface. This is due to the fact that for a high antenna density, the overall impact of the mutual coupling is greater compared to the lower density. There is a drastic increase in the mean Δ RCS from $1\lambda \times 1\lambda$ to $2\lambda \times 2\lambda$ distribution area and the coefficient of variance ($CV = \sigma/\mu$) is always higher for the higher antenna density. We chose to present data for two antenna densities in the reverse link as the mean is unlikely to vary significantly for the remaining lower antenna densities. Here, we intend to analyse the degradation of the differential RCS as a consequence of coupling compared to the isolated case and to predict the correlation and statistical similarities between the two types of antennas in terms of differential RCS. Figure 4.6 presents the CDF plots of the Δ RCS of dipoles and T-matched dipoles in dBm² for two distribution surface areas.

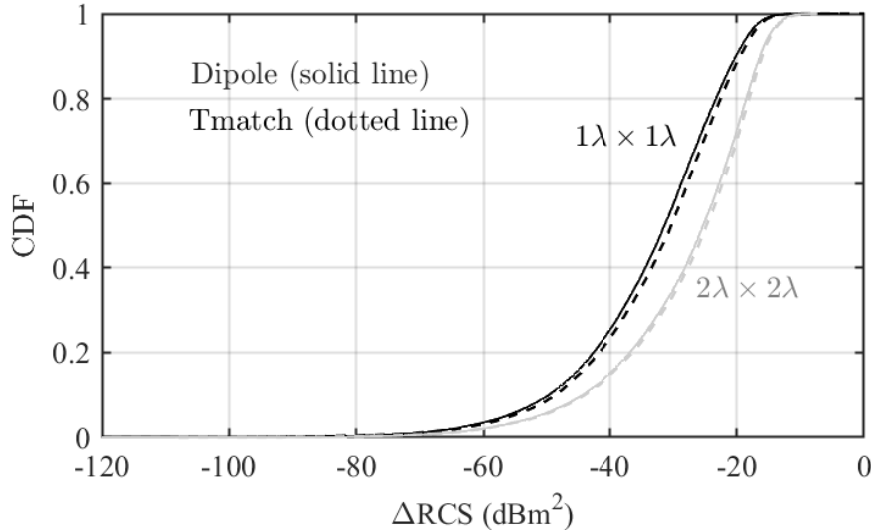


Figure 4.6: CDF plots for the differential RCS (ΔRCS) in dBm^2 of 2000 configurations of 10 randomly distributed dipoles without T-match (solid line) and with T-match (dotted line) over two distribution surface areas of $1\lambda \times 1\lambda$ (black line) and $2\lambda \times 2\lambda$ (grey line).

Table 4.8: Percentage of the dipole and T-matched dipoles with a differential RCS less than the threshold i.e. $\Delta\text{RCS} < -23\text{dBm}^2$.

Dipole	$1\lambda \times 1\lambda$	$2\lambda \times 2\lambda$
	81%	58%
T-match	$1\lambda \times 1\lambda$	$2\lambda \times 2\lambda$
	78%	56%

The international standard ISO/IEC 18000-6 [7] mentions that the differential RCS of tags affects the performance of the RFID system. A typical value should be greater than 0.005 m^2 (-23 dBm^2). According to this standard and according to the distribution function in Figure 4.6, the percentage of dipoles presenting a differential RCS greater than -23 dBm^2 , is equal to 19% for the largest dipole density ($1\lambda \times 1\lambda$) and it reaches 42% for the larger distribution surface ($2\lambda \times 2\lambda$). Consequently, the percentage of dipoles presenting a ΔRCS lower than the value recommended by the standard is equal to 81% for the small surface and 58% for the large one. A similar tendency is verified for T-matched dipoles. This conclusion quantifies the physical reality of electromagnetic coupling in terms of the observables of an RFID system. Indeed, when the proximity of tags in a high-density context creates strong electromagnetic coupling, the probability of the tag not being read increases. The statistical analysis of differential RCS is considered a key parameter of an RFID link. Therefore, in the long term, this study could give a reliable prediction of the performance of an RFID system in the context of high tag density.

4.3 Statistical analysis in the reverse link

It is interesting to combine the results obtained for the reverse link with those of the forward link in order to have a better insight over the whole RFID communication link. Consequently, we can observe among the tags activated during the forward link, which percentage satisfy also the constraints of the reverse link. For example, if the absorbed power by the isolated tag is estimated at the read range, the percentage of the coupled tags distributed over a $1\lambda \times 1\lambda$ surface and having $P_{L_{\text{norm}}} > 0$ dB is 16% as shown in Figure 4.5. The question would be which percentage of this population will show a satisfying ΔRCS with respect to the standard in the reverse link. Since we could not simulate real tags in the reverse link, we will use dipoles and T-matched dipoles instead to understand this relationship.

Referring to Table 4.5, the percentages of dipoles having $P_{L_{\text{norm}}} > 0$ dB with a linearly polarised plane wave are 14% for $1\lambda \times 1\lambda$ area and 38% for $2\lambda \times 2\lambda$ area. These percentages represent 2692 and 7687 of 20000 samples for the two densities respectively. After getting turned on, the ΔRCS of these samples are traced in Figure 4.7 to conclude on the percentage of dipoles satisfying the standard.

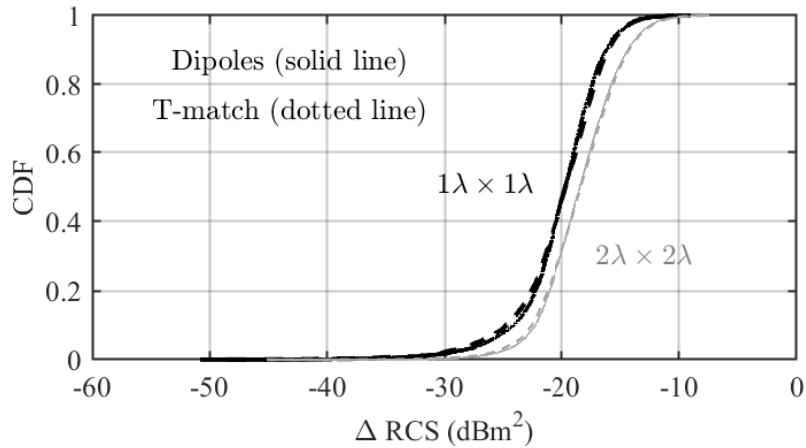


Figure 4.7: CDF plot for the ΔRCS in dBm^2 of samples (dipoles and T-matched dipoles) illuminated by a linearly polarised wave and having normalised absorbed power higher than 0 dB over a distribution of $1\lambda \times 1\lambda$ and $2\lambda \times 1\lambda$ area.

Table 4.9: Percentage of the dipole and T-matched dipoles having $P_{L_{\text{norm}}} > 0$ dB in the forward link, with a differential RCS greater than the standard value in the reverse link, i.e. $\Delta\text{RCS} > -23\text{dBm}^2$.

Dipole	$1\lambda \times 1\lambda$	$2\lambda \times 2\lambda$
	85%	93%
T-match	$1\lambda \times 1\lambda$	$2\lambda \times 2\lambda$
	83%	92%

From Table 4.9, we have found that 85% of the samples have $\Delta\sigma > -23 \text{ dBm}^2$ for

a $1\lambda \times 1\lambda$ distribution area and this percentage reached 93% for a $2\lambda \times 2\lambda$ area. This shows that among the number of dipoles activated in the forward link, a large number of dipoles would satisfy the standard in the reverse link. Due to coupling effects, the remaining samples show a smaller ΔRCS as per the standard value, although having received $P_{L_{\text{norm}}} > 0$ dB. The same tendency is valid for the T-matched dipoles. This combined information relating the normalised absorbed power and the differential RCS would help the RFID designer to assess the performance of the RFID link as a whole.

4.4 Conclusion

NEC and HFSS simulations were used to estimate the statistics concerning the impact of coupling on RFID forward and reverse links. The forward link is investigated by the chip absorbed power and the reverse link by the differential RCS. The results include dipoles, with and without T-match and real tags for both polarisations in the forward link while real tags and circular polarisation are not included in the reverse link. This study was carried out for 2000 configurations of antennas randomly distributed over different distribution surfaces. The statistics of the forward link allow us to draw conclusions regarding the percentage of the antennas that are powered up for a given antenna density. We observed that despite the fact of different intrinsic characteristics between dipoles, T-match dipoles and tags, their statistical behaviour on the turn-on power is similar. After being turned on, the tags respond to the reader with a backscattered modulated signal, the results obtained in terms of ΔRCS allow us to estimate the percentage of the antennas that present a satisfying ΔRCS with respect to standards.

4.4 Conclusion

,

Chapter 5

Conclusion and Perspectives

In the context of UHF RFID communication, the effective communication between RFID antennas can be compromised when strong coupling occurs. This coupling typically arises from the presence of a high density of RFID tags in close proximity, which leads to the RFID antennas encountering the turn-on power to wake up the tag and the associated backscattering in terms of RCS and Δ RCS. The primary aim of this thesis was to investigate the consequences of coupling on the inherent properties of antennas, particularly in scenarios where a significant quantity of RFID tags is densely concentrated within a confined space. The impact of polarisation of the incident plane wave on the antenna orientation, and antenna density considering the presence or absence of adjacent dipoles/tags, either enhances or suppresses coupling effects has been studied. Predicting the performance degradation resulting from antennas' position and orientation is challenging with a deterministic approach, particularly for a group of strongly coupled tags. Hence, a statistical evaluation becomes essential, especially when dealing with intricate scenarios. This study was carried out for several configurations of antennas randomly distributed over different distribution surfaces with loaded antennas, taking into account the effect of polarisation.

In Chapter 2, we presented three measurement setups for characterising RFID tags along with their associated RFID chips. The first setup entails measuring the wake-up power, impedance, and sensitivity of the isolated chip. The second setup is focused on determining the impedance of the isolated tag antenna. The third setup is designed to measure the read range of the isolated tag, which involves system-level measurements. For this characterisation procedure, we used the commercial ALN-996 tag and a homemade tag, each paired with their respective Higgs-3 and Higgs-9 chips. All the results obtained from these measurements were subsequently validated using HFSS. At the moment, these characterisation steps were important to further estimate the degradation in the read range of the tag of interest surrounded by other loaded tags. Following the comprehensive characterisation study, we turned our attention to

the development of a physical RFID model that incorporates the random distribution of RFID tags. To address the initial complexity of this modelling endeavour, we represented the RFID tags as a set of half-wave dipoles, both with and without T-matches. The reader in this model was substituted with a plane wave source. This approach not only simplifies the model but also makes it a cost-effective model. All the experimental and simulator tools we used further in the study have been discussed in this chapter.

The system-level measurements led us to extend our work on a circuit level with a simplified model of an RFID tag surrounded by other loaded tags as presented in Chapter 3. Here, we presented a conventional RFID network model with random tags and performed a comprehensive power budget analysis to understand our network model better. We used real commercial UHF RFID tags (ALN9662), and dipoles with and without T-match to analyse the impact of coupling due to the randomness of tags in a high-density context. We introduced two NEC-based models for the analysis. The first model employs a plane wave to excite a set of randomly distributed tags, while the second uses open circuit voltages derived from the plane wave illumination to stimulate the tags. We validated all our results using HFSS simulations. Here in simulations, the degradation is examined through a power budget analysis, involving four power levels estimated for a set of randomly distributed tags exposed to plane wave illumination. This is attributed to the coupling effects arising from various factors, including antenna randomness, antenna density, and plane wave polarisation. To focus on a critical aspect of the RFID forward link explicitly, we evaluate the absorbed power by the load. The observed statistical similarities between tags and dipoles presented by I. Adjali (former PhD student) are further investigated here in terms of normalised absorbed power associated with the forward link. The utilization of the normalized absorbed power methodology introduces an innovative method in assessing the performance of RFID systems. It enables us to accurately determine the percentage of active tags within a high-density context. In addition to the forward link analysis, we integrated the reverse link perspective by presenting the Radar Cross Section (RCS) of loaded scatterers with short-circuit and matched loads. We also verified the differential RCS to explain the backscattering phenomenon. Predicting the performance degradation resulting from antennas' position and orientation is challenging with a deterministic approach, especially in a high-density context and therefore a statistical study has been presented in Chapter 4. Here, we presented a statistical evaluation of coupling effects between tags in UHF RFID forward and reverse links.

The RFID forward link has been investigated statistically for four different densities of dipoles (with and without T-match) terminated on their matched loads employing linear and circular polarisations, and one density in the case of commercial tags

employing linear polarisation. The statistical results show a non-negligible influence of the coupling on the received power at the level of the chip. This technique allows the quantification of the percentage of tags that are not powered up in a given scenario. The impact of coupling is noticeable to a certain extent, and it diminishes as the tag density decreases. Combined with the reverse link, the statistical analysis of ΔRCS has been presented for two densities of dipoles and T-matched dipoles employing the linear polarisation of a plane wave. The statistical similarity between dipoles with and without a T-match network and the real tags, in relation to ΔRCS in the reverse link, could not be verified. Consequently, definitive conclusions cannot yet be drawn. Furthermore, despite extending the statistical study to UHF RFID tags, a complete comparison of the statistical behaviours among dipoles, T-matched dipoles, and RFID tags remains pending due to limited computing resources. Additional investigations are required to address unresolved hypotheses.

Short term perspective

- In this thesis simulations and measurements were conducted to assess the read range of an isolated tag. In the ongoing research, the immediate objective is to conduct a performance analysis to elucidate the degradation in read range measurements when assessing a particular tag of interest in the presence of proximate loaded tags. This inquiry will systematically consider the non-linear characteristics inherent in the chip's behaviour, as the chip impedance varies according to the incident power.
- The ΔRCS of the tag of interest, when it is surrounded by loaded tags, should also be estimated experimentally. The HFSS simulation setup needs to be modified/adapted to allow statistical investigations on the ΔRCS of real tags.
- The reverse link statistics should be more solidly combined to those of the forward link, to further enhance the understanding of both links. A total link budget of an RFID communication, from the reader to a tag as well as the tag to the reader, should be established.

Medium term perspective

- In this thesis, the statistical analysis has been exclusively conducted using electromagnetic simulators. The statistical similarity between real tags and dipoles encourages to further simplify the NEC-based model. Using thin dipoles, the absorbed power as well as the ΔRCS can be achieved analytically using the induced electromotive force (IEMF) method. This involves introducing a plane

wave excitation and determining the equivalent open circuit voltage. Leveraging the reduced computational time made possible by IEMF, a significant quantity of statistical samples can be efficiently generated and treated.

- In this thesis, for the sake of simplicity, the dipoles/tags are distributed on a 2D surface. It is worth noting that the statistical conclusions, e.g. related to the percentage of non-activated tags for a given density in the forward link, might change in a 3D scenario. The NEC-based model and HFSS simulations can easily be accommodated to cover 3D cases while the IEMF method can be extended using Euler angles [50].

Long term perspectives

- The long term vision involves the integration of variable parameters related to the immediate environment of RFID tags, starting with the electrical properties of the tagged objects. These environmental factors would include multi-path phenomena and may encompass parameters like temperature, humidity, and exposure to harsh environmental conditions, all of which have the potential to influence the system performances.
- The RFID infrastructure uncertainties, including the reader sensitivity in addition to the reader-to-tag distance, should be included in a system-based statistical analysis.
- A long-term research work may include benchmarking different types and natures of tag antennas with respect to their behaviour in presence of strong couplings. This step leads eventually to the development of an optimal antenna topology in a high density of tagged objects.

,

List of publications

The following are the papers based on this work, which were presented at national and international conferences and accepted journal articles.

□ National Conference with Proceedings:

1. J. Mudakkarappilli Sudersanan, A. Mughal, S. Mostarshedi, B. Poussot, J-M. Laheurte, "**Estimation de la surface équivalente radar d'un ensemble de dipôles aléatoirement répartis : application à la RFID – Partie I**", *22^{eme} Journées Nationales Microondes (JNM)*, Limoges, France, 7-10 Juin 2022.
2. A. Mughal, J. Mudakkarappilli Sudersanan, S. Mostarshedi, B. Poussot, J-M. Laheurte, "**Estimation de la surface équivalente radar d'un ensemble de dipôles aléatoirement répartis : application à la RFID – Partie II**", *22^{eme} Journées Nationales Microondes (JNM)*, Limoges, France, 7-10 Juin 2022.

□ International Conferences with Review Committee:

1. A. Mughal, J. Mudakkarappilli Sudersanan, S. Mostarshedi, B. Poussot, J-M. Laheurte, "**Backscattered field of a random set of dipoles as a model for highly coupled RFID tags**", *16th European Conference on Antennas and Propagation (EUCAP)*, Madrid, Spain, 27 March - 1 April 2022.
2. A. Mughal, J. Mudakkarappilli Sudersanan, S. Mostarshedi, B. Poussot, J-M. Laheurte, "**Radar Cross Section estimation of a set of randomly distributed dipoles as an application to RFID in a high density context**", *8th International Conference on Antennas and Electromagnetic Systems (AES)*, Marrakech, Morocco, 24 - 27 May 2022.
3. A. Mughal, S. Mostarshedi, B. Poussot, J-M. Laheurte, "**Introduction of statistics in the analysis of an RFID link in a high density context**", *12th Annual IEEE International Conference on RFID Technology and Applications (RFID-TA)*, Cagliari, Italy, 12 - 14 Sept 2022.

□ Journal Article:

1. A. Mughal, J. Mudakkarappilli Sudersanan, S. Mostarshedi, B. Poussot, J-M. Laheurte, "**Statistical evaluation of the coupling effects between tags in a UHF RFID forward link**", *IEEE Journal of Radio Frequency Identification*, Vol. 7, 2023.

Annex

A Derivation of absorbed power P_L and re-radiated power P_{in} in terms of reflection coefficient (Γ_{int})

This section is dedicated to the detailed derivations of power equations (3.8) and (3.13) in terms of reflection coefficient Γ_{int} defined by equation (3.9), which represents the mismatch between the load impedance (Z_L) and the input impedance of (Z_{in}) of the tag of interest (n) in the presence of the other loaded tags when illuminated by the plane wave.

A - 1 Absorbed power P_L in terms of Γ_{int}

The absorbed power (P_L) of a tag of interest (n) is expressed as follows,

$$P_{L_n} = \frac{1}{2} \left| \frac{V_n^{\text{OC}} - V_{\text{in}_n}^{\text{OC}}}{Z_{L_n} + Z_{\text{in}_n}} \right|^2 \Re(Z_{L_n}) \quad (\text{A1.1})$$

and reflection coefficient (Γ_{int_n}) is given as,

$$\Gamma_{\text{int}_n} = \frac{Z_{L_n} - Z_{\text{in}_n}^*}{Z_{L_n} + Z_{\text{in}_n}} \quad (\text{A1.2})$$

The derivation is given below,

$$1 - |\Gamma_{\text{int}_n}|^2 = 1 - \Gamma_{\text{int}_n} \Gamma_{\text{int}_n}^* \quad (\text{A1.3})$$

$$1 - |\Gamma_{\text{int}_n}|^2 = 1 - \left(\frac{Z_{L_n} - Z_{\text{in}_n}^*}{Z_{L_n} + Z_{\text{in}_n}} \right) \left(\frac{Z_{L_n} - Z_{\text{in}_n}^*}{Z_{L_n} + Z_{\text{in}_n}} \right)^* \quad (\text{A1.4})$$

$$1 - |\Gamma_{\text{int}_n}|^2 = 1 - \frac{(Z_{L_n} - Z_{\text{in}_n}^*)(Z_{L_n} - Z_{\text{in}_n}^*)^*}{(Z_{L_n} + Z_{\text{in}_n})(Z_{L_n} + Z_{\text{in}_n})^*} \quad (\text{A1.5})$$

$$1 - |\Gamma_{\text{int}_n}|^2 = \frac{(Z_{L_n} + Z_{\text{in}_n})(Z_{L_n} + Z_{\text{in}_n})^* - (Z_{L_n} - Z_{\text{in}_n}^*)(Z_{L_n} - Z_{\text{in}_n}^*)^*}{|Z_{L_n} + Z_{\text{in}_n}|^2} \quad (\text{A1.6})$$

After simplifying the numerator,

$$1 - |\Gamma_{\text{int}_n}|^2 = \frac{(Z_{\text{in}_n} + Z_{\text{in}_n}^*)(Z_{L_n} + Z_{L_n}^*)}{|Z_{L_n} + Z_{\text{in}_n}|^2} = \frac{4R_{\text{in}_n}R_{L_n}}{|Z_{L_n} + Z_{\text{in}_n}|^2} \quad (\text{A1.7})$$

Re-arranging equations (A1.7) as,

$$\frac{1 - |\Gamma_{\text{int}_n}|^2}{4R_{\text{in}_n}} = \frac{R_{L_n}}{|Z_{L_n} + Z_{\text{in}_n}|^2} \quad (\text{A1.8})$$

Hence, (A1.1) can also be expressed as,

$$P_{L_n} = \frac{|V_n^{\text{OC}} - V_{\text{in}_n}^{\text{OC}}|^2}{8R_{\text{in}_n}}(1 - |\Gamma_{\text{int}_n}|^2) \quad (\text{A1.9})$$

A - 2 Re-radiated power (P_{in}) in terms of reflection coefficient (Γ_{int})

The re-radiated power at the antenna level (P_{in}) of a tag of interest (n) is given as,

$$P_{\text{in}_n} = \frac{1}{2} \left| \frac{V_n^{\text{OC}} - V_{\text{in}_n}^{\text{OC}}}{Z_{L_n}^{\text{High/Low}} + Z_{\text{in}_n}} \right|^2 \Re(Z_{\text{in}_n}) \quad (\text{A2.1})$$

The derivation is given below,

$$|1 - \Gamma_{\text{int}_n}|^2 = \left| 1 - \frac{Z_{L_n} - Z_{\text{in}_n}^*}{Z_{L_n} + Z_{\text{in}_n}} \right|^2 \quad (\text{A2.2})$$

$$|1 - \Gamma_{\text{int}_n}|^2 = \left| \frac{(Z_{L_n} + Z_{\text{in}_n}) - (Z_{L_n} + Z_{\text{in}_n}^*)}{Z_{L_n} + Z_{\text{in}_n}} \right|^2 \quad (\text{A2.3})$$

After simplifying,

$$|1 - \Gamma_{\text{int}_n}|^2 = \left| \frac{Z_{\text{in}_n} + Z_{\text{in}_n}^*}{Z_{L_n} + Z_{\text{in}_n}} \right|^2 = \frac{4R_{\text{in}_n}^2}{|Z_{L_n} + Z_{\text{in}_n}|^2} \quad (\text{A2.4})$$

and

$$\frac{|1 - \Gamma_{\text{int}_n}|^2}{4R_{\text{in}_n}} = \frac{R_{\text{in}_n}}{|Z_{L_n} + Z_{\text{in}_n}|^2} \quad (\text{A2.5})$$

Now equation (A2.1) can also be expressed as,

$$P_{\text{in}_n} = \frac{|V_n^{\text{OC}} - V_{\text{in}_n}^{\text{OC}}|^2}{8R_{\text{in}_n}} |1 - \Gamma_{\text{int}_n}|^2 \quad (\text{A2.6})$$

where, Γ_{int_n} is obtained by $Z_{L_n}^{\text{High}}$ and $Z_{L_n}^{\text{Low}}$.

B Automation of simulation with NEC using MATLAB

B - 1 Presentation of 4NEC2 graphic interface

In this part, first, we will present the different windows found on the graphical interface of the software. When launching the software (4nec2.exe), two windows appear, shown in Figure B.1. The main window (Main: **F2**) is a window that allows access to several options and parameters, such as the editor, the 3D display. It also allows the launch of the simulation by clicking on the Run or F7 button and the display of certain simulation parameters related to the antenna such as: current, voltage, impedance, efficiency, etc. The second window (Geometry: **F3**), and is used to display the diagram of the wire antenna or the network of wire antennas showing working frequency.

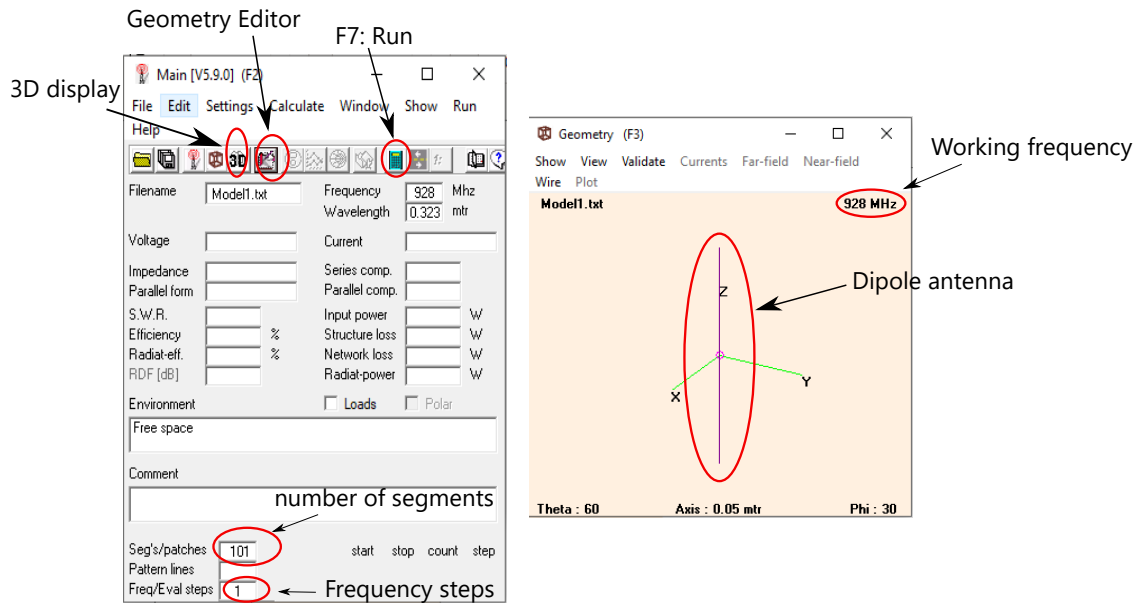


Figure B.1: Graphical interface of the 4NEC2 electromagnetic simulator

NEC Editors

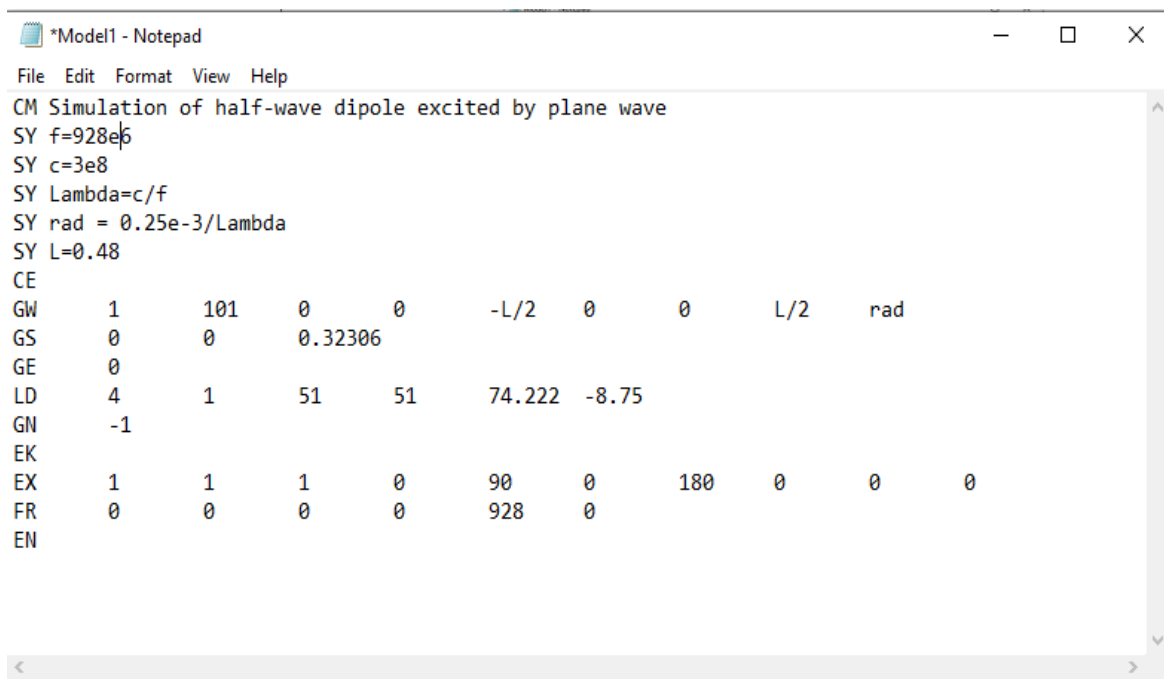
In order to integrate the parameters necessary for the design and simulation of antennas, it is important to know how to use the different NEC editors. To select the desired editor, simply go to the main window (Main: **F2**), go to settings and choose from the four editors offered by the manufacturer:

- Notepad editor (Ctrl+F1)
- NEC editor (old version) (Ctrl+F2)
- Geometry edit (Ctrl+F3)

- NEC editor (new version) (Ctrl+F4)

Notepad editor (Ctrl+F1)

By selecting the Notepad editor and clicking the editor icon on the main window (Main: **F2**), the window of Figure B.2 is displayed on the screen. Instructions at the beginning of the line make it possible to integrate the various parameters necessary for the design of the antenna and for the smooth running of the simulation.



```
*Model1 - Notepad
File Edit Format View Help
CM Simulation of half-wave dipole excited by plane wave
SY f=928e6
SY c=3e8
SY Lambda=c/f
SY rad = 0.25e-3/Lambda
SY L=0.48
CE
GW 1 101 0 0 -L/2 0 0 L/2 rad
GS 0 0 0.32306
GE 0
LD 4 1 51 51 74.222 -8.75
GN -1
EK
EX 1 1 1 0 90 0 180 0 0 0
FR 0 0 0 0 928 0
EN
```

Figure B.2: Notepad editor of 4NEC2

Line 1: "**CM**" Allows you to write comments

Line 2 to 6: "**SY**" (Symbol) is used to assign any value of antenna in terms of variables.

Line 7: "**CE**" (End of Comment) Indicates the end of the comments.

Line 8: "**GW**" (Geometry of wire), This line is dedicated to the geometry of wire antennas as follows:

"**1**" Corresponds to the wire antenna number.

"**101**" Indicates that the antenna is divided into 101 segments

"0,0,-L/2" Indicates the coordinates (xyz) of the end of the wire antenna

"0,0,L/2" Specifies the coordinates (xyz) of the other end of the wire antenna.

"rad" radius Radius of the antenna

Line 9: "GS" (Scale Structure Dimensions) This line is to scale all dimensions of a structure by a constant. Here in our case, the structure is scaled by lambda.

Line 10: "GE" (End of Geometry information) Command which puts an end to the information linked to the geometry of the antenna. This command is followed by a number "0" which indicates no ground is present, which means free space.

Line 11: "LD" (loading) To specify the impedance loading on one segment or a number of segments as follows:

"4" indicates type of load. Here it is impedance, input resistance and reactance in ohms.

"1" indicates wire number where you want to put load.

"51,51" indicates first and last segment of the wire antenna to assign load.

"74.222,-8.75" input resistance and reactance of load in ohms.

Line 12: "GN" (Ground parameters) This command nullifies ground parameters previously used and sets free-space condition in our case.

Line 13: "EK" (Extended Thin-Wire Kernel (EK)) Blank or zero to initiate use of the extended thin-wire kernel, -1 to return to standard thin-wire kernel. Without an EK card, the program will use the standard thin-wire kernel.

Line 14: "EX" (Excitation) Indicates the line dedicated to the excitation of the antenna.

"1" corresponds to the type of excitation used. In this case, the number 1 corresponds to a linear plane wave excitation.

"1" is the number of the θ plane angle of plane wave.

"1" is the number of the ϕ plane angle of plane wave.

"0" no action for maximum relative admittance matrix asymmetry for source segment and network connection.

"90,0,180" are the plane angle and polarization angles of plane wave in degrees as per following Figure B.3.

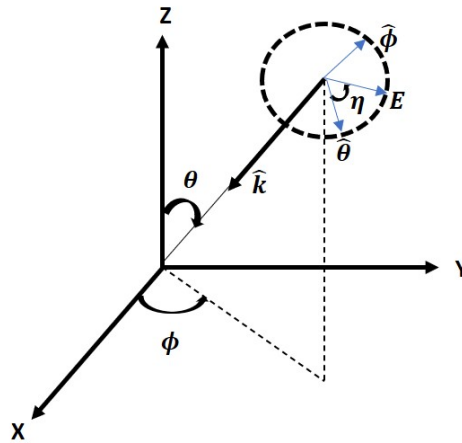


Figure B.3: Specifications of a plane wave

"0,0,0" are the θ and ϕ increment steps in degrees followed by the Rratio of minor axis to major axis for elliptic polarization (major axis field strength - 1 V/m).

Line 15: "FR" (Frequency) Indicates frequency-related information.

"0" Linear frequency sweep

"1" A single frequency step

"0,0" Two empty fields

"0" Empty field.

"928" Selected frequency.

Line 16: "EN" (End nec file) Indicates the end of the commands of the input file.

NEC Editor (old version) (Ctrl+F2)

By selecting the NEC editor (old version) and clicking the editor icon on the main window (Main: **F2**) or **F6**, the window in Figure B.4 is displayed on the screen.

This version is equivalent to the Notepad editor. The selection or the integration of a line is done in the dedicated frame. The user then fills in the fields with the desired variables. It is possible to launch the simulation without calling the window.

B - 1.1 Geometry Editor (Ctrl+F3)

By selecting the Geometry edit and clicking on the editor icon on the main window (Main: **F2**), the window of Figure B.5 is displayed on the screen.

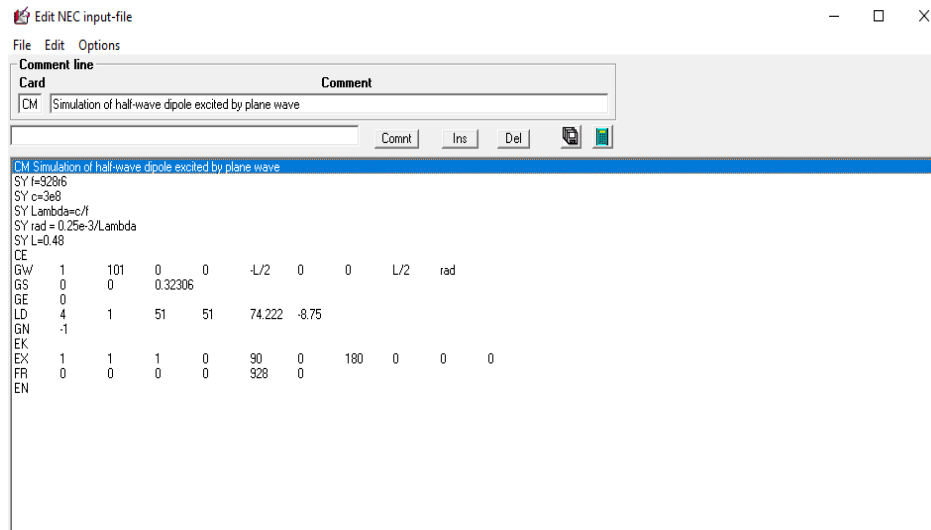


Figure B.4: Old version of 4NEC2 editor

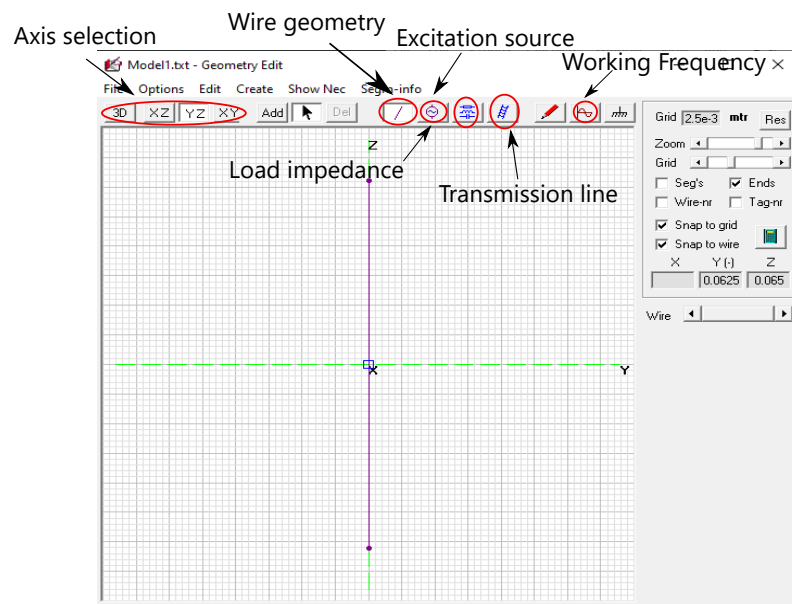


Figure B.5: Geometry editor of 4NEC2

This easy-to-use graphic editor is intended for beginners. Some antenna structures are already pre-registered such as patch, cylindrical, parabolic, helical antennas.

B - 1.2 NEC Editor (New Version) (Ctrl+F4)

By selecting the NEC editor (new version) and clicking on the editor icon on the main window (Main: **F2**), the window in Figure B.6 is displayed on the screen. Unlike the old version, each abbreviation is split across multiple tabs.

B Automation of simulation with NEC using MATLAB

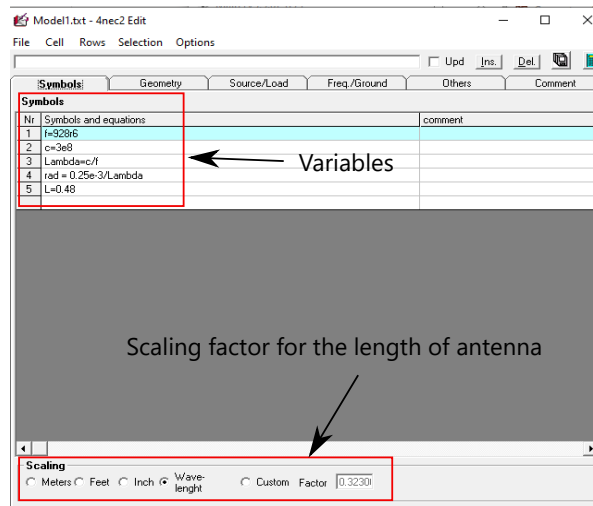


Figure B.6: Geometry editor of 4NEC2

-Symbols

The first tab (Figure B.6) is dedicated to the different variables or equations involved in the design of the antenna. Just integrate the variables under the "Symbols" column. You can also choose the scale in the "scaling" dial. Here we chose Lambda as mentioned before.

-Geometry

Under the Geometry tab (Figure B.7), we see one of the column allowing to create the type of metal and the geometry of the antenna.

"Type": This field offers different types of structures. In our work, we used the "wires" type. The columns of this table are as follows:

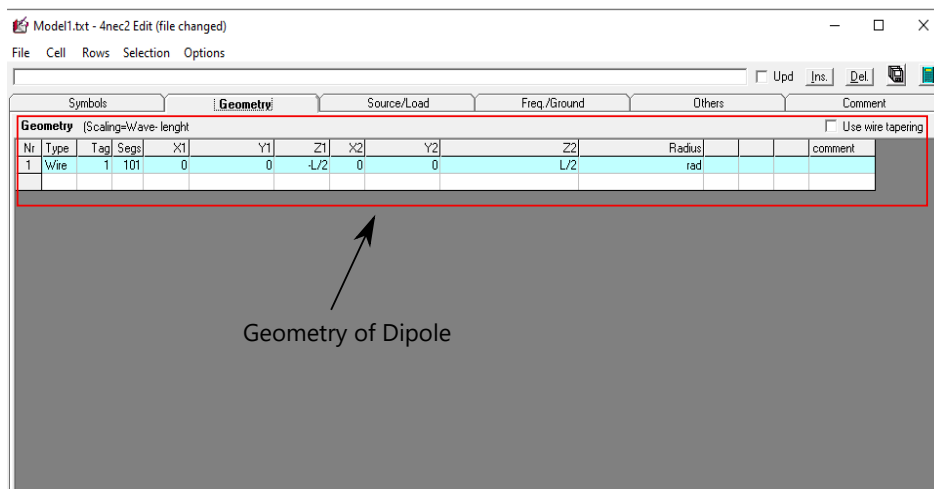


Figure B.7: Geometry editor of 4NEC2

"**Tag**": This field identifies the tag number (antenna) which will be used to assign a source or a load to the particular segment.

"**Segs**": This field defines the number of segments discretizing the antenna for the simulation. Accuracy increases with the number of segments which requires more computing resources.

"**X1, Y1, Z1**": These fields define the x, y and z coordinates of one end of the wire.

"**X2, Y2, Z2**": These fields define the x, y and z coordinates of the other end of the wire.

"**Radius**": This field defines the radius of the wire in meters.

- Source/Load

Antenna excitation Under the "Source/Load" tab (Figure B.8), the various columns allow you to configure the source, the load or a transmission line. The different columns are exactly same as defined in notepad editor.

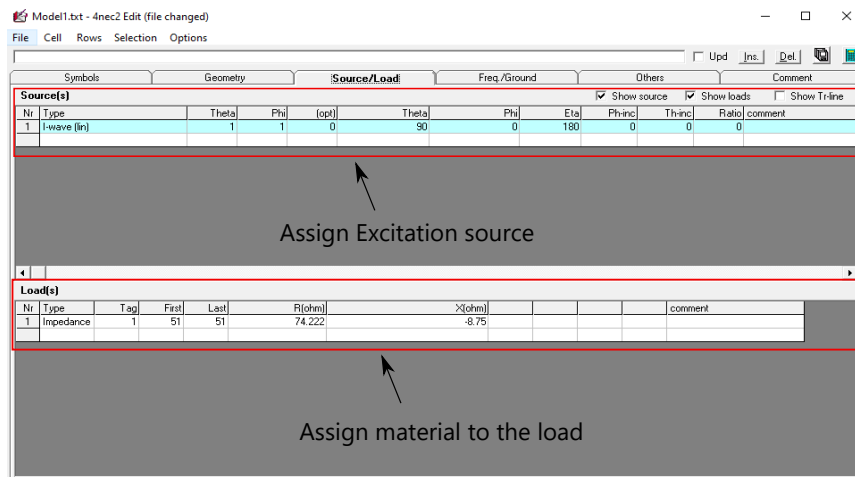


Figure B.8: Geometry editor of 4NEC2

-Frequency and Environment

the (Freq/Ground) tab, there are two options (Figure B.9), one allows you to specify information related to the frequency, For us it is 928MHz frequency. The second dial allows you to choose the environment around the antenna. In this example, we have chosen a free-space simulation.

-Generate Data

The simulation can be launched by pressing F7, or by clicking on the "Run" icon located on the main window. There are several options (Figure B.10) to generate the impedance or near-field or far-field radiation of antenna.

B Automation of simulation with NEC using MATLAB

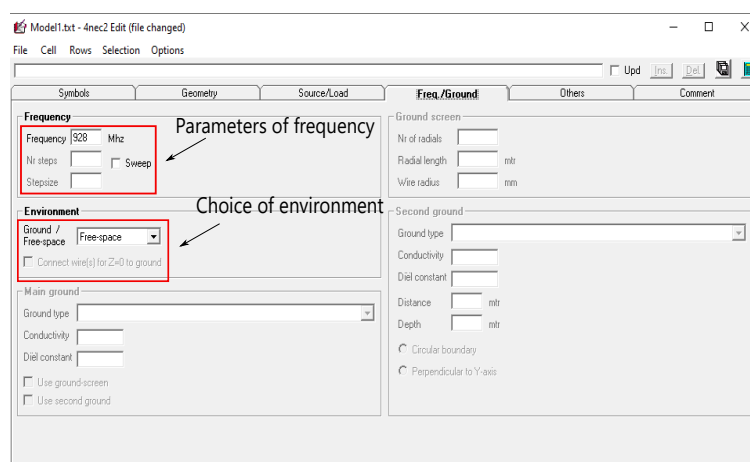


Figure B.9: Geometry editor of 4NEC2

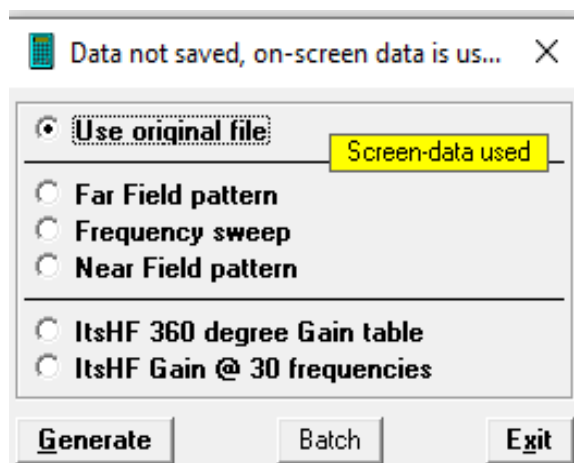


Figure B.10: Geometry editor of 4NEC2

"Use original file": Generates the antenna impedance, current and voltage.

"Far Field pattern": Generates only the radiation from the antenna in the far field.

"Frequency sweep": Generates the antenna input impedance on a frequency band.

"Near Field pattern": Generates radiation from the antenna in the near field only.

Obtained Load current from output file

NEC only calculates input current in the case of plane wave excitation. After assigning linearly or circularly polarised wave for the desired polarization and plane angle of incident field as explained in Section B - 1, the input current would be calculated in the center segment of wire antennas. Because of the sinusoidal current distribution, current would be maximum at its center segment.

C Automation of simulation with HFSS using MATLAB:

The study of monostatic RCS of commercial tags presented in chapter 2 was carried out using HFSS simulations. To carry out a statistical study with commercial tags, it was important to find a solution to automate HFSS simulations. In this section, the automated procedure for launching HFSS simulation using MATLAB is presented. First, a script containing all the parameters and instructions necessary for the simulation was created. The script is read and generated by HFSS are programmed either with Python or VBs (Visual Basic script). Here, we have opted VBs for the coding of the scripts from the MATLAB interface in C language. Following are the detailed step by step instructions of the HFSS script coded in VBs for a simulation of a tag.

The first step is to declare the different libraries and packages used during the simulation and to create and rename the HFSS projects with a ".aedt" extension as shown in the Figure C.1.

```

' -----
' Script Recorded by Ansys Electronics Desktop Version 2021.2.0
' 12:38:49 févr. 08, 2022
' -----
Dim oAnsoftApp
Dim oDesktop
Dim oProject
Dim oDesign
Dim oEditor
Dim oModule
Set oAnsoftApp = CreateObject("Ansoft.ElectronicsDesktop")
Set oDesktop = oAnsoftApp.GetAppDesktop()
oDesktop.RestoreWindow
Set oProject = oDesktop.NewProject
oProject.InsertDesign "HFSS", "HFSSDesign1", "HFSS Modal Network", ""
oProject.Rename "C:/Users/mughal/Documents/Ansoft/HFSS_SCRIPT_configuration1.aedt", true
Set oDesign = oProject.SetActiveDesign("HFSSDesign1")
oDesign.RenameDesignInstance "HFSSDesign1", "HFSS_SCRIPT_antenne_1"

```

} Package declaration

} Creation of HFSS project (.aedt)

Figure C.1: Declaration of packages and creation of HFSS projects from the script

The second step is to declare all the local variables used during the simulation such as the positions of the centers of the tags as well as their angles of inclination, the dimensions of the air box, the wavelength, etc. Figure C.2 shows a few parameters of a tag as an example of how to assign a local variable.

```

oDesign.ChangeProperty Array("NAME:AllTabs",
Array("NAME:LocalVariableTab"), ← assign variable to parameters
Array("NAME:PropServers", "LocalVariables"),
Array("NAME:NewProps",
Array("NAME:Angle1", "PropType=", "VariableProp", "UserDef=", true, "Value=", "-15.326475826deg" ),
Array("NAME:MoveX1", "PropType=", "VariableProp", "UserDef=", true, "Value=", "2.540496e+02mm" ),
Array("NAME:MoveY1", "PropType=", "VariableProp", "UserDef=", true, "Value=", "1.489451e+02mm" ),
parameters (angle & orientation)

```

Figure C.2: Declaration of local variables on the HFSS script

The third step is to create and edit the air box in which the RFID tags will be placed as shown in Figure C.3. By setting the correct positioning and the correct size of the air box, the calculation time is optimized with excellent precision.

```

Set oEditor = oDesign.SetActiveEditor("3D Modeler")
oEditor.CreateBox Array("NAME:BoxParameters", "XPosition=", "-Lbx/2", "YPosition=", _
"-Lby/2+Air_PosY", "ZPosition=", "-Lbz/2+Air_PosZ", "XSize=", "Lbx", "YSize=", "Lby", "ZSize=", _
"Lbz"), Array("NAME:Attributes", "Name=", "Box1", "Flags=", "", "Color=", _
"(255 255 255)", "Transparency=", 1, "PartCoordinateSystem=", "Global", "UDMId=", _
"", "MaterialValue=", "" & Chr(34) & "vacuum" & Chr(34) & "", "SolveInside=", _
true)

```

Figure C.3: Creation of boundary box

The two very important input parameters are to assign complex load impedance to the tags and apply excitation to the tag model. In HFSS, the complex load impedance is decomposed into series/parallel RLC components and assigned as (**RLC Type: parallel**) as shown in Figure C.4 with the assigned values of resistance, inductance, and capacitance. Next is to give excitation to our model and we chose incident plane wave with the direction given in spherical coordinates as shown in Figure C.4.

The last instruction consists firstly in integrating the simulation parameters, such as the frequency, the minimum and the maximum number of convergent passes, the convergence criterion, etc. Then to launch the simulation and export the simulation results in a given directory (see Figures C.5 and C.6).

```

Set oModule = oDesign.GetModule("BoundarySetup")
oModule.AssignLumpedRLC Array("NAME:LumpRLC1", "Objects:=", Array("Rectangle1"), Array("NAME:CurrentLine", "Coordinate System:=", _
"Global", "Start:=", Array("0.00999999999999987mm", "2.6mm", "-0.5mm"), "End:=", Array(
"0.01mm", "2.6mm", "0.5mm")), "RLC Type:=", "Parallel", "UseResist:=", true, "Resistance:=", _
"0ohm", "UseInduct:=", false, "UseCap:=", true, "Capacitance:=", "0pF")
oModule.AssignPlaneWave Array("NAME:IncPWave1", "IsCartesian:=", false, "PhiStart:=", _
"90deg", "PhiStop:=", "90deg", "PhiPoints:=", 1, "ThetaStart:=", "0deg", "ThetaStop:=", _
"360deg", "ThetaPoints:=", 73, "EoPhi:=", "0", "EoTheta:=", "-1", "OriginX:=", _
"0mm", "OriginY:=", "0mm", "OriginZ:=", "0mm", "IsPropagating:=", true, "IsEvanescent:=", _
false, "IsEllipticallyPolarized:=", false)

```

Assigning RLC port

Assigning incident plane wave

RLC type: Series /Parallel

Value of capacitance (variable)

Value of resistance (variable)

E field vector definition

Figure C.4: Specifications used to assign RLC port and plane wave excitation

```

Set oModule = oDesign.GetModule("AnalysisSetup")
oModule.InsertSetup "HfssDriven", Array("NAME:Setup1", "SolveType:=", "Single", "Frequency:=", _
"866MHz", "MaxDeltaE:=", 0.01, "MaximumPasses:=", 30, "MinimumPasses:=", 10, "MinimumConvergedPasses:=", _
3, "PercentRefinement:=", 30, "IsEnabled:=", true, Array("NAME:MeshLink", "ImportMesh:=", _

```

Figure C.5: Simulation parameters

```

oProject.Save
oDesign.AnalyzeAll
Set oModule = oDesign.GetModule("ReportSetup")
oModule.CreateReport "Monostatic RCS Table 1", "Monostatic RCS", "Data Table", _
"Setup1 : LastAdaptive", Array(), Array("IWaveTheta:=", Array("All"), "IWavePhi:=", Array( _
"90deg"), "Freq:=", Array("0.866GHz"), "segment:=", Array("Nominal")), Array("X Component:=", _
"IWaveTheta", "Y Component:=", Array("abs(MonostaticRCSTotal)"))
oModule.ExportToFile "Monostatic RCS Table 1", _
"C:/Users/mughal/Documents/Ansoft/Monostatic RCS Table 1.csv", false

```

Direction of interest to find RCS

Extract RCS data

Figure C.6: Launching the HFSS simulation and exporting the results from the script

This process must be repeated for each configuration. Once the script is finished, just launch from MATLAB the generated file in VBs format, using the MATLAB command "dos" or "system".

D Near-field of dipole using NEC

In this section, antenna radiation pattern is generated numerically by considering cartesian and spherical coordinates. The unit vectors of cartesian and spherical coordinates are $[c] = [x, y, z]^T$ and $[s] = [r, \theta, \phi]^T$ respectively where T denotes the

D Near-field of dipole using NEC

transpose of the vector. The two coordinate systems are shown in figure D.1. A vector field \mathbf{E} can be expressed by its cartesian components as $[E^c] = [E^x, E^y, E^z]^T = [|E^x|e^{j\varphi}, |E^y|e^{j\varphi}, |E^z|e^{j\varphi}]$ where $|E^x|, |E^y|, |E^z|$ and $e^{j\varphi}$ are the magnitudes in Volts/m and phase of each component of \mathbf{E} respectively.

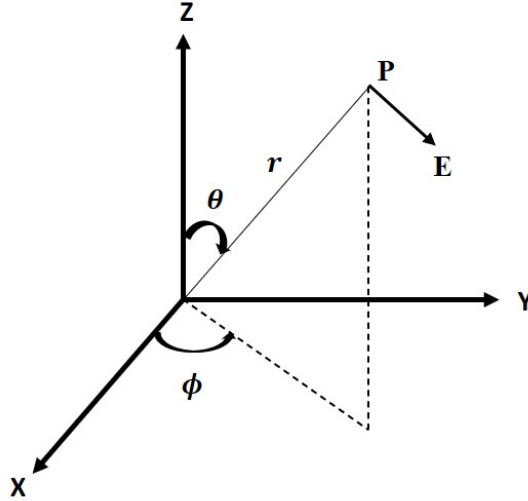


Figure D.1: Cartesian and spherical coordinates at point P

The NEC output file gives the vector components of radiated near field \mathbf{E} in cartesian coordinates system $[E^c]$ which could be transformed into spherical coordinates system $[E^s]$ using transformation matrix equations. Pre-defined input parameters to obtain \mathbf{E} in NEC simulator require only the spherical components $[s]$ of position vector at point \mathbf{P} as shown in figure D.2. In which **nr-R**, **nr-phi**, and **nr-theta** are the number of points required in $r, \phi(\phi), \theta(\theta)$ with their directions assign to **first R**, **first Phi** and **first The** respectively. **R-step**, **The-step** and **Phi-step** are the step sizes required for the calculation of number of points in their respective directions.

Near elec-field (spheric)

Card

NE : Near electric field

Type

.Near elec-field (spheric)

nr-R	nr-Phi	nr-The	first R	first Phi	first THE	R-step	The-step	Phi-step

Figure D.2: Input parameters for radiated near electric field using NEC

The transformation matrix from cartesian to spherical $[C_{toS}]$ is defined as

$$[C_{toS}] = \begin{bmatrix} \sin\theta\cos\phi & \sin\theta\sin\phi & \cos\theta \\ \cos\theta\cos\phi & \cos\theta\sin\phi & -\sin\theta \\ -\sin\phi & \cos\phi & 0 \end{bmatrix} \quad (\text{A2.7})$$

where θ and ϕ of equation (A2.7) are the spherical components of position vector at point P given as $\theta = \cos^{-1}(z/r)$ and $\phi = \tan^{-1}(y/x)$ and r is the amplitude calculated from the cartesian coordinates (x,y,z) of position vector. The transformation of a vector field \mathbf{E} from cartesian to spherical coordinates and vice versa could be done using equations (A2.8) and (A2.9) respectively.

$$E^s = [C_{toS}].[E^c] \quad (\text{A2.8})$$

$$E^c = [C_{toS}]^T.[E^s] \quad (\text{A2.9})$$

One can easily determine the antenna radiation pattern of a driven dipole in spherical vector components using equation (A2.8) for any observation point P from NEC output file.

Bibliography

- [1] H. Stockman, “Communication by Means of Reflected power,” *Proceedings of the IRE*, vol. 36, no. 10, pp. 1196–1204, Oct 1948.
- [2] F. Vernon, “Application of The Microwave Homodyne,” *Transactions of the IRE Professional Group on Antennas and Propagation*, vol. PGAP-4, pp. 110–116, December 1952.
- [3] D. B. Harris, “Radio Transmission Systems With modulatable Passive Responder,” no. 2927321, March 1960. [Online]. Available: <http://www.freepatentsonline.com/2927321.html>
- [4] R. F. Harrington, “Theory of loaded scatterers,” in *Proceedings of the institution of electrical engineers*, vol. 111, no. 4. IET, 1964, pp. 617–623.
- [5] S. A. Ahson and M. Ilyas, *RFID handbook: Applications, Technology, Security, and Privacy*. CRC press, 2017.
- [6] “EPC Radio-Frequency Identity Protocols Generation-2 UHF RFID Standard,” 2018, Specification for RFID Air Interface Protocol for Communications at 860 MHz – 960 MHz.
- [7] “Standard ISO/IEC 18000-6:2013,” 2013, Information Technology— Radio Frequency Identification for item management — Part 6: Parameters for air interface communications at 860 MHz to 960 MHz General.
- [8] X. Jia, Q. Feng, and C. Ma, “An Efficient Anti-Collision Protocol for RFID Tag Identification,” *IEEE Communications Letters*, vol. 14, no. 11, pp. 1014–1016, 2010.
- [9] R. Want, “An introduction to RFID technology,” *IEEE Pervasive Computing*, vol. 5, no. 1, pp. 25–33, 2006.
- [10] M. Bagherzadeh, M. Inamura, and H. Jeong, “Food Waste Along The Food Chain,” *OECD Food, Agriculture and Fisheries Papers No. 71*, 2014.

- [11] M. Beqqal and M. Azizi, “Review on security issues in RFID systems,” *Advances in Science, Technology and Engineering Systems Journal*, vol. 2, pp. 194–202, 12 2017.
- [12] H.-J. Li, H.-H. Lin, and H.-H. Wu, “Effect of antenna mutual coupling on the uhf passive rfid tag detection,” in *2008 IEEE Antennas and Propagation Society International Symposium*. IEEE, 2008, pp. 1–4.
- [13] M. Škiljo, P. Šolić, Z. Blažević, L. D. Rodić, and T. Perković, “Uhf rfid: Retail store performance,” *IEEE Journal of Radio Frequency Identification*, vol. 6, pp. 481–489, 2021.
- [14] G. Marrocco, “RFID Grids: Part I Electromagnetic Theory,” *IEEE Transactions on Antennas and Propagation*, vol. 59, no. 3, pp. 1019–1026, March 2011.
- [15] G. Marrocco and S. Caizzone, “Multi-chip RFID grids,” in *2011 IEEE International Symposium on Antennas and Propagation (APSURSI)*, 2011, pp. 1085–1088.
- [16] J. Mautz and R. Harrington, “Modal Analysis of Loaded N-port Scatterers,” *IEEE Transactions on Antennas and Propagation*, vol. 21, no. 2, pp. 188–199, March 1973.
- [17] S. Caizzone and G. Marrocco, “RFID Grids: Part II—Experimentations,” *IEEE Transactions on Antennas and Propagation*, vol. 59, no. 8, pp. 2896–2904, 2011.
- [18] I. Adjali, “Approche statistique pour la quantification des performances d’antennes fortement couplées: application à la rfid dans le contexte d’une densité élevée de tags,” Ph.D. dissertation, Paris Est, 2020.
- [19] H. Baker and A. LaGrone, “Digital computation of the mutual inductance between thin dipoles,” *IRE Transactions on Antennas and Propagation*, vol. 10, no. 2, pp. 172–178, 1962.
- [20] I. Adjali, A. Gueye, S. Mostarshedi, B. Poussot, F. Nadal, and J.-M. Laheurte, “Matching Evaluation of Highly Coupled Dipoles Quantified by a Statistical Approach,” *IEEE Transactions on Antennas and Propagation*, vol. 68, no. 7, pp. 5044–5051, 2020.
- [21] L. Wang, B. Norman, and J. Rajgopal, “Placement of multiple RFID reader antennas to maximize portal read accuracy,” *IJRFITA*, vol. 1, pp. 260–277, 01 2007.
- [22] S. Ebrahimi-Asl, M. T. A. Ghasr, and M. J. Zawodniok, “A solution to low read rate problem in RFID scattering networks,” *IEEE Journal of Radio Frequency Identification*, vol. 1, no. 2, pp. 176–184, 2017.

BIBLIOGRAPHY

- [23] S. Ebrahimi-Asl, M. T. A. Ghasr, and M. Zawodniok, “Cooperative interference control in neighboring passive scattering antennas,” *IEEE Journal of Radio Frequency Identification*, vol. 2, no. 3, pp. 152–158, 2018.
- [24] J. R. Kruest and G. Bann, “Systems and methods for stirring electromagnetic fields and interrogating stationary RFID tags,” Patent 07, 2011-07-07.
- [25] M. Balog, E. Szilagy, D. Duplakova, and M. Mindaš, “Effect verification of external factor to readability of RFID transponder using least square method,” *Measurement*, vol. 94, pp. 233–238, 2016.
- [26] J. Bolton, E. Jones, R. K. Punugu, A. Addy, and S. Okate, “Performance and benchmarking of multisurface UHF RFID tags for readability and reliability,” *Journal of Sensors*, vol. 2017, 2017.
- [27] R. Durgamcherur and E. C. Erick Jones, “Statistical analysis on readability of RFID Gen2 passive tags using Bayesian information criterion and 2-level factorial design,” *Int. Supply Chain Technol. J.*, vol. 06, no. 11, Nov. 2020.
- [28] G. Aryal, L. Mapa, and S. K. Camsarapalli, “Effect of variables and their interactions on RFID tag readability on a conveyor belt—Factorial analysis approach,” in *2010 IEEE International Conference on Electro/Information Technology*. IEEE, 2010, pp. 1–6.
- [29] R. Y. Rubinstein and D. P. Kroese, *Simulation and the Monte Carlo method*. John Wiley & Sons, 2016.
- [30] B. Sudret, “Meta-models for structural reliability and uncertainty quantification,” *arXiv preprint arXiv:1203.2062*, 2012.
- [31] *ALN-9662 Short Inlay*, Alien Technology, 2014. [Online]. Available: <http://www.alientechnology.com/wp-content/uploads/Alien-Technology-Higgs-3-ALN-9662-Short.pdf>
- [32] *Higgs 3, EPC Class 1 Gen 2 RFID Tag IC*, Alien Technology, 2020. [Online]. Available: <https://www.alientechnology.com/products/ic/higgs-3>
- [33] “RFID Measurement Cabinets,” <https://voyantic.com/products/tagformance-pro/accessories/rfid-measurement-cabinet>, accessed: 2019-11-1.
- [34] K. D. Palmer and M. W. van Rooyen, “Simple broadband measurements of balanced loads using a network analyzer,” *IEEE transactions on instrumentation and measurement*, vol. 55, no. 1, pp. 266–272, 2006.
- [35] G. J. Burke and A. J. Poggio, “Numerical Electromagnetics Code (NEC)-Method of Moments,” 1981.

- [36] Z. Cendes, “The development of hfss,” in *2016 USNC-URSI Radio Science Meeting*, 2016, pp. 39–40.
- [37] P. V. Nikitin, K. V. S. Rao, R. Martinez, and S. F. Lam, “Sensitivity and Impedance measurements of UHF RFID chips,” *IEEE Transactions on Microwave Theory and Techniques*, vol. 57, no. 5, pp. 1297–1302, 2009.
- [38] *Higgs 9, EPC Class 1 Gen 2 RFID Tag IC*, Alien Technology, 2020. [Online]. Available: <https://www.alientechnology.com/products/ic/higgs-9/>
- [39] L. Catarinucci, D. De Donno, R. Colella, F. Ricciato, and L. Tarricone, “A cost-effective SDR platform for performance characterization of RFID tags,” *IEEE Transactions on Instrumentation and Measurement*, vol. 61, no. 4, pp. 903–911, 2011.
- [40] C. A. Balanis, *Antenna Theory: Analysis and Design*. Wiley-Interscience, 2005.
- [41] F. Gourari, S. Meriah, S. Protat, J. Dubouil, and J.-M. Laheurte, “Comparison of two matching techniques for UHF RFID tags,” *Microwave and Optical Technology Letters*, vol. 60, no. 7, pp. 1763–1767, 2018.
- [42] P. Nikitin, K. Rao, and R. Martinez, “Differential RCS of RFID tag,” *Electronics Letters*, vol. 43, pp. 431 – 432, 02 2007.
- [43] A. E. Fuhs, *Radar cross section lectures*. Monterey, California, Naval Postgraduate School, 1982.
- [44] K. Penttilä, M. Keskilammi, L. Sydänheimo, and M. Kivikoski, “Radar cross-section analysis for passive RFID systems,” *IEE Proceedings-Microwaves, Antennas and Propagation*, vol. 153, no. 1, pp. 103–109, 2006.
- [45] P. Nikitin and K. Rao, “Theory and measurement of backscattering from RFID tags,” *Antennas and Propagation Magazine, IEEE*, vol. 48, pp. 212 – 218, 01 2007.
- [46] S. Ebrahimi, M. Ghasr, and M. Zawodniok, “A solution to low read rate problem in rfid scattering networks,” *IEEE Journal of Radio Frequency Identification*, vol. PP, pp. 1–1, 11 2017.
- [47] R. C. Hansen, “Relationships between antennas as scatterers and as radiators,” *Proceedings of the IEEE*, vol. 77, no. 5, pp. 659–662, 1989.
- [48] R. B. Green, *The general theory of antenna scattering*. The Ohio State University, 1963.
- [49] N. Barbot, O. Rance, and E. Perret, “Differential RCS of Modulated Tag,” *IEEE Transactions on Antennas and Propagation*, vol. 69, no. 9, pp. 6128–6133, 2021.

BIBLIOGRAPHY

- [50] Y. Rahmat-Samii, "Useful coordinate transformations for antenna applications," *IEEE Transactions on Antennas and Propagation*, vol. 27, no. 4, pp. 571–574, 1979.

Résumé

Le contexte de cette thèse était de proposer un modèle physique d'un système RFID pour quantifier les effets du couplage dans les deux liens RFID dans un contexte de haute densité. Un couplage électromagnétique significatif se produit généralement en raison de la présence de plusieurs étiquettes à proximité, ce qui conduit les antennes RFID à rencontrer la puissance d'allumage pour réveiller l'étiquette dans la liaison avant et la rétrodiffusion associée en termes de SER et Δ SER dans la liaison arrière. L'objectif principal était d'évaluer comment le couplage affecte les caractéristiques inhérentes des antennes, en particulier dans les scénarios où une quantité importante d'étiquettes RFID est densément concentrée dans un volume réduit. L'étude a examiné l'impact de la polarisation des ondes planes incidentes sur l'orientation et la densité de l'antenne, en tenant compte de la présence ou de l'absence d'étiquettes adjacentes. Il a été observé que les effets de couplage peuvent être renforcés ou supprimés en fonction de la polarisation et du caractère aléatoire des étiquettes. La prévision de la dégradation des performances causée par la position et l'orientation de l'antenne est difficile à réaliser à l'aide d'une approche déterministe, en particulier dans les scénarios impliquant un ensemble d'étiquettes fortement couplées. C'est pourquoi une évaluation statistique devient cruciale, en particulier dans les situations complexes. La recherche a porté sur diverses configurations d'antennes réparties de manière aléatoire sur différentes surfaces, avec des antennes chargées, tout en tenant compte de l'impact de la polarisation.

Le chapitre 2 a commencé par un modèle de communication entre une seule étiquette et un lecteur. Dans un premier temps, nous avons examiné le comportement d'une seule étiquette sans tenir compte de l'interaction avec d'autres (pas de couplage). Pour atteindre cet objectif, nous avons introduit trois dispositifs de mesure pour caractériser l'antenne de l'étiquette RFID et la puce RFID qui lui est associée. L'étude a porté sur deux types d'étiquettes : l'étiquette commerciale ALN-9662 conçue par la société de technologie Alien pour être conjuguée à la puce Higgs-3 et une étiquette artisanale conçue par mon collègue J. Mudakkarappilli Sudersanan et fabriquée par notre équipe de recherche pour être conjuguée à la puce Higgs-9. Le premier dispositif de mesure comprend l'analyseur d'impédance pour mesurer l'impédance de la puce (Z_{chip})

Résumé

et le système Voyantic Tagformance pour déterminer la puissance minimale d'allumage (P_{min}) au niveau du réveil de la puce pour une fréquence de travail donnée. Le comportement non linéaire de la puce a été observé en mesurant l'impédance de la puce à l'aide de l'analyseur d'impédance en fonction de P_{min} pour différentes fréquences. Dans cette thèse, nous avons choisi de travailler sur une fréquence de 928 MHz, et la puissance minimale d'allumage, P_{min} , à cette fréquence, a été mesurée à l'aide du système Voyantic Tagformance. Comme indiqué, deux puces RFID sont utilisées dans l'étude et -7,2 dBm et -9,2 dBm sont les puissances d'activation minimales mesurées des deux puces, Higgs-3 et Higgs-9, au niveau de réveil respectivement. À l'aide d'un analyseur d'impédance, les valeurs Z_{chip} de deux puces ont été mesurées à une fréquence de 928 MHz, avec les P_{min} correspondants. Nos résultats ont révélé que l'impédance de la puce de Higgs-3 varie d'un échantillon à l'autre, ce qui peut être attribué à l'emballage mince de la puce ou à sa nature délicate, nécessitant une manipulation soignée pour obtenir des résultats de mesure cohérents dans tous les échantillons. En revanche, dans le cas de Higgs-9, les résultats de l'impédance sont cohérents d'une puce à l'autre. Cette uniformité des résultats valide non seulement notre dispositif expérimental, mais souligne également la robustesse et la précision des mesures. Par conséquent, Higgs-9 est choisi non seulement pour la cohérence de ses résultats de mesure, mais aussi pour servir de moyen de validation de notre dispositif, un aspect qui ne pouvait pas être déterminé de manière concluante avec Higgs-3 seul.

Le second dispositif expérimental a été utilisé pour caractériser l'étiquette ALN-9662 et une étiquette artisanale sans les puces associées. L'impédance d'entrée complexe (Z_a) de l'antenne du tag est mesurée avec un analyseur de réseau vectoriel (VNA) utilisant une technique d'excitation différentielle. L'impédance d'entrée de l'antenne en fonction des paramètres S est obtenue en utilisant les équations courant-tension liées à la matrice d'impédance des deux câbles à l'aide du VNA. Ensuite, à partir de la matrice S différentielle, nous obtenons le S11 qui est ensuite utilisé pour calculer l'impédance d'entrée de l'antenne. Il a été observé que l'impédance mesurée de l'antenne tag correspondait à l'impédance d'entrée simulée obtenue par HFSS. L'adaptation conjuguée de l'étiquette ALN-9662 et d'une étiquette artisanale avec leurs puces associées est observée à 928 MHz et 862 MHz respectivement. Le processus de caractérisation est ensuite suivi par la mesure des observables au niveau du système à l'aide du troisième dispositif expérimental qui comprend le système Voyantic Tagformance et l'étiquette RFID qui incorpore à la fois l'antenne et la puce placées à l'intérieur de l'armoire Voyantic dans un dispositif sans fil. Le système Voyantic Tagformance est utilisé pour évaluer la fonctionnalité des étiquettes RFID dans les deux liaisons RFID. Parmi les paramètres clés disponibles pour la liaison aller, la portée de lecture est le seul paramètre qui permette une évaluation complète de l'étiquette au niveau du système.

Par conséquent, nous avons choisi de mesurer la portée de lecture pour quelques échantillons d'étiquettes isolées. Nous avons également développé une équation analytique pour estimer la portée de lecture à l'aide de paramètres obtenus à partir de mesures ou de simulations dans HFSS. Trois échantillons d'étiquettes ALN-9962 et d'étiquettes artisanales ont été placés dans l'armoire Voyantic, un par un, sous forme isolée, et la portée de lecture a été mesurée en tant que sortie directe du logiciel Tagformance. Une comparaison entre les résultats mesurés et les portées de lecture simulées a montré que les performances des étiquettes artisanales correspondaient étroitement aux données simulées. En revanche, les étiquettes ALN-9662 présentaient des écarts, potentiellement attribuables à des variations d'impédance non cohérentes dans les puces Higgs-3 des différents échantillons.

Après avoir compris le modèle physique d'une seule étiquette, nous sommes passés à un scénario plus complexe impliquant plusieurs étiquettes, où nous avons introduit les effets du couplage entre elles. À ce stade, l'évaluation des scénarios impliquant plusieurs étiquettes et communiquant avec le lecteur devient complexe et la quantification des effets de couplage représente un défi important. Il était donc plus pratique d'adopter un modèle simplifié. Dans cette approche, nous avons remplacé le lecteur par une onde plane et l'ensemble des étiquettes ALN-9662 par des dipôles d'adaptation en T et des dipôles demi-onde. Les effets de couplage dans un scénario à étiquettes multiples ont été évalués numériquement à l'aide de NEC et HFSS. Des similitudes de comportement entre les étiquettes commerciales, les dipôles à adaptation en T et les dipôles demi-onde ont été notées pour deux aspects essentiels. Premièrement, en ce qui concerne le diagramme de rayonnement, qui englobe le gain de puissance et le diagramme SER, les dipôles en T et les dipôles demi-onde présentent des distributions angulaires comparables à celles des étiquettes commerciales. Deuxièmement, en termes d'impédance d'entrée, les dipôles demi-onde ne présentent pas un comportement similaire. Toutefois, une analyse plus approfondie des paramètres au niveau du circuit est nécessaire pour comprendre pleinement cette divergence.

Dans le chapitre 3, un modèle de réseau RFID conventionnel comprenant la distribution aléatoire de dipôles avec et sans correspondance en T, et les véritables étiquettes commerciales RFID a été présenté. L'impact du couplage sur la position et l'orientation des antennes en fonction de la densité des antennes et de la polarisation de l'onde incidente a été étudié tout d'abord en termes d'analyse du bilan de puissance. Un ensemble d'antennes chargées réparties de manière aléatoire a été éclairé par l'onde plane polarisée linéairement/circulairement et quatre niveaux de puissance ont été estimés pour une étiquette à la fois en présence d'autres étiquettes chargées et actives à l'aide du circuit équivalent de Thevenin de l'étiquette en question. Les quatre niveaux

Résumé

de puissance de l'étiquette en question sont : la puissance absorbée par la charge (P_L), la puissance reçue par l'antenne (P_{in}), la puissance induite par l'onde plane (P_{Voc}) et la puissance induite par le couplage introduit par d'autres étiquettes actives ($P_{Voc_{in}}$). Selon le principe de la consommation d'énergie, la somme des deux puissances aux deux sources de tension doit être égale à la somme des deux puissances disponibles au niveau de la charge et de l'antenne, c'est-à-dire $P_{Voc} + P_{Voc_{in}} = P_L + P_{in}$. NEC est utilisé pour estimer le bilan de puissance des quatre dipôles d'adaptation en T et des dipôles demi-onde, tandis que HFSS est utilisé pour les étiquettes commerciales. Parmi quelques cas déterministes, un ensemble de dix dipôles distribués de manière aléatoire sur une surface de 1λ fois 1λ dans le plan yoz est pris en considération comme indiqué dans le tableau suivant Figure 3.6. Chaque dipôle a des coordonnées centrales et une orientation aléatoires, à condition qu'ils ne se chevauchent pas. à condition qu'ils ne se chevauchent pas. L'ensemble des dipôles est éclairé par une onde plane polarisée linéairement et circulairement en incidence normale et le résultat du bilan de puissance est illustré à la figure I.

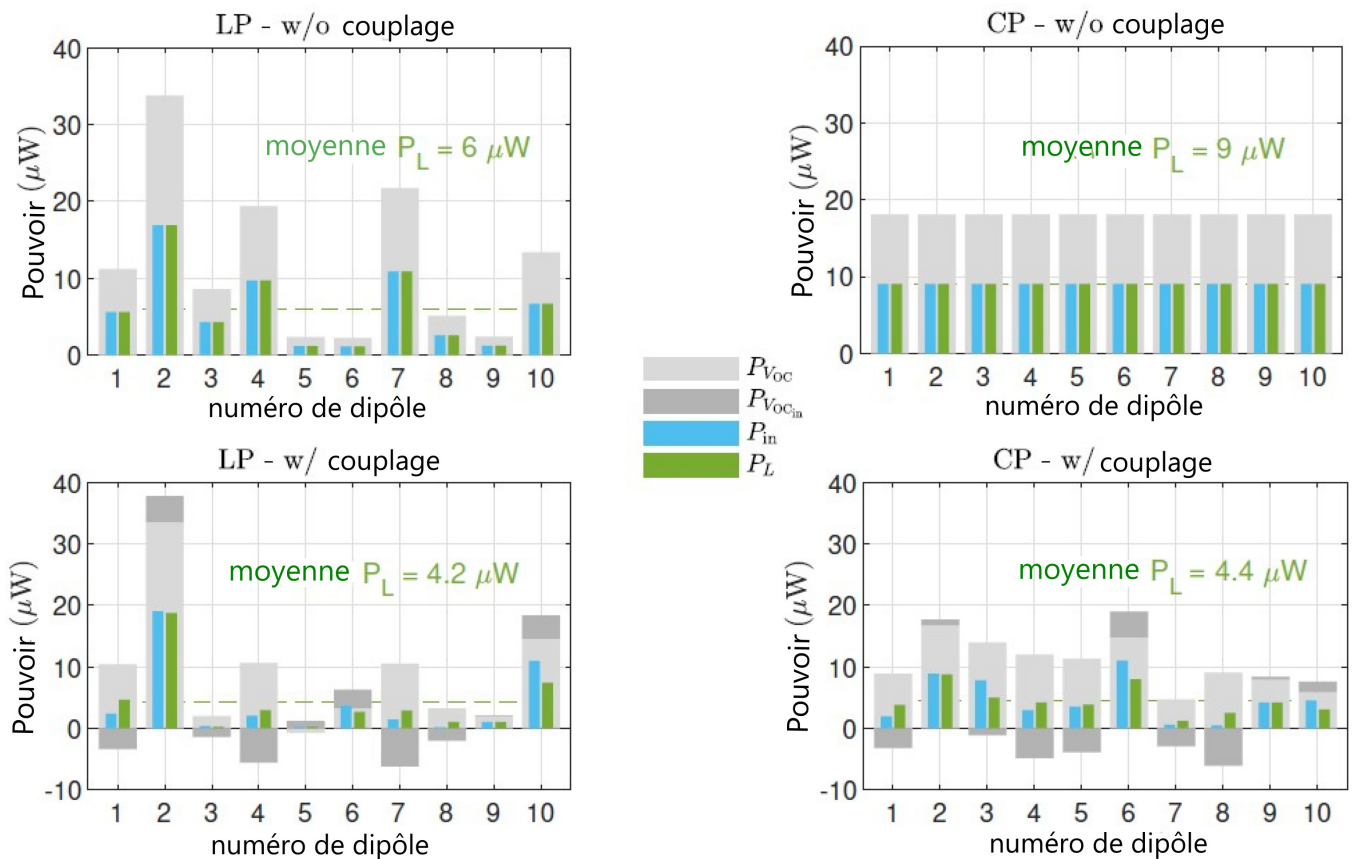


Figure I: Bilan de puissance de dix dipôles demi-onde chargés répartis aléatoirement sur une surface de dimensions $1\lambda \times 1\lambda$.

L'analyse du bilan de puissance en μW pour chaque dipôle, de 1 à 10 pour les ondes planes polarisées linéairement et circulairement. Dans un premier temps, nous avons considéré chaque doublet dans sa position et son orientation d'origine, sans tenir compte du couplage mutuel, c'est-à-dire que seule l'orientation des doublets a été prise en compte. Pour ce faire, nous avons supprimé le couplage mutuel et nous nous sommes concentrés uniquement sur le comportement de chaque dipôle. Le bilan de puissance d'un tel cas est présenté dans la première ligne de la figure I. Sans couplage mutuel et dans le cas d'une polarisation linéaire, nous observons que la puissance à la source, désignée par $P_{V_{nOC}}$, diffère pour chaque doublet en fonction de son orientation. Considérons le dipôle n°2, qui est positionné plus parallèlement à l'onde plane polarisée linéairement, ce qui se traduit par une réception de puissance plus élevée. Inversement, le dipôle no. 5 en polarisation linéaire (LP) subit une désadaptation de polarisation, ce qui entraîne une réception réduite de la puissance. Cependant, pour la polarisation circulaire (CP), cette puissance est égale quelle que soit l'orientation. Cette égalité est due au fait que la polarisation circulaire ne tient pas compte de l'effet de l'orientation. En l'absence de couplage entre les dipôles, la puissance induite par les autres dipôles, notée $P_{V_{inOC}}$, est naturellement nulle pour les deux polarisations. De plus, la puissance absorbée (P_L) et la puissance réémise (P_{in}) pour chaque doublet sont donc identiques ($P_L = P_{in}$) pour les deux polarisations. Cependant, lorsque les dix dipôles sont considérés ensemble, le bilan de puissance change. La deuxième ligne de la figure I illustre ce scénario. En raison des positions et orientations aléatoires des dipôles, ainsi que du couplage entre eux, des valeurs de puissance différentes sont observées aux deux sources de tension, pour les deux polarisations. Tous les dipôles étant de forme identique mais orientés différemment et connectés à leurs charges isolées adaptées, la puissance est répartie de manière inégale entre eux en raison du décalage causé par les effets de couplage mutuel. Par conséquent, la puissance absorbée (P_L) et la puissance réémise ($P_{mathrmin}$) à travers chaque doublet ne sont pas égales dans ce cas. En moyenne, la puissance absorbée par les doublets diminue en raison des effets de couplage. Cependant, l'effet du couplage sur chaque dipôle est un phénomène aléatoire. Par exemple, si l'on prend l'exemple du dipôle no. 10, outre la discordance de polarisation en LP, il y aurait également des effets de couplage, mais la distribution des niveaux de puissance n'a pas beaucoup changé par rapport à la PC pour ce dipôle. Les résultats ci-dessus permettent de conclure que la dégradation des performances de l'antenne est plus importante dans le cas de la polarisation basse que dans celui de la polarisation haute. Cela s'explique par le fait que la méthode LP tient compte à la fois des effets aléatoires et des effets de couplage, alors que la méthode CP ne tient compte que de l'effet de couplage. La puissance d'intérêt spécifique dans la liaison RFID était P_L et donc, en moyenne, il n'y a pas de couplage significatif observé sur P_L dans les deux polarisations.

Résumé

Pour se concentrer explicitement sur un aspect critique de la liaison RFID vers l'avant, nous évaluons la puissance absorbée par la charge pour quelques cas déterministes. Les similitudes observées entre les étiquettes, les dipôles en T et les dipôles demi-onde ont fait l'objet d'une étude plus approfondie en termes de puissance absorbée normalisée associée à la liaison directe. En plus de l'analyse de la liaison directe, nous avons intégré la perspective de la liaison inverse en présentant la section transversale radar (SER) des diffuseurs chargés avec des charges en court-circuit et appariées. Nous avons également vérifié la SCR différentielle de quelques cas déterministes pour expliquer le phénomène de rétrodiffusion. La prévision de la dégradation des performances résultant de la position et de l'orientation des antennes est difficile à réaliser avec une approche déterministe, en particulier dans un contexte de forte densité. C'est pourquoi une étude statistique a été présentée au chapitre 4, où nous avons présenté une évaluation statistique des effets de couplage entre les étiquettes dans les liaisons RFID UHF avant et arrière.

La liaison aller RFID a été étudiée statistiquement pour quatre densités différentes de dipôles (avec et sans T-match) terminés sur leurs charges appariées employant des polarisations linéaires et circulaires, et une densité dans le cas d'étiquettes commerciales employant une polarisation linéaire. Les résultats statistiques montrent une influence non négligeable du couplage sur la puissance reçue au niveau de la puce. Cette technique permet de quantifier le pourcentage d'étiquettes qui ne sont pas alimentées dans un scénario donné. L'impact du couplage est perceptible dans une certaine mesure, et il diminue à mesure que la densité d'étiquettes diminue. Combinée au lien inverse, l'analyse statistique de ΔSER a été présentée pour deux densités de dipôles et de dipôles appariés en T utilisant la polarisation linéaire d'une onde plane. La similarité statistique entre les dipôles avec et sans réseau d'appariement en T pour ΔSER dans la liaison inverse a été vérifiée. En effet, lorsque la proximité des étiquettes dans un contexte de haute densité crée un fort couplage électromagnétique, la probabilité que l'étiquette ne soit pas lue augmente. Cette conclusion a permis de quantifier la réalité physique du couplage électromagnétique en termes de puissance absorbée dans la liaison aller et de ΔSER dans la liaison retour d'un système RFID. Il est intéressant de combiner les résultats obtenus pour la liaison inverse avec ceux de la liaison directe afin d'avoir un meilleur aperçu de l'ensemble de la liaison de communication RFID. Comme nous n'avons pas pu simuler de véritables étiquettes dans la liaison inverse, nous utiliserons des dipôles et des dipôles appariés en T pour comprendre cette relation. Par exemple, parmi les dipôles ou les dipôles appariés en T, les dipôles activés pendant la liaison aller à $P_{Lnorm} \geq 0$ dB, satisfont également aux contraintes de la liaison retour ayant $\Delta SER \geq -23$ dBm². Après avoir été activée par une onde plane à polarisation linéaire dans la liaison aller, la Figure II Nous avons représenté les ΔSER

de ces dipôles activés avec et sans correspondance T sous la forme d'une fonction de distribution cumulative (CDF) afin de déterminer le pourcentage de dipôles satisfaisant à la norme.

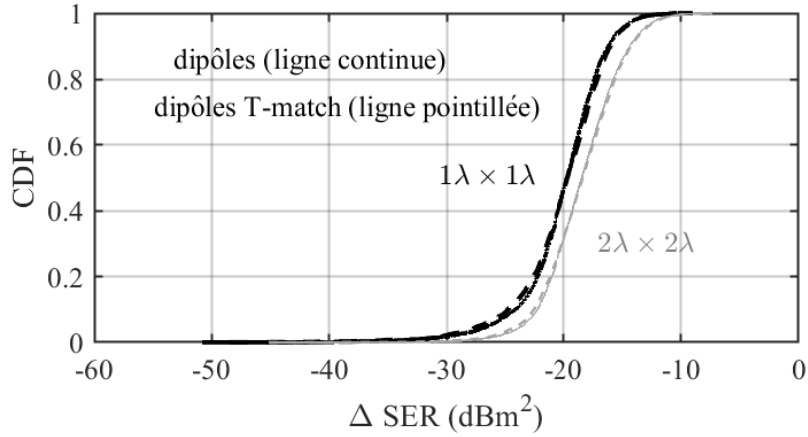


Figure II: Graphique CDF pour le ΔSER en dBm^2 d'échantillons (dipôles et dipôles adaptés en T) éclairés par une onde polarisée linéairement et ayant une puissance absorbée normalisée supérieure à 0 dB sur une distribution de $1\lambda \times 1\lambda$ et $2\lambda \times 1\lambda$.

Table I: Pourcentage de dipôles et dipôles T-match ayant $P_{L_{\text{norm}}} \geq 0$ dB dans la liaison aller, avec un SER différentiel supérieur à la valeur standard dans la liaison retour, c'est-à-dire $\Delta SER \geq -23\text{dBm}^2$.

Dipôle	$1\lambda \times 1\lambda$	$2\lambda \times 2\lambda$
	85%	93%
Dipôles T-match	$1\lambda \times 1\lambda$	$2\lambda \times 2\lambda$
	83%	92%

Le tableau I montre que parmi le nombre de dipôles activés dans la liaison avant, un grand nombre de dipôles satisferaient à la norme dans la liaison arrière. En raison des effets de couplage, les échantillons restants présentent un ΔSER inférieur à la valeur standard, même après avoir été activés dans la liaison avant. La même tendance est valable pour les dipôles appariés en T. Ces informations combinées relatives à la puissance absorbée normalisée et à la SER différentielle aideraient le concepteur RFID à évaluer les performances de la liaison RFID dans son ensemble. Cependant, malgré l'extension de l'étude statistique aux étiquettes RFID UHF dans la liaison aller, il n'est pas encore possible de tirer des conclusions définitives car une comparaison complète des comportements statistiques entre les dipôles, les dipôles appariés en T et les étiquettes RFID en termes de ΔSER reste à faire en raison de ressources informatiques limitées. Des recherches supplémentaires sont nécessaires pour répondre aux hypothèses non résolues.